이학박사학위논문

# Chemical aging of organic aerosol and its climatic implications

## 유기 에어로졸의 대기 중 화학적 노화 과정과 기후에 미치는 영향 연구

2017년 8월

서울대학교 대학원
지구환경과학부
조 두 성

# 유기 에어로졸의 대기 중 화학적 노화 과정과 기후에 미치는 영향 연구

# Chemical aging of organic aerosol and its climatic implications

지도 교수 박 록 진

이 논문을 이학박사 학위논문으로 제출함

2017년 4월

서울대학교 대학원

지구환경과학부

조 두 성

조두성의 이학박사 학위논문을 인준함

2017년 6월

위 원 장 _____ (인)

부위원장 _____ (인)

위 원 _____ (인)

위 원 _____ (인)

위 원 _____ (인)

# Abstract

Aerosols can offset the positive radiative effect by various greenhouse gases, but there is a large uncertainty in the estimate of aerosol's radiative effect. This large uncertainty is mainly due to the limitation of models reproducing various characteristics of aerosols in the real atmosphere. This dissertation is to reduce the gap between observations and models focusing on three issues of aerosol modeling: (1) mass concentration, (2) speciation, and (3) physical/optical property. I investigate these subjects using a global 3-D chemical transport model (GEOS-Chem) and update the model with the new findings. And finally, I apply the developed model to recent aircraft campaign over South Korea (KORUS-AQ) as a case study in a heavily polluted condition. The first issue is that organic aerosol (OA) constitutes significant mass fractions (20%-90%) of total dry fine aerosols in the atmosphere, but global models of OA have shown large discrepancies when compared to the observed values. I update the GEOS-Chem in order to improve the model simulation capability of OA by implementing the volatility basis set (VBS) approach. The VBS method can efficiently simulate chemical aging of SOA in the atmosphere, which can lead to decreases in organic volatility, resulting in an increase of SOA mass yields. I find that the model results with the chemical aging are in better agreement with observations relative to those without chemical aging, especially for rural regions. Second, most models consider OA as a light-scattering aerosol,

but the observations showed that a certain fraction of OA (called as brown carbon; BrC) could be a light-absorbing aerosol. I develop the model to explicitly simulate BrC, which has not been considered in most of the current chemical transport models. I develop a new method for the estimation of BrC emission from biomass burning and biofuel use based on the relationship between modified combustion efficiency and absorption Ångstrom exponent. I calculate that BrC accounts for 21% of the global mean OA concentration, which is typically assumed to be scattering. The inclusion of BrC absorption in the model decreases the direct radiative cooling effect of OA by 16%. In addition, the BrC absorption leads to a general reduction of $NO_2$ photolysis rates and ozone concentration (by up to -13% in spring time in Asia). Third, some previous global modeling studies showed positive single scattering albedo (SSA) bias, which can lead to a significant change in aerosol radiative forcing. However, it is difficult to find the cause of the SSA bias because of diverse physical/optical characteristics of aerosols are combined in the model. Therefore, I carry out multiple sensitivity simulations to examine the effects of individual factors on calculated SSA. I find that large variation of calculated black carbon absorption may result from slight changes of its geometric mean radius, geometric standard deviation, real and imaginary refractive indices, and density. The inclusion of BrC and observationally-constrained dust size distribution also significantly affects SSA, and results in a remarkable improvement for simulated SSA at 440 nm compared with the AERONET

observations. Finally, I examine the observed OA characteristics during the KORUS-AQ campaign with the updated model above. The model simulates similar mean OA concentrations against the observed OA (5% bias). The model also successfully reproduces mean vertical profile of OA during KORUS-AQ. However, I find that the model performance is significantly changed if the evaluation is focused on the specific research flight. The model underestimates the observed OA by more than a factor of two when the observation is heavily influenced by biomass burning. Fine-scale biomass burning emissions (< 0.01 $km^2$) are missed in the current emission inventory due to the coarse spatial resolution of satellite, but they contribute about 90% of biomass burning in South Korea. On the other hand, the model overestimates observed OA concentrations from some research flights. I find that photolytic loss, which is revealed in the observation but not considered in the model, could reduce the overestimation and should be considered in future modeling studies.

Keyword : Organic aerosol, Chemical aging, Brown carbon, Direct radiative effect, Single scattering albedo

Student Number : 2010-20353

# Table of Contents

# List of Tables

# List of Figures

# Abbreviation index

| | |
|---|---|
| AAE | absorption Ångström exponent |
| ACCMIP | atmospheric chemistry and climate model intercomparison project |
| AEIC | aviation emissions inventory code |
| AERONET | aerosol robotic network |
| AMS | aerosol mass spectrometer |
| AOD | aerosol optical depth |
| BC | black carbon |
| BrC | brown carbon |
| CA | carbonaceous aerosol |
| DEAD | dust entrainment and deposition |
| DRE | direct radiative effect |
| DRF | direct radiative forcing |
| EMEP | european monitoring and evaluation programme |
| FINN | fire inventory from ncar |
| GCM | global climate model |
| GEOS | goddard earth observing system |
| GFED | global fire emission database |
| GMAO | global modeling and assimilation office |
| HOA | hydrocarbon-like organic aerosol |
| HTAP | hemispheric transport of air pollution |
| HULIS | humic-like substances |
| IMPROVE | interagency monitoring of protected visual environments |

| | |
|---|---|
| IVOC | Intermediate-volatility organic compound |
| MACCity | monitoring atmospheric composition & climate/city zen |
| MAE | mass absorption efficiency |
| MEGAN | model of emissions of gases and aerosols from nature |
| MERRA | modern era retrospective-analysis for research and applications |
| NMB | normalized mean bias |
| NME | normalized mean error |
| OA | organic aerosol |
| OC | organic carbon |
| OM | organic matter |
| OOA | oxygenated organic aerosol |
| PBL | planetary boundary layer |
| POA | primary organic aerosol |
| POC | primary organic carbon |
| R | correlation coefficient |
| RETRO | reanalysis of the tropospheric chemical composition |
| RMA | reduced major axis |
| RMSE | root mean square error |
| SOA | secondary organic aerosol |
| SOC | secondary organic carbon |
| SOG | secondary organic aerosol in a gas phase |
| SPARTAN | Surface particulate matter network |
| SSA | single scattering albedo |
| SVOC | semi-volatile organic compound |
| TOR | thermal optical reflectance |
| TOT | thermal optical transmittance |
| VBS | volatility basis set |
| VOC | volatile organic compound |
| WSOC | water-soluble organic carbon |

# Chapter 1. Introduction

Organic aerosol (OA) constitutes significant mass fractions (20% to 90%) of total dry fine aerosols in the atmosphere (Zhang et al., 2007) and has adverse effects on human health (Folinsbee, 1993; Pavia et al., 1977) and atmospheric visibility (Eidels-Dubovoi, 2002). OA has also received increasing attention in climate studies because of its negative radiative forcing, which may offset a significant fraction of global warming by greenhouse gases (Ming et al., 2005; Myhre et al., 2009). However, the effect of OA on climate is still unclear because of an incomplete understanding of its sources, chemical formation, and physical and chemical characteristics (Hallquist et al., 2009; Kanakidou et al., 2005). In particular, secondary organic aerosols (SOAs), which are produced in the atmosphere from gas-phase precursors, are poorly understood relative to primary organic aerosols (POAs), which are directly emitted from sources.

Optical properties of OA are also poorly understood. Traditionally, OA is considered as a light-scattering aerosol, and black carbon (BC) is considered as a light absorbing aerosol. These two aerosol types are classified as carbonaceous aerosols (CAs) and emitted together mainly by combustion processes (except for SOA). Therefore, the climatic effect of CAs depends on the relative contributions of BC to CAs. For example, the net climatic effect of biomass burning is estimated to be negligible, whereas diesel use causes climate warming although the first source is larger than the

latter for CAs (Forster et al., 2007).

However, many field observations and chamber studies recently showed that a certain fraction of OA could absorb solar radiation, especially for shortwave wavelengths (< 400 nm) (Alexander et al., 2008; Hecobian et al., 2010; Kirchstetter and Thatcher, 2012; Kirchstetter et al., 2004; Yang et al., 2009). This light-absorbing OA fraction is referred to as brown carbon (BrC) aerosol (Andreae and Gelencser, 2006; Laskin et al., 2015). If BrC is prevalent, and its climate effect is significant, then previous estimates of the climate effect of CAs need to be revised.

On the other hand, recent IPCC report (AR5) showed that aerosols dominate the uncertainty associated with the total anthropogenic driving of climate change (Myhre et al., 2013). One of the largest contributors to this uncertainty is single scattering albedo (SSA). Previous studies suggested that a small change in SSA can lead to a significant change in aerosol radiative forcing based on the analysis of in-situ observations, chemical transport and radiative transfer model results, and satellite data (Loeb and Su, 2010; McComiskey et al., 2008; Srivastava et al., 2011). For example, a decrease in SSA from 0.9 to 0.8 (11% decrease) can often change the sign of direct radiative forcing (DRF) from negative (cooling) to positive (warming) values (Jethva et al., 2014).

## 1.1. Uncertainty of SOA simulation

Global models of OA have shown large discrepancies when compared to the observed values because of the limited capability to simulate SOA. Such simulations poorly represent complex SOA formation in the atmosphere (Heald et al., 2005; Volkamer et al., 2006) and have been primarily based on the gas-particle partitioning of semi-volatile organics (Pankow, 1994a; Pankow, 1994b), which is typically parameterized in models using two oxidation products (called the two-product approach) developed by Odum et al. (1996). The two-product approach has been found to be sufficient for representing experimentally observed SOA yields in chambers (Chung and Seinfeld, 2002; Griffin et al., 1999).

However, many studies have recently shown that chemical aging reactions in the atmosphere are important (Donahue et al., 2006; Jimenez et al., 2009; Kroll and Seinfeld, 2008) because they can lead to decreases in organic volatility, resulting in increases of SOA mass yields. This photochemical aging, which cannot be properly measured in chemical chambers, may contribute to the very low bias in models that do not simulate chemical aging processes in the atmosphere, especially photochemical aging progresses (Volkamer et al., 2006).

To efficiently simulate chemical aging in the atmosphere, Donahue et al. (2006) proposed the volatility basis set (VBS) approach, which has been extensively used in regional modeling studies (Lane et al., 2008; Murphy

and Pandis, 2009; Robinson et al., 2007; Shrivastava et al., 2008; Tsimpidi et al., 2010). Using the VBS approach, SOA-forming reactions from different parent hydrocarbons can be mapped onto the same set of bins encompassing the range of typical ambient organic aerosol mass concentrations (~0.1-100 μg $m^{-3}$). Then, aging reactions can easily be simulated by altering the SOA volatility. The VBS approach has recently been implemented in global models. Farina et al. (2010) first used the Goddard Institute for Space Studies General Circulation Model II (GISS GCM II), a "unified" climate model (4° longitude by 5° latitude with 9 vertical layers), to investigate SOA aging. They found that the OA simulation was in better agreement with the Interagency Monitoring of Protected Visual Environments (IMPROVE) data from the United States. Yu (2011) extended the two-product approach by adding an additional low-volatility tracer with a simple aging step and demonstrated improved SOA simulations, especially in rural areas.

For the simulation of SOA aging processes using the VBS approach, models generally assume that gas-phase semi-volatiles react with OH; the saturation vapor pressures of these semi-volatiles is reduced by one order of magnitude. In this process, an aging constant plays an important role because a high value leads to high mass concentrations of SOA, and vice versa. The aging constant of SOA differs greatly in the literature, ranging from $2.5 \times 10^{-12}$ $cm^3$ $molecule^{-1}$ $s^{-1}$ to $4 \times 10^{-11}$ $cm^3$ $molecule^{-1}$ $s^{-1}$ (Farina et al., 2010; Jathar et al., 2011; Lane et al., 2008; Murphy and Pandis, 2009;

Murphy and Pandis, 2010; Shrivastava et al., 2008). Therefore, its use in models results in large uncertainty.

In contrast, POA is traditionally regarded as nonvolatile. However, based on laboratory experiments, Robinson et al. (2007) proposed that POA emissions are semi-volatile. A number of modeling studies have employed semi-volatile POA (Jathar et al., 2011; Murphy and Pandis, 2009; Pye and Seinfeld, 2010; Shrivastava et al., 2008), which resulted in decreased OA mass concentrations over the source regions but increased OA concentrations away from the source regions as a result of enhanced SOA formation from semi-volatile POA transport.

Jathar et al. (2011) added semi-volatile POA emissions and SOA aging to the GISS GCM II and found that this addition did not enhance the model performance compared with the observed OA concentrations. However, the simulated SOA-to-OA ratio was greatly increased, resulting in better agreement with the observed ratio. Pye and Seinfeld (2010) simulated semi-volatile POA using GEOS-Chem and obtained results that were consistent with those of Jathar et al. (2011).

## 1.2. Light absorption of OA

Recent studies showed that the solar absorption of BrC is not negligible, and is even comparable to that of BC (Alexander et al., 2008; Chung et al., 2012; Kirchstetter and Thatcher, 2012). Using residential wood smoke samples, Kirchstetter and Thatcher (2012) calculated that BrC absorption accounts for 14% of total solar absorption by CA, and even contributes 49% of solar absorption of CA at wavelengths below 400 nm. Chung et al. (2012) found that OC contributes about 45% of CA absorption at 520 nm by analyzing observations at the Gosan site in South Korea. Using aerosol optical property observations at Aerosol Robotic Network (AERONET) sites, Bahadur et al. (2012) estimated that BrC absorption at 440 nm is about 40% of BC absorption at the same wavelength, whereas at 675 nm it is less than 10% of BC absorption.

Several efforts have also been made to examine the chemical and physical properties of BrC. Some studies showed that humic-like substances (HULIS) were related to BrC (Hoffer et al., 2006; Kim and Paulson, 2013; Lukács et al., 2007) based on the high absorption Ångström exponent (AAE) of HULIS in the range of 6–7, indicating that the specific absorption increases substantially towards the shorter wavelengths (Hoffer et al., 2006), although the sources and the dominating chromophores of HULIS have not clearly been revealed yet (Moise et al., 2015; Graber and Rudich, 2006). Alexander et al. (2008) observed individual BrC spheres in East Asian

outflows, and showed that the characteristics of BrC spheres (AAE of 1.5) were different from those of HULIS and also strongly absorbing. On the other hand, several classes of compounds have been identified as potential contributions to BrC - nitroaromatic compounds, such as nitrophenols, imidazole-based and other N-heterocyclic compounds, and quinones (Laskin et al., 2015). Furthermore, secondary organic carbon (SOC) produced from aromatic species has been found to absorb solar radiation, especially in high NOx conditions (Jaoui et al., 2008; Laskin et al., 2015; Lin et al., 2015; Liu et al., 2012; Nakayama et al., 2010; Nakayama et al., 2013; Yu et al., 2014; Zhong and Jang, 2011).

Even though the chemical composition of BrC is not clearly understood yet, observations strongly indicate possible important sources of BrC (Laskin et al., 2015). Using the positive matrix factorization analysis of absorption at 365 nm over the southeastern United States in 2007, Hecobian et al. (2010) showed that biomass burning was the most dominant source of BrC (55%), followed by SOC (26-34%). Many other studies have also suggested biomass burning as the most important BrC source (Chakrabarty et al., 2010; Clarke et al., 2007; Favez et al., 2009; Hoffer et al., 2006; Kirchstetter and Thatcher, 2012; Kirchstetter et al., 2004; McMeeking, 2008; Saleh et al., 2014). Several studies recently proposed SOC as an additional BrC source, especially when it is aged in the atmosphere (Bones et al., 2010; Flores et al., 2014; Hawkins et al., 2014; Jaoui et al., 2008; Laskin et al., 2014; Laskin et al., 2010; Liu et al., 2014; Nakayama et al., 2010;

Nakayama et al., 2013; Nguyen et al., 2012; Updyke et al., 2012; Zhang et al., 2011; Zhong and Jang, 2011).

Despite the ample observational studies, very few modeling studies have been conducted to simulate global and regional distributions of BrC and to further quantify its radiative effect (Feng et al., 2013; Jacobson, 2001; Lin et al., 2014; Park et al., 2010; Wang et al., 2014). Jacobson (2001) first assumed 10% of OC as a solar-absorbing aerosol in a model, and this assumption resulted in an increase of the global DRF by 0.03–0.05 W $m^{-2}$. Park et al. (2010) estimated BrC concentrations in East Asia using the mass ratio of BrC to BC, and the resulting annual clear-sky DRF of BrC over East Asia was 0.05 W $m^{-2}$. Feng et al. (2013) simulated global BrC concentrations by considering 92% of OC from biomass burning and biofuel use as BrC, and estimated 0.09 W $m^{-2}$ for the global clear-sky DRF of BrC. Lin et al. (2014) calculated the DRF of OC by assuming that all of the biomass burning and the biofuel OC is BrC, and all of the SOC (as a high-absorbing case) as BrC. They estimated the global clear-sky DRF of OC as -0.20 W $m^{-2}$.

## 1.3. SSA calculation in previous studies

Aerosol optical depth (AOD), single scattering albedo (SSA), and asymmetry parameter are important input for calculating direct radiative forcing (DRF) of aerosols (Iacono et al., 2008). Among these aerosol optical properties, SSA is the most uncertain factor contributing to the uncertainty of aerosols DRF. Generally, aerosol SSA is calculated using the Mie theory by assuming spherical particles. This spherical assumption may not be applicable to aerosols with diverse geometrical shapes including black carbon (BC) and soil dust (Mishchenko, 2009). For this reason, previous studies have suggested alternative methods such as the Rayleigh-Debye-Gans theory for aggregates (Farias et al., 1996) and the T-matrix method for non-spherical particles (Mishchenko, 2009). However, the Mie theory is still a powerful tool for global model calculations by virtue of its brevity, computational efficiency, and applicability to radiative transfer models. As a result, the Mie theory was used in all models that participated in a recent AeroCom study (Myhre et al., 2013b), which is the basis of IPCC fifth assessment report (Myhre et al., 2013a).

An application of the Mie theory for aerosol SSA calculations requires precise information on the size distribution, refractive index, particle density, and hygroscopic growth factors of aerosols. However, it is

difficult to determine these parameters from measurements because the characteristics of aerosols vary widely depending on regions, sources, aging and mixing state, and measurement techniques of aerosols. As a result, input parameters used for aerosol SSA calculations were diverse according to corresponding measurements, which can cause a wide diversity of calculated aerosol SSAs. For example, some previous global modeling studies found no significant bias in calculated SSAs against AERONET observations (Chin et al., 2009; Dai et al., 2015), while other studies showed positive bias in their estimates (Feng et al., 2013; Jo et al., 2016; Lin et al., 2014; Myhre et al., 2009). I surmise that the SSA bias could be reduced when models used relatively high BC emissions and a low BC density. For example, Chin et al. (2009) used the BC emission of 10.2 TgC $yr^{-1}$ (which is 50% higher than 6.8 TgC $yr^{-1}$ used in Jo et al. (2016)) and the BC density of 1.0 g $cm^{-3}$ (which is the lowest value used in the literature (Koch et al., 2009)). Because limited information on the emission and physical parameters of BC used in previous studies are available, I cannot reach any conclusion to explain the diversity of previous modeling studies for estimating global SSA values. Instead, I mainly focus on physical parameters affecting SSA calculation, which are discussed below.

Choosing the appropriate input parameters for the Mie calculations is a greater challenge for BC than for other aerosols, because BC particles usually exist as agglomerates of primary spherules rather than individual spherical particles (Alexander et al., 2008). As a result, physical parameters

of BC used in AeroCom models are diverse – mass median diameter (0.020 – 0.852 μm), density (1.0 – 2.0 g $cm^{-3}$), and refractive index (1.75-0.44i – 2.0-1.0i) (Koch et al., 2009). Furthermore, SSA may significantly vary depending on their mixing states. Both theoretical and observational studies showed that a SSA value of an internally mixed BC aerosol is lower than that of an externally mixed BC (Bond et al., 2006; Drury et al., 2010; Shiraiwa et al., 2008).

Although BC is a major species contributing to aerosol absorption, soil dust is also an important contributor (Yang et al., 2009). A global mass concentration of soil dust is the largest among other aerosols. Thus, it could have a significant impact on global SSA. Especially the size distribution of dust is poorly evaluated in global models (Kok, 2011; Kok et al., 2017). Previous studies showed a significant change of observed SSA (Khatri et al., 2014) and simulated aerosol DRF (Mahowald et al., 2014) as a function of coarse/fine fractions of soil dust.

Finally, few models consider an absorbing fraction of OA, which is typically assumed scattering although recent studies confirmed its presence (Alexander et al., 2008; Kirchstetter and Thatcher, 2012; Laskin et al., 2015). The inclusion of this absorbing OA (known as brown carbon, BrC) may have a significant effect on SSA calculation (Feng et al., 2013; Jo et al., 2016; Lin et al., 2014).

## 1.4. Objectives of this study

As discussed in Chapters 1.1-1.3, there are many issues in aerosol modeling for the estimation of its climate effects. IPCC AR5 showed large uncertainties of aerosol forcing for not only indirect effect (-1.2 to 0.0 W $m^{-2}$) but also direct effect (-0.95 to +0.05 W $m^{-2}$) (Myhre et al., 2013). Using a 3-D global chemical transport model (GEOS-Chem) driven by assimilated meteorological fields, I investigate three modeling issues of aerosols: SOA simulation, light absorbing OA, and SSA calculation. I update the model with the new findings and evaluate it against global observation networks.

For the implication of the updated model on regional-scale simulation, I examine the model performance using aircraft observations of KORUS-AQ campaign. This campaign provided sizable measurements of aerosols and gases and captured high concentrations of them from various sources over South Korea.

The objectives of this dissertation are as follows:

1. to improve the simulation capability of OA mass concentration by considering the chemical aging process of SOA (Chapter 3).
2. to develop the method to explicitly simulate BrC in the model (Chapter 4).
3. to examine key factors of SSA calculation (Chapter 5).

4. to investigate the updated model performance in a heavily polluted urban atmosphere as a case study (Chapter 6)

# Chapter 2. Model description

## 2.1. GEOS-Chem model

I use the GEOS-Chem global 3-D chemical transport model (Bey et al., 2001), which is driven by the assimilated meteorological data. I use different model versions for this study – version 9.1.2 for Chapter 3 and 4, and version 10.1 for Chapter 5 and 6. For meteorological data, Goddard Earth Observing System version 5 (GEOS-5) (Chapter 3), Modern Era Retrospective-analysis for Research and Applications (MERRA) (Chapter 4 and 5), and GEOS-FP (Chapter 6) are used. Meteorological data including temperature, winds, humidity, planetary boundary layer height, and other meteorological variables.

The simulation of POA in GEOS-Chem was described in detail by Park et al. (2003). The model includes two POA tracers: hydrophobic and hydrophilic POAs. Combustion sources emit hydrophobic POA, which then becomes hydrophilic with an e-folding time of 1.15 day (Cooke et al., 1999; Park et al., 2003). I assume that 50% of POAs emitted are hydrophobic (Park et al., 2003).

SOA simulation in GEOS-Chem version 9.1.2 is based on the scheme developed by Chung and Seinfeld (2002) who used the two-product approach. This scheme has been used in previous studies (Heald et al., 2005;

Henze and Seinfeld, 2006; Henze et al., 2008; Liao et al., 2007). A detailed description of the two-product approach in GEOS-Chem can be found in Liao et al. (2007). Here, I briefly discuss a few updates. The model considers nine lumped parent hydrocarbons that consist of monoterpenes, sesquiterpenes, isoprene, and aromatic compounds. Oxidation of these parent hydrocarbons by OH, $O_3$, and $NO_3$ yields a total of 56 products. At every model time step, these oxidation products are partitioned into a gas phase (SOG) and a particle phase (SOA), which are determined by equilibrium partitioning coefficients and pre-existing POA concentrations. These products are then lumped into 10 tracers (5 for gases and 5 for aerosols). Depending on the source, 8 tracers are biogenic, and 2 are anthropogenic. This scheme does not account for aging of the oxidation products. In GEOS-Chem version 10.1, SOA simulation is updated following Pye et al. (2010), who considers parent hydrocarbons of monoterpenes, sesquiterpenes, isoprene, and aromatics with NOx dependent yields. I update SOA simulation scheme, which is described in detail in Chapter 3.1.

The simulation of other inorganic salts in GEOS-Chem was described by Park et al. (2004). Nitrate aerosol formation is calculated using ISORROPIA II (Fountoukis and Nenes, 2007; Pye et al., 2009), which computes the $H_2SO_4$-$HNO_3$-$NH_3$–$H_2O$ thermodynamics. Dust aerosols are computed by the Dust Entrainment And Deposition (DEAD) scheme of Zender et al. (2003), along with the source function used in GOCART

(Ginoux et al., 2001), as elucidated in Fairlie et al. (2007). The sea salt emission is estimated as a function of dry particle size, local 10 m wind speed, and sea surface temperature (Alexander et al., 2005; Jaeglé et al., 2011).

Wet deposition is simulated using the scheme described by Liu et al. (2001) and applies only to hydrophilic aerosols. This scheme accounts for scavenging in convective updrafts, rainout from convective anvils, and rainout and washout from large-scale precipitation (Mari et al., 2000). Dry deposition algorithm uses a standard resistance-in-series model dependent on local surface types and meteorological conditions, as described by Wang et al. (1998).

## 2.2. Emissions

Here I use anthropogenic, biogenic, and biomass burning emissions to simulate gasses and aerosols. For biogenic emissions, I use the same emission inventory, but anthropogenic emissions vary by study because of different target years in each Chapter. The details are described below.

Biogenic emissions are obtained from the Model of Emissions of Gases and Aerosols from Nature (MEGAN) v2.1 inventory (Guenther et al., 2012). The MEGAN inventory includes isoprene, methylbutenol, and seven monoterpene compounds (α-pinene, β-pinene, limonene, myrcene, sabinene, 3-carene and ocimene). The emissions of these compounds are calculated on the basis of emission activity factors, canopy environment, leaf age, and soil moisture. The global biogenic emissions of isoprene and the seven monoterpenes are 456 TgC $yr^{-1}$ and 91 TgC $yr^{-1}$, respectively.

In Chapter 3, I use global fossil fuel (3.05 TgC $yr^{-1}$) and biofuel (6.28 TgC $yr^{-1}$) emissions of POA from Bond et al. (2007), who estimated emissions by country, sector, fuel type, and fuel/technology for 2000. This emission inventory has no monthly variations. However, domestic wood burning for heating has strong seasonal dependency. Therefore, in Chapter 4,

I update this emission inventory with the Monitoring Atmospheric Composition & Climate/City Zen (MACCity) emission inventory (Diehl et al., 2012; Granier et al., 2011) to obtain seasonal variations of global biofuel emissions and to scale up for 2007. I divide the whole globe into regions with similar seasonality according to the Atmospheric Chemistry and Climate Model Intercomparison Project (ACCMIP) (Lamarque et al., 2010), which is the basis of the MACCity inventory. I apply the annual trend of each ACCMIP region to the emissions from Bond et al. (2007). In Chapter 5, I use recently published anthropogenic inventory - the Hemispheric Transport of Air Pollution (HTAP) v2 inventory with a horizontal resolution of 0.1° x 0.1° (Janssens-Maenhout et al., 2015). Anthropogenic VOC (aromatics: benzene, toluene, and xylene) emissions are obtained from the Reanalysis of the TROpospheric chemical composition (RETRO) inventory; the total annual anthropogenic VOC emission is 13.57 TgC $yr^{-1}$, and these anthropogenic VOC emissions are used in Chapters 3-5. In Chapter 6, I use the NIER/KU-CREATE (Comprehensive Regional Emissions inventory for Atmospheric Transport Experiment) inventory, which was jointly developed by National Institute of Environmental Research (NIER) and Konkuk University (KU). NIER/KU-CREATE inventory covers Asia region and the base year is 2015.

I use three different biomass burning inventories - the Global Fire Emission Database version 3 (GFEDv3) inventory (van der Werf et al., 2010) for 2009 (Chapter 3), Fire inventory from NCAR (FINN) version 1

(Wiedinmyer et al., 2011) for 2007 (Chapter 4), GFED version 4 (Giglio et al., 2013) inventory for 2008-2010 (Chapter 5), and FINN version 1.5 for 2016 (Chapter 6).

# Chapter 3. Effects of chemical aging on global secondary organic aerosol

In this study, I implement the VBS approach in GEOS-Chem. I extensively evaluate the model by comparing it with observations from a global aerosol mass spectrometer (AMS) dataset compiled by Zhang et al. (2007) with 10 additional observations compiled by Spracklen et al. (2011), the IMPROVE dataset from the United States (Malm et al., 1994), the European Monitoring and Evaluation Programme (EMEP) dataset from Europe (Yttri et al., 2007), and organic carbon (OC) and water-soluble organic carbon (WSOC) concentration data collected over East Asia (Aggarwal and Kawamura, 2009; Batmunkh et al., 2011; Cho and Park, 2013; Choi et al., 2012; Feng et al., 2006; Li et al., 2010; Miyazaki et al., 2007; Pathak et al., 2011; Pavuluri et al., 2013; F. Zhang et al., 2012; Zhao et al., 2013). Then, I examine the effects of semi-volatile POA aging by conducting sensitivity simulations. Based on the simulated results, I analyze the global sources and burdens of SOA. The simulated SOA concentrations are then used to compute the direct radiative effect (DRE) of SOA to reveal the global climatic implications.

## 3.1. Volatility basis set approach

I implement the VBS approach (Donahue et al., 2006) in GEOS-Chem to consider aging reactions. First, I partition all semi-volatile organics by volatility, with 6 bins defined by a set of prescribed vapor pressures as follows: $[C^*_i]$ = [0.01, 0.1, 1, 10, 100, 1000] μg $m^{-3}$ at 300 K. $C^*_i$ is the effective saturation concentration of species i. The temperature dependence of $C^*$ is calculated using the Clausius-Clapeyron equation:

$$C^*_T = C^*_{T_{ref}} \frac{T_{ref}}{T} \exp\left[\frac{\Delta H}{R}\left(\frac{1}{T_{ref}} - \frac{1}{T}\right)\right] \quad (3.1)$$

where ΔH is the enthalpy of vaporization, and R is the universal gas constant. ΔH is one of the most important parameters for SOA formation because it determines the rate that the saturation vapor pressure decreases with decreasing temperature. A high ΔH value leads to a higher SOA mass increase with decreasing temperatures lower than the reference temperature. The ΔH values differ from study to study, ranging from ~10 kJ $mol^{-1}$ to ~180 kJ $mol^{-1}$ (Yu, 2011). In this study, the ΔH values are assumed to be 100 kJ $mol^{-1}$ for $C^*$ = 1 μg $m^{-3}$ and decrease by 6 kJ $mol^{-1}$ for each increase in order of magnitude of $C^*$ (Donahue et al., 2006; Robinson et al., 2007). The GEOS-Chem model previously used 42 kJ $mol^{-1}$ for all SOA tracers (Chung

and Seinfeld, 2002).

In the VBS approach, each VOC reacts with OH, $O_3$, and $NO_3$; the resulting oxidation products (semi-volatile species) are allocated into 4 bins, $[C^*_i] = [1, 10, 100, 1000]$ μg $m^{-3}$, using yield parameters based on chamber studies. I adopt the yield parameters compiled by Farina et al. (2010) (Table 1). Following Henze et al. (2008), I consider one $NO_x$ level (low $NO_x$) for biogenic species and two $NO_x$ levels (high and low $NO_x$) for aromatic species. Compared with previous SOA studies using GEOS-Chem, I considerably update the yield parameters of semi-volatile species, as shown in Table 3.1. For example, the isoprene yield parameter of the VBS is 0.04, based on several chamber studies (Farina et al., 2010; Dommen et al., 2006; Kleindienst et al., 2007; Kroll et al., 2005, 2006). However, the parameter for the two-product approach is 0.26 (Henze and Seinfeld, 2006; Kroll et al., 2006), which is much higher. Yield parameters of other VOCs also differ between the VBS and the two-product schemes. For example, I use 0.52 to 0.79 for aromatic VOCs with the VBS approach, which are higher than the values (0.09-0.47) used by Henze et al. (2008). The effects of the updated yield parameters on the global budget of SOA are discussed in Chapter 3.4.

Table 3.1. Yield parameters used in this study (Farina et al., 2010). High-NOx yields are presented in parentheses. Aromatic yields are scaled with the $RO_2$/VOC ratio because GEOS-Chem applies yield parameters to $RO_2$ (Henze et al., 2008).

| Oxidants | Species[1] | Saturation concentration (μg $m^{-3}$) | | | |
|---|---|---|---|---|---|
| | | 1 | 10 | 100 | 1000 |
| OH and $O_3$ | ALPH | 0.07 | 0.06 | 0.24 | 0.41 |
| | LIMO | 0.32 | 0.31 | 0.3 | 0.6 |
| | TERP | 0.01 | 0 | 0.54 | 0 |
| | ALCO | 0.03 | 0.06 | 0.1 | 0.5 |
| | SESQ | 0 | 0.55 | 0.54 | 0 |
| | ISOP | 0.02 | 0.02 | 0 | 0 |
| | BENZ | 0.0049 (0.0049) | 0.1079 (0.1079) | 0.2600 (0.1521) | 0.3140 (0.2600) |
| | TOLU | 0.0053 (0.0053) | 0.1170 (0.1170) | 0.2818 (0.1649) | 0.3403 (0.2818) |
| | XYLE | 0.0057 (0.0057) | 0.1247 (0.1247) | 0.3004 (0.1757) | 0.3628 (0.3004) |
| $NO_3$ | monoterpenes | 0.07 | 0.06 | 0.24 | 0.41 |
| | sesquiterpenes | 0.07 | 0.06 | 0.24 | 0.41 |

1) **ALPH - pinene, sabinene, carene, and terpenoid ketones; LIMO - limonene; TERP - terpinene and terpinolene; ALCO - myrcene, terpenoid alcohols and ocimene; SESQ - sesquiterpenes; ISOP - isoprene; BENZ - benzene; TOLU - toluene; XYLE - xylene**

The chemical aging of semi-volatile organics is accounted for by decreasing their saturation vapor pressures. In this study, I only apply the aging to aromatic species. Biogenic species are not aged following previous global modeling studies (Farina et al., 2010; Jathar et al., 2011). Lane et al. (2008) and Murphy and Pandis (2009) found that models overestimated the observed OA concentrations when they considered the aging of both biogenic and anthropogenic SOA. Murphy and Pandis (2010) further investigated SOA aging and found that including only anthropogenic SOA aging resulted in the best agreement with observations relative to the other cases, which used only biogenic SOA aging, no aging, and both biogenic and anthropogenic SOA aging.

There may be two reasons related to biogenic SOA aging for the overestimation of OA concentrations in models. First, mass yield parameters of biogenic SOA represent completed reactions; hence, they do not need to be aged (i.e., biogenic SOA aging is already accounted for in the yield parameters) (Farina et al., 2010; Jathar et al., 2011). This can be partially explained from chamber studies – the growth of SOA from VOCs having one double bond stops once all the VOCs are consumed (i.e., no aging process); some biogenic VOCs (e.g., α-pinene, β-pinene, $\Delta^3$-carene) have

one double bond (Ng et al., 2006). These monoterpenes constitute a large portion of biogenic SOA (Hallquist et al., 2009). Second, the chemical aging using the VBS approach only accounts for functionalization. However, in the real atmosphere, there might be an offset between functionalization (decreased volatility) and fragmentation (increased volatility) effects, especially for biogenic SOA (Murphy et al., 2012).

At every time step, I calculate the amount of aged gas-phase aromatic SOAs proportional to the reaction with OH using various rate constants: $1 \times 10^{-10}$, $4 \times 10^{-11}$, $1 \times 10^{-11}$, $4 \times 10^{-12}$, and $1 \times 10^{-12}$ $cm^3$ $molecule^{-1}$ $s^{-1}$. The vapor pressure of these aged SOAs is reduced by one order of magnitude, and they are moved into the next lower bin (Jathar et al., 2011). Additionally, I further conduct a no aging case with the VBS and the two-product schemes as a control run. All SOAs in the model are assumed to be hydrophilic aerosols, which are subject to wet deposition.

## 3.2. Model Evaluation

I focus the model evaluation on surface networks of OA observations. First, I compare the model with the global aerosol mass spectrometer (AMS) dataset, which measures OA into two categories: hydrocarbon-like OA (HOA) and oxygenated OA (OOA). I also use two regional observation network datasets, IMPROVE and EMEP, from the United States and Europe, respectively. These data do not classify OA, as in the AMS dataset, and instead provide total OC concentrations that I used for comparison with the model simulations. Finally, I evaluate the model in East Asia using OC and water-soluble OC (WSOC) data collected over East Asia.

### 3.2.1. Global

I use the AMS dataset compiled by Zhang et al. (2007) along with 10 more observations compiled by Spracklen et al. (2011) to evaluate the global simulations, which are conducted for 2009. The simulated year is different from the observation period of the AMS dataset (2000-2008). However, this difference is not significant in terms of monthly variations (on which the model evaluation is primarily focused), as shown in previous studies (Farina et al., 2010; Jathar et al., 2011; Spracklen et al., 2011; Yu, 2011).

The AMS combines aerodynamic lens inlet technology with thermal vaporization and electron-impact mass spectrometry to provide measurements of speciated PM mass concentrations and size distributions. Canagaratna et al. (2007) described AMS measurement techniques and associated issues in detail. Factor analysis of AMS spectra can be used to divide OA into two groups: HOA and OOA. On the basis of many recent observations (Aiken, 2009; Aiken et al., 2008; Dzepina et al., 2009; Lanz et al., 2007; Zhang et al., 2005), I assume that POA is equivalent to the observed HOA and that SOA is equivalent to the observed OOA.

Figure 3.1 shows the scatter plots of the simulated concentrations versus the observed concentrations for $SO_4^{2-}$, $NO_3^-$, $NH_4^+$ and HOA (POA).

A global comparison of inorganic $SO_4^{2-}$, $NO_3^-$ and $NH_4^+$ aerosols provides an evaluation of the GEOS-Chem aerosol simulations in terms of transport and other depositional loss processes (Park et al., 2004). The statistical parameters, including the regression slope, correlation coefficient (R), normalized mean bias (NMB), normalized mean error (NME) and root mean square error (RMSE), between the observations and the model are summarized in Table 3.2. I find that the $SO_4^{2-}$ and $NH_4^+$ concentrations are generally in good agreement with the observations (NMBs are -2% and 48%, respectively), but the $NO_3^-$ concentrations are overestimated (NMB is 178%) in the model. This overestimation occurs mainly in Europe (NMB is 521%) where other inorganic $SO_4^{2-}$ and $NH_4^+$ aerosols are also overestimated. The NMB of $SO_4^{2-}$ is 46% and the NMB of $NH_4^+$ is 220%. This result is most likely due to the overestimated regional EMEP emission inventories in Europe. Overall, the model reproduces the inorganic concentrations well except for $NO_3^-$

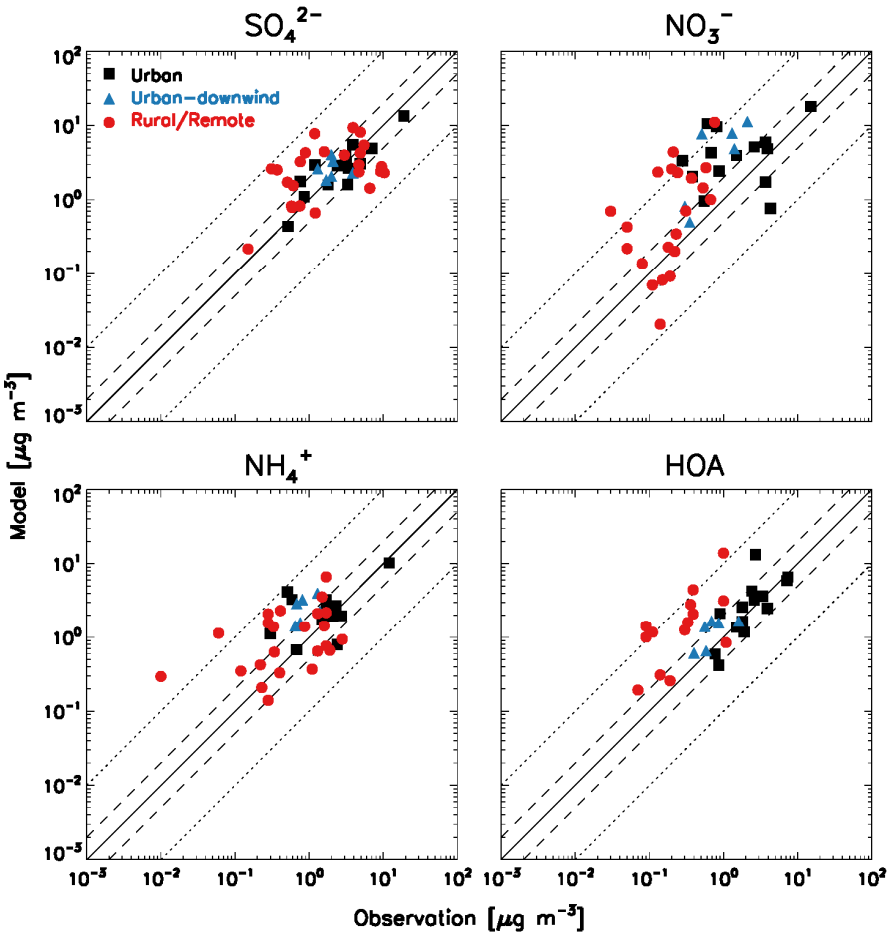


Figure 3.1. Scatter plots of the modeled (y-axis) versus observed (x-axis) $SO_4^{2-}$, $NO_3^-$, $NH_4^+$, and HOA. I multiply the carbon mass of OA by 2.1 to account for the non-carbon mass. I exclude observed HOA reported as 0.00 μg $m^{-3}$. Information on the AMS observation sites is given in Zhang et al. (2007) and Spracklen et al. (2011). The 1:1 line (solid), 2:1 lines (dashed), and 10:1 lines (dotted) are indicated.

Table 3.2. Statistical parameters for the evaluation of inorganic aerosols and HOA against AMS observations. Regressions are computed using the reduced-major-axis method (Hirsch and Gilroy, 1984).

| Type | Species | Data points | Slope | R | NMB | NME | RMSE |
|---|---|---|---|---|---|---|---|
| Urban | $SO_4^{2-}$ | 14 | 0.68 | 0.95 | -0.11 | 0.33 | 1.89 |
| | $NO_3^-$ | 14 | 1.23 | 0.67 | 0.90 | 1.19 | 4.24 |
| | $NH_4^+$ | 14 | 0.81 | 0.86 | 0.21 | 0.48 | 1.5 |
| | HOA | 14 | 1.59 | 0.49 | 0.26 | 0.52 | 2.97 |
| Urban Downwind | $SO_4^{2-}$ | 6 | -0.93 | -0.09 | 0.24 | 0.49 | 1.28 |
| | $NO_3^-$ | 6 | 5.91 | 0.79 | 4.55 | 4.55 | 5.66 |
| | $NH_4^+$ | 6 | 3.02 | 0.43 | 1.75 | 1.75 | 1.83 |
| | HOA | 6 | 1.15 | 0.61 | 0.61 | 0.61 | 0.61 |
| Rural | $SO_4^{2-}$ | 24 | 0.76 | 0.16 | 0.00 | 0.84 | 3.62 |
| | $NO_3^-$ | 23 | 11.71 | 0.63 | 4.87 | 5.06 | 2.54 |
| | $NH_4^+$ | 23 | 1.87 | 0.33 | 0.55 | 1.12 | 1.44 |
| | HOA | 14 | 9.7 | 0.56 | 5.22 | 5.30 | 3.8 |
| All | $SO_4^{2-}$ | 44 | 0.72 | 0.57 | -0.02 | 0.61 | 2.91 |
| | $NO_3^-$ | 43 | 1.64 | 0.63 | 1.78 | 2.02 | 3.71 |
| | $NH_4^+$ | 43 | 1.01 | 0.71 | 0.48 | 0.82 | 1.52 |
| | HOA | 34 | 1.78 | 0.43 | 0.85 | 1.07 | 3.11 |

concentrations, similar to previous GEOS-Chem evaluations conducted in East Asia (Jeong et al., 2010) and in the United States (Heald et al., 2012).

Because GEOS-Chem transports organic carbon (OC) mass as a tracer for POA, it is needed to convert the carbon mass of POA (POC) into the organic matter concentrations for the comparison with the AMS observations, which are provided as organic matter (OM) mass concentrations. For the conversion of POC into POM, I multipy the model POC concentrations by an OM/OC ratio of 2.1, following the method used in previous studies with GEOS-Chem (Henze et al., 2008; Pye et al., 2010; Pye and Seinfeld, 2010). Moreover, the model transports organic matter mass for SOA. Therefore, I do not need to apply the OM/OC ratio to SOA tracers. Figure 3.1 shows that the model overestimates the globally observed HOA (POA) concentrations; the NMB is 85%. It should be noted that NMBs are not significantly high in urban (26%) and urban downwind (61%) regions. The overestimation results primarily from rural regions (522%), where very low HOA concentrations are observed (this overestimation still exists if I apply a different OM/OC ratio, e.g., 1.4 (314%) and 1.6 (374%)). High bias in regions away from the source region implies that POA loss processes are missed in the model, especially in rural areas. Treating POA as semi-volatile rather than non-volatile species may reduce this discrepancy. This is discussed in Chapter 3.3.

Figure 3.2 compares the model results with the AMS observations of OOA (SOA) for selected cases, i.e., the VBS approach with aging constants

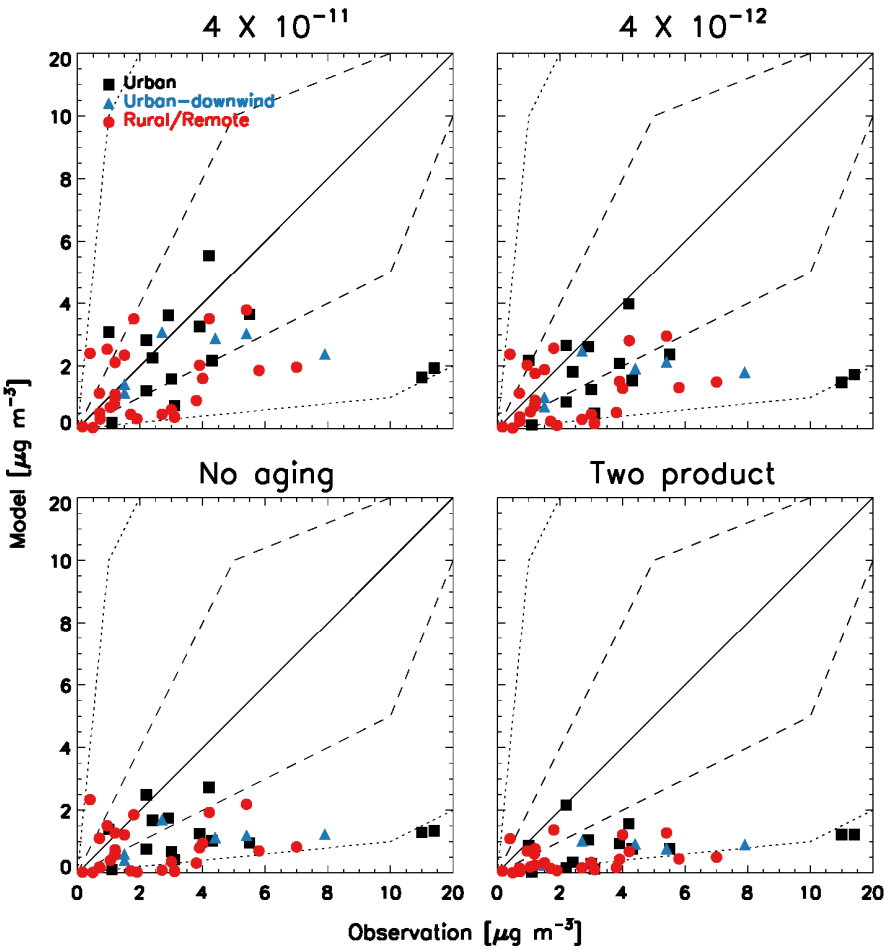


Figure 3.2. Scatter plots of the modeled (y-axis) versus observed (x-axis) OOA for selected cases - the VBS with aging constant of $4 \times 10^{-11}$ and $4 \times 10^{-12}$ $cm^3$ $molecule^{-1}$ $s^{-1}$, the VBS with no aging condition, and the two-product scheme. The 1:1 line (solid), 2:1 lines (dashed), and 10:1 lines (dotted) are indicated.

Table 3.3. Statistical parameters for the evaluation of OOA and TOA against AMS observations. The numbers of data points are given in parentheses.

| Type | Case | OOA | | | | | TOA | | | | |
|---|---|---|---|---|---|---|---|---|---|---|---|
| | | Slope | R | NMB | NME | RMSE | Slope | R | NMB | NME | RMSE |
| Urban (14) | 1 X $10^{-10}$ | -0.29 | -0.08 | -0.48 | 0.64 | 5.53 | 0.55 | 0.30 | -0.21 | 0.58 | 6.75 |
| | 4 X $10^{-11}$ | -0.28 | -0.06 | -0.50 | 0.64 | 5.54 | 0.55 | 0.30 | -0.22 | 0.58 | 6.75 |
| | 1 X $10^{-11}$ | -0.24 | -0.01 | -0.57 | 0.66 | 5.60 | 0.55 | 0.32 | -0.27 | 0.58 | 6.77 |
| | 4 X $10^{-12}$ | 0.20 | 0.02 | -0.63 | 0.68 | 5.68 | 0.55 | 0.34 | -0.30 | 0.59 | 6.81 |
| | 1 X $10^{-12}$ | 0.16 | 0.06 | -0.70 | 0.73 | 5.81 | 0.55 | 0.35 | -0.34 | 0.61 | 6.90 |
| | No aging | 0.15 | 0.06 | -0.74 | 0.76 | 5.92 | 0.55 | 0.35 | -0.37 | 0.63 | 6.98 |
| | Two product | 0.12 | 0.31 | -0.83 | 0.83 | 6.09 | 0.56 | 0.38 | -0.43 | 0.65 | 7.05 |
| Urban downwind (6) | 1 X $10^{-10}$ | 0.35 | 0.53 | -0.38 | 0.42 | 2.46 | 0.28 | 0.46 | -0.21 | 0.40 | 2.50 |
| | 4 X $10^{-11}$ | 0.34 | 0.53 | -0.41 | 0.44 | 2.54 | 0.28 | 0.45 | -0.24 | 0.41 | 2.55 |
| | 1 X $10^{-11}$ | 0.30 | 0.52 | -0.49 | 0.50 | 2.79 | 0.27 | 0.40 | -0.31 | 0.43 | 2.76 |
| | 4 X $10^{-12}$ | 0.27 | 0.50 | -0.57 | 0.57 | 3.03 | 0.26 | 0.35 | -0.37 | 0.45 | 2.96 |
| | 1 X $10^{-12}$ | 0.23 | 0.48 | -0.67 | 0.67 | 3.34 | 0.26 | 0.29 | -0.45 | 0.48 | 3.22 |
| | No aging | 0.19 | 0.48 | -0.73 | 0.73 | 3.56 | 0.24 | 0.25 | -0.51 | 0.51 | 3.42 |
| | Two product | 0.14 | 0.65 | -0.82 | 0.82 | 3.84 | 0.20 | 0.31 | -0.58 | 0.58 | 3.66 |
| Rural (27) | 1 X $10^{-10}$ | 0.63 | 0.39 | -0.39 | 0.64 | 1.93 | 1.51 | 0.55 | 0.18 | 0.64 | 2.57 |
| | 4 X $10^{-11}$ | 0.61 | 0.38 | -0.42 | 0.65 | 1.96 | 1.51 | 0.55 | 0.16 | 0.64 | 2.55 |
| | 1 X $10^{-11}$ | 0.55 | 0.34 | -0.48 | 0.68 | 2.05 | 1.48 | 0.53 | 0.10 | 0.65 | 2.53 |
| | 4 X $10^{-12}$ | 0.50 | 0.30 | -0.54 | 0.71 | 2.15 | 1.45 | 0.51 | 0.04 | 0.65 | 2.52 |
| | 1 X $10^{-12}$ | 0.43 | 0.22 | -0.62 | 0.74 | 2.30 | 1.42 | 0.49 | -0.03 | 0.65 | 2.53 |
| | No aging | 0.39 | 0.15 | -0.68 | 0.77 | 2.40 | 1.40 | 0.47 | -0.08 | 0.65 | 2.54 |
| | Two product | 0.22 | 0.28 | -0.82 | 0.84 | 2.56 | 1.42 | 0.47 | -0.21 | 0.65 | 2.63 |
| All (47) | 1 X $10^{-10}$ | 0.40 | 0.24 | -0.43 | 0.61 | 3.47 | 0.72 | 0.47 | -0.08 | 0.58 | 4.26 |
| | 4 X $10^{-11}$ | 0.38 | 0.25 | -0.45 | 0.62 | 3.49 | 0.72 | 0.47 | -0.10 | 0.58 | 4.26 |
| | 1 X $10^{-11}$ | 0.34 | 0.26 | -0.52 | 0.64 | 3.57 | 0.70 | 0.47 | -0.15 | 0.58 | 4.28 |
| | 4 X $10^{-12}$ | 0.29 | 0.26 | -0.58 | 0.67 | 3.66 | 0.69 | 0.46 | -0.20 | 0.59 | 4.31 |
| | 1 X $10^{-12}$ | 0.25 | 0.24 | -0.66 | 0.72 | 3.81 | 0.68 | 0.46 | -0.25 | 0.61 | 4.38 |
| | No aging | 0.22 | 0.22 | -0.71 | 0.76 | 3.92 | 0.68 | 0.45 | -0.29 | 0.62 | 4.44 |
| | Two product | 0.15 | 0.40 | -0.82 | 0.83 | 4.08 | 0.68 | 0.46 | -0.38 | 0.64 | 4.53 |

of $4 \times 10^{-11}$ and $4 \times 10^{-12}$ $cm^3$ $molecule^{-1}$ $s^{-1}$, the VBS approach with no aging, and the two-product scheme. The statistical parameters for all cases are presented in Table 3.3. First, the VBS with no aging yielded slightly lower RMSE and NME values than the two-product method because of the updated yield parameters. The simulated results that include aging are in better agreement with the observations than the simulations performed with no aging and the two-product scheme. The model performance is improved with an increase in the aging constant, i.e., lowered RMSE and NME, and increased R (Table 3.3). However, the model improvement is saturated beyond $4.0 \times 10^{-11}$ $cm^3$ $molecule^{-1}$ $s^{-1}$ because no significant differences are found in simulated results using the highest aging constant (i.e., $1 \times 10^{-10}$ $cm^3$ $molecule^{-1}$ $s^{-1}$).

In urban downwind and rural regions, R increases as the aging effect increases. This implies that aging reactions become significant as the photochemical aging time increases in the atmosphere. However, in urban regions, R decreases as the aging effect increases and becomes much lower than the R values in other regions. This result suggests that OOA concentrations in urban regions are significantly affected by local sources, which are subgrid-scale processes in the model because the spatial resolution (2°×2.5°) is too coarse to capture these sources. In contrast, in remote regions, grid-scale processes are more important. Therefore, the model reproduces the observed OOA concentrations relatively well in these locales.

By comparing OOA between the two-product scheme and the VBS approach with no aging, I find that the R values for the two-product scheme are higher than those for the VBS approach with no aging, indicating that the former is more successful at reproducing the observed variability even though the RMSE of the two-product scheme is higher than that of the VBS approach with no aging. Because neither method considers chemical aging of SOA, the difference in R between the simulations results primarily from the yield parameters, which should be investigated further to improve global models.

For total OA (TOA), the model is similar to that of OOA except that the R values are nearly equivalent. In summary, chemical aging reduces the low biases of the modeled OOA (from -71% to -43%) and TOA (from -29% to -8%), and its effect becomes more important farther away from the sources (i.e., R is increased from urban to the rural regions, as shown in Table 3.3).

### 3.2.2. United States

I use observations from the IMPROVE network for 1988-2012 to evaluate the model in the United States (Malm et al., 1994). Most of the sites are situated in rural regions measuring background concentrations of OA. The number of sites increased from 37 in 1988 to 219 in 2012. The data were observed every 3 days; more than 280,000 samples are used for the comparison. However, the IMPROVE network does not separate HOA and OOA and instead provides total OC concentrations, which are measured using the thermal optical reflectance (TOR) method (Chow et al., 1993). For comparison with the model results, I compute the observed monthly mean concentrations averaged on the $2^{o} \times 2.5^{o}$ model grid.

Figure 3.3 shows the scatterplots of the simulated versus observed OC concentrations, and the statistics are given in Table 3.4. The model with a high aging constant shows improved results; less scatter is found and the NMB is reduced from -30% to 2%. The R value also improves as the aging constant increases. I find that the NME slightly increases with the $1 \times 10^{-10}$ (0.43) and $4 \times 10^{-11}$ (0.42) $cm^3$ $molecule^{-1}$ $s^{-1}$ aging constants. However, these simulations are still better than those using either the two-product scheme (0.56) or the no aging cases (0.47). Statistical parameters show that the VBS approach with chemical aging is better than the other methods for

reproducing the observations in the United States.

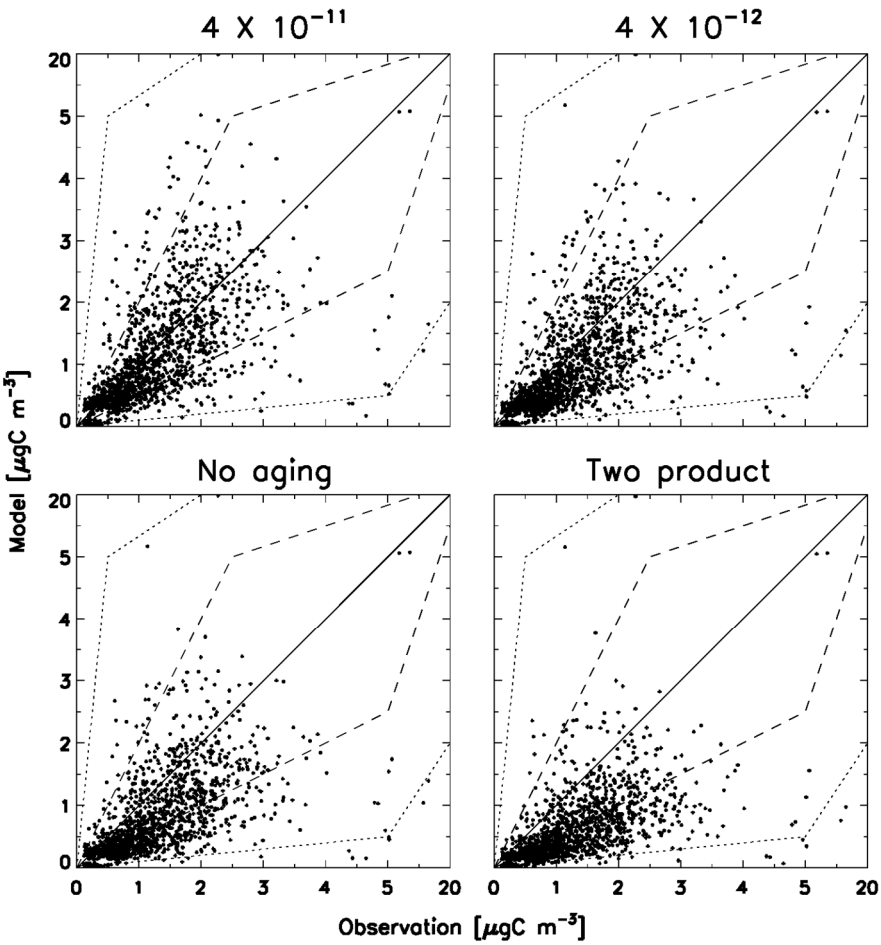


Figure 3.3. Scatter plots of OC concentrations between IMPROVE observations (x-axis) and the model (y-axis) for selected cases - the VBS with aging constant of $4 \times 10^{-11}$ and $4 \times 10^{-12}$ $cm^3$ $molecule^{-1}$ $s^{-1}$, the VBS with no aging condition, and the two-product scheme. The 1:1 line (solid), 2:1 lines (dashed), and 10:1 lines (dotted) are indicated. The number of points is 1394.

Table 3.4. Statistical parameters for the evaluation of OC against IMPROVE and EMEP observations.

| Case | IMPROVE OC | | | | | EMEP OC | | | | |
|---|---|---|---|---|---|---|---|---|---|---|
| | Slope | R | NMB | NME | RMSE | Slope | R | NMB | NME | RMSE |
| 1 X $10^{-10}$ | 1.20 | 0.50 | 0.02 | 0.43 | 0.97 | 0.47 | 0.27 | -0.42 | 0.53 | 3.05 |
| 4 X $10^{-11}$ | 1.17 | 0.50 | -0.02 | 0.42 | 0.96 | 0.47 | 0.27 | -0.44 | 0.54 | 3.10 |
| 1 X $10^{-11}$ | 1.11 | 0.49 | -0.10 | 0.41 | 0.94 | 0.45 | 0.26 | -0.48 | 0.56 | 3.19 |
| 4 X $10^{-12}$ | 1.06 | 0.48 | -0.17 | 0.42 | 0.93 | 0.44 | 0.26 | -0.51 | 0.58 | 3.26 |
| 1 X $10^{-12}$ | 1.02 | 0.47 | -0.25 | 0.44 | 0.95 | 0.44 | 0.27 | -0.55 | 0.61 | 3.34 |
| No aging | 0.99 | 0.46 | -0.30 | 0.47 | 0.97 | 0.43 | 0.28 | -0.58 | 0.63 | 3.39 |
| Two product | 0.87 | 0.42 | -0.47 | 0.56 | 1.05 | 0.34 | 0.28 | -0.68 | 0.70 | 3.65 |

### 3.2.3. Europe

Figure 3.4 shows the comparison of the model results with monthly mean observations of OC at EMEP sites for 2002-2003 (Yttri et al., 2007). The EMEP also provides total OC concentrations, which were measured using the thermal optical transmittance (TOT) method (Birch and Cary, 1996).

Similar to the comparison with the United States, including chemical aging reduces biases and errors in the model simulations (Table 3.4). However, in contrast to the IMPROVE comparison, R remains unchanged, and the model continues to underestimate OC concentrations. The model appears to be better in the United States than Europe because IMPROVE sites in the United States are primarily situated in rural areas. The mean OC concentration from IMPROVE is 1.19 μgC $m^{-3}$, three times lower than the OC concentration from EMEP (3.83 μgC $m^{-3}$). As discussed in Chapter 3.2.1, the model reproduces observations well in downwind and rural areas, where grid-scale processes are dominant.

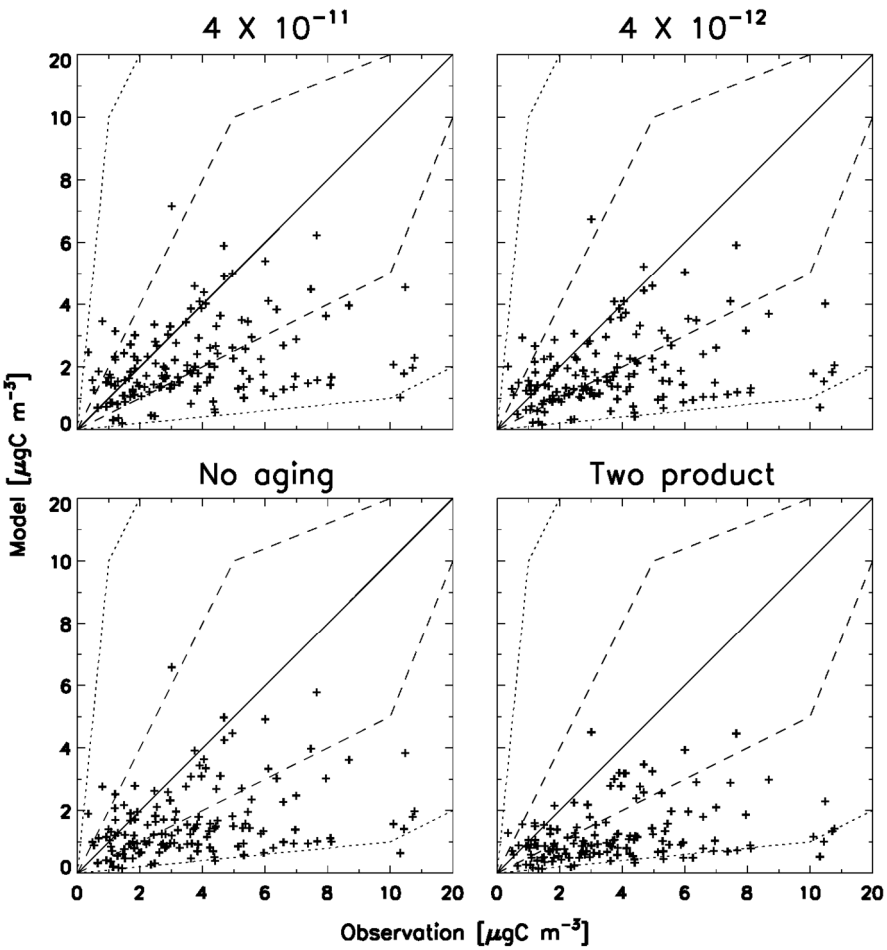


Figure 3.4. Scatter plots of OC concentrations between EMEP observations (x-axis) and the model (y-axis) for selected cases - the VBS with aging constant of $4 \times 10^{-11}$ and $4 \times 10^{-12}$ $cm^3$ $molecule^{-1}$ $s^{-1}$, the VBS with no aging condition, and the two-product scheme. The 1:1 line (solid), 2:1 lines (dashed), and 10:1 lines (dotted) are indicated. The number of points is 142.

### 3.2.4. East Asia

Long-term observations of OA in East Asia are unavailable. Instead, I collect episodic OC and WSOC data measured on relatively short-term periods from the literature. For the evaluation of SOA in the model, I use observed WSOC concentrations, which can be used as a proxy for SOA (Sullivan et al., 2006; Weber et al., 2007). However, WSOC concentrations are not entirely SOA in the atmosphere because some POA species, especially those from biomass burning, may be soluble (Sullivan et al., 2006; Sullivan et al., 2004; Weber et al., 2007). Therefore, the observed WSOC concentrations should be regarded as the upper limit of SOA concentrations. However, the annual biomass-burning contribution to OC is relatively minor in East Asia (Jeong et al., 2010). I also compare the observed and simulated OC concentrations in East Asia as an alternative validation of the model.

Figure 3.5 displays a comparison of the simulated and observed WSOC concentrations over East Asia. The statistical parameters of the OC and WSOC comparison are listed in Table 3.5. I find that the model underestimates the observed WSOC (NMB: -84% to -70%) and OC (NMB: -70% to -60%) regardless of the chemical aging constant used. This underestimation results because the observations in East Asia were mainly from highly polluted urban regions (e.g., Beijing and Guangzhou) and

resolution of the model is too coarse to simulate the high concentrations from heavily polluted megacities – the observed mean concentration of OC

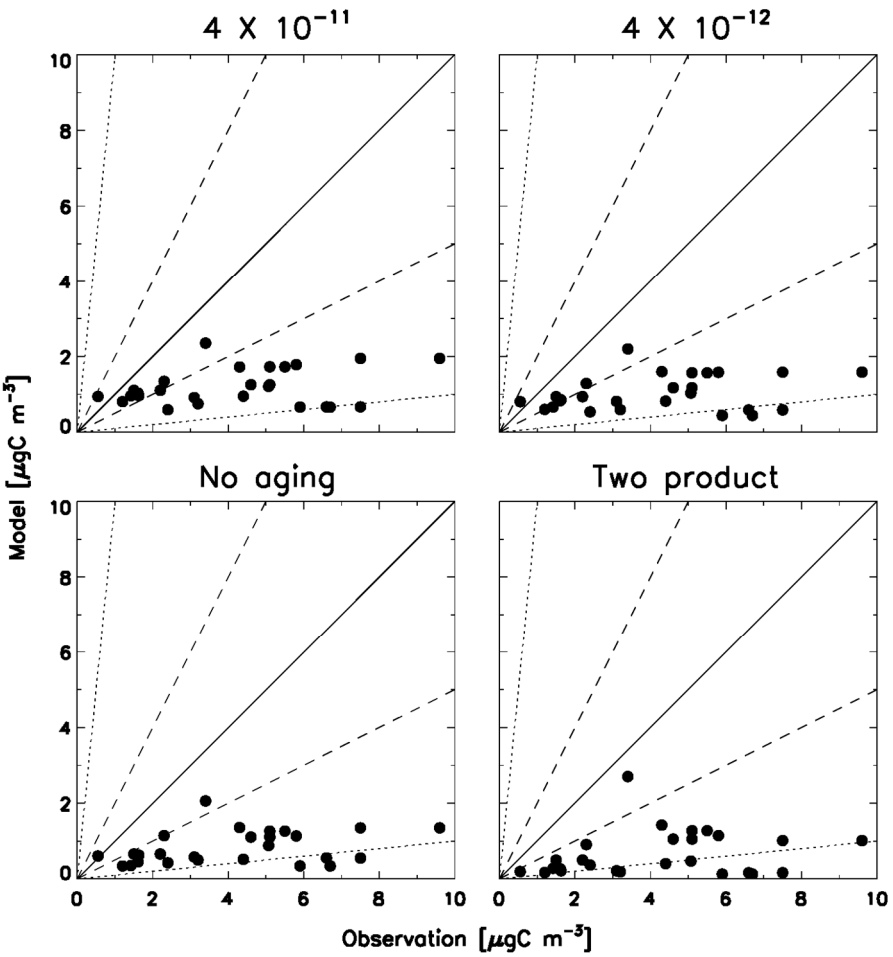


Figure 3.5. Scatter plots of WSOC concentrations between observations (x-axis) and the model (y-axis) over East Asia for selected cases - the VBS with aging constant of $4 \times 10^{-11}$ and $4 \times 10^{-12}$ $cm^3$ $molecule^{-1}$ $s^{-1}$, the VBS with no aging condition, and the two-product scheme. The 1:1 line (solid), 2:1 lines (dashed), and 10:1 lines (dotted) are indicated.

Table 3.5. Statistical parameters for the evaluation of OC against OC and WSOC observations collected over East Asia. The number of observation points is given in parenthesis.

| Case | OC (57) | | | | | WSOC (27) | | | | |
|---|---|---|---|---|---|---|---|---|---|---|
| | Slope | R | NMB | NME | RMSE | Slope | R | NMB | NME | RMSE |
| 1 X $10^{-10}$ | 0.27 | 0.63 | -0.66 | 0.66 | 12.35 | 0.21 | 0.31 | -0.70 | 0.71 | 3.66 |
| 4 X $10^{-11}$ | 0.27 | 0.63 | -0.66 | 0.66 | 12.38 | 0.21 | 0.29 | -0.71 | 0.72 | 3.69 |
| 1 X $10^{-11}$ | 0.27 | 0.63 | -0.66 | 0.67 | 12.45 | 0.20 | 0.26 | -0.73 | 0.74 | 3.78 |
| 4 X $10^{-12}$ | 0.27 | 0.63 | -0.67 | 0.68 | 12.50 | 0.20 | 0.25 | -0.75 | 0.76 | 3.84 |
| 1 X $10^{-12}$ | 0.27 | 0.63 | -0.68 | 0.68 | 12.58 | 0.19 | 0.28 | -0.78 | 0.78 | 3.92 |
| No aging | 0.27 | 0.64 | -0.68 | 0.69 | 12.63 | 0.19 | 0.32 | -0.80 | 0.80 | 3.99 |
| Two product | 0.27 | 0.62 | -0.70 | 0.70 | 12.82 | 0.26 | 0.20 | -0.84 | 0.84 | 4.16 |

is 14.19 μgC $m^{-3}$ and that of WSOC is 4.16 μgC $m^{-3}$. The observed mean WSOC concentration over East Asia is even higher than the mean OC concentration from IMPROVE (1.19 μgC $m^{-3}$) and EMEP (3.83 μgC $m^{-3}$). Second, although there are slight improvements in the statistical parameters (NME from 84 to 71% and RMSE from 4.16 to 3.66 μgC $m^{-3}$) after the inclusion of chemical aging, they are very limited. The model still shows significant low biases with the highest aging constant, indicating the possibility of missing sources of SOA in East Asia (Liu et al., 2012).

### 3.2.5. Discussion

In the evaluations above, the VBS approach with chemical aging shows better agreement with the observations in terms of mean mass concentrations (NMB) and errors (NME and RMSE). However, the model performance differs regionally. In polluted urban regions, the model significantly underestimates the observed OA, and R is also low. In clean rural areas, the model reproduces the observed OA with high R values and small biases.

Comparisons between the observations and the model results with different aging constants allow us to provide a constraint on the aging constants for the VBS approach. I find that the simulation using $4 \times 10^{-11}$ $cm^3$ $molecule^{-1}$ $s^{-1}$ agrees best with the global SOA observations despite significant biases in some regions. The model with the highest aging constant, i.e., $1 \times 10^{-10}$ $cm^3$ $molecule^{-1}$ $s^{-1}$, exhibits a similar performance, and less improvement is observed in some regions compared to simulations using $4 \times 10^{-11}$ $cm^3$ $molecule^{-1}$ $s^{-1}$. Furthermore, the $1 \times 10^{-10}$ $cm^3$ $molecule^{-1}$ $s^{-1}$ aging constant has never been used in previous studies because it is too high. Therefore, I recommend the use of $4 \times 10^{-11}$ $cm^3$ $molecule^{-1}$ $s^{-1}$ with the VBS approach. All of the results below are from the model with this value, including a semi-volatile POA simulation, global budget analysis, and DRE estimation.

Although the use of chemical aging reduces the gap between the model and the observations, the model still underestimates the observed SOA concentrations, indicating the existence of missing SOA formation processes, e.g., aqueous-phase oxidation (Carlton et al., 2008; Washenfelder et al., 2011) and acid catalysis reactions of SOA from glyoxal (Liggio et al., 2005). The reported glyoxal imbalance between model simulations and observations can increase equivalent SOA mass by a few μg $m^{-3}$ in urban areas, e.g., Mexico City (Volkamer et al., 2007). Furthermore, the model does not include other potential parent VOCs. For example, MBO, a potential parent VOC, has recently been reported as a possible source of SOA (H. Zhang et al., 2012). Further investigation is needed to examine these missing processes through observations and improved models.

The simulated planetary boundary layer (PBL) and its related mixing processes can also cause a gap between model simulations and observations. Lin and McElroy (2010) showed that changing the PBL mixing scheme can reduce model biases over the United States by more than 10 ppb for surface ozone concentrations at night and by 2-5 ppb during the afternoon. However, computing the PBL height is difficult because the PBL height differs between algorithms approximately by a factor of 3 or 4, or more than 1 km (Seidel et al., 2010). More investigation is needed to calculate the appropriate PBL heights through improved observational methods and model schemes.

In this work, the VBS scheme accounts for the functionalization

process. The recently proposed two-dimensional volatility basis set (2D-VBS) can simulate both functionalization and fragmentation processes (Donahue et al., 2011; Donahue et al., 2012a; Donahue et al., 2012b; Murphy et al., 2012). However, a simplified functionalization scheme (analogous to the 1D-VBS approached used in this work) still showed a better performance than a functionalization and fragmentation scheme (Murphy et al., 2012), which requires too many parameterizations (e.g., functionalization kernel and functionalization/fragmentation branching ratio) that are poorly constrained.

## 3.3. Semi-volatile POA simulations

As discussed in Chapter 3.2, a significant overestimation of POA occurs in rural areas, possibly due to the absence of semi-volatile POA in the model. To examine the simulated sensitivity to semi-volatile POA, I conduct sensitivity model simulations using the VBS approach. I adopt an approach proposed by Robinson et al. (2007) even though their method possesses a high level of uncertainty, especially in the estimates of intermediate-volatility organic compounds (IVOCs) and semi-volatile organic compounds (SVOCs). In addition, it is computationally expensive. To resolve these issues, I suggest a simple approach to account for the semi-volatility of POA. The details are described below.

### 3.3.1. Semi-volatile POA simulation with the VBS approach

Based on the VBS approach, I add three more species with higher volatility, resulting in 9 volatility bins: $[C^*_i] = [0.01, 0.1, 1, 10, 100, 1000, 10000, 100000, 1000000]$ μg $m^{-3}$. The three highest volatility bins are used to represent IVOCs, and the others are used to represent SVOCs. The semi-volatile POA is partitioned into these volatility bins using normalized emission factors: [0.03, 0.06, 0.09, 0.14, 0.18, 0.30, 0.40, 0.50, 0.80]. The sum of these factors is 2.5. The semi-volatile POA emission amounts to 2.5 times the non-volatile POA emissions estimated from diesel emission profiles (Jathar et al., 2011; Robinson et al., 2007; Shrivastava et al., 2008; Tsimpidi et al., 2010). As a result, all POAs and SOAs are considered as semi-volatile compounds.

I separate semi-volatile POA into fresh POA (emitted directly from the sources) and oxidized POA (oxidized with the hydroxyl radical). I assume fresh POA to be HOA and oxidized POA to be OOA, as described by Shrivastava et al. (2008) and Murphy and Pandis (2009). The mass increase after one oxidation process is 7.5%, according to Robinson et al. (2007). For the aging of semi-volatile POA, I use an aging constant of $4 \times 10^{-11}$ $cm^3$ $molecule^{-1}$ $s^{-1}$, which is the most widely used for semi-volatile POA aging

(Bergstrom et al., 2012; Jathar et al., 2011; Murphy et al., 2011; Murphy and Pandis, 2010; Robinson et al., 2007; Shrivastava et al., 2008; Tsimpidi et al., 2010)

Table 3.6 summarizes the statistics from the comparison between the semi-volatile POA simulation and the AMS observations. Compared with the previous results shown in Table 3.2 and Table 3.3, the model shows an improvement, especially for HOA concentrations. Specifically, the simulated high bias with non-volatile POA (RMSE of 3.11) is reduced after using semi-volatile POA (RMSE of 1.85). In general, the biases in the model are decreased. However, the remaining discrepancies between the model simulation and observations are highly region dependent. For example, the simulated HOA concentrations are higher than the observations in urban and urban downwind regions (Table 3.2) and are now lower than the observations (-75% and -72% for urban and urban-downwind regions, respectively), whereas the high bias in the rural regions (522%) is greatly reduced (-20%).

Table 3.6. Statistical parameters for the semi-volatile simulation results against the OA of the AMS observations.

| Type | Species | With the VBS | | | | | Simple conversion | | | | |
|---|---|---|---|---|---|---|---|---|---|---|---|
| | | Slope | R | NMB | NME | RMSE | Slope | R | NMB | NME | RMSE |
| Urban | HOA | 0.32 | 0.37 | -0.75 | 0.75 | 2.82 | 0.72 | 0.44 | -0.42 | 0.59 | 2.24 |
| | OOA | 0.5 | 0.28 | -0.20 | 0.63 | 4.74 | 0.43 | 0.23 | -0.22 | 0.63 | 4.81 |
| | TOA | 0.42 | 0.3 | -0.40 | 0.59 | 7.08 | 0.48 | 0.3 | -0.29 | 0.58 | 6.84 |
| Urban Downwind | HOA | 0.37 | 0.33 | -0.72 | 0.72 | 0.67 | 0.7 | 0.54 | -0.30 | 0.37 | 0.41 |
| | OOA | 0.42 | 0.48 | -0.23 | 0.40 | 2.2 | 0.38 | 0.53 | -0.27 | 0.40 | 2.24 |
| | TOA | 0.39 | 0.38 | -0.31 | 0.42 | 2.75 | 0.29 | 0.46 | -0.28 | 0.39 | 2.63 |
| Rural | HOA | 1.38 | 0.46 | -0.20 | 0.77 | 0.45 | 3.7 | 0.54 | 0.80 | 1.35 | 1.18 |
| | OOA | 1.36 | 0.64 | 0.18 | 0.57 | 1.92 | 1.11 | 0.61 | 0.04 | 0.54 | 1.68 |
| | TOA | 1.37 | 0.65 | 0.16 | 0.59 | 2.12 | 1.4 | 0.58 | 0.13 | 0.61 | 2.33 |
| All | HOA | 0.32 | 0.47 | -0.68 | 0.75 | 1.85 | 0.77 | 0.5 | -0.27 | 0.65 | 1.63 |
| | OOA | 0.72 | 0.43 | -0.05 | 0.57 | 3.07 | 0.61 | 0.42 | -0.12 | 0.56 | 3.02 |
| | TOA | 0.58 | 0.44 | -0.20 | 0.57 | 4.3 | 0.64 | 0.46 | -0.15 | 0.56 | 4.23 |

The NMB of HOA in all regions is -68%, indicating that the fresh POA concentration is low, as semi-volatile POA aging reactions occur too rapidly. A smaller aging constant for semi-volatile POA may reduce this bias (i.e., more semi-volatile POA remains as fresh POA), even though the $4 \times 10^{-11}$ $cm^3$ $molecule^{-1}$ $s^{-1}$ aging constant was best for SOA.

In contrast, the low bias of the simulated OOA is greatly reduced in urban and urban downwind regions. However, the model slightly overestimates the observed OOA in rural regions. These changes in simulated OOA concentrations are also consistent with those of HOA, indicating rapid semi-volatile POA aging reactions. The R values for all regions are slightly improved for HOA (0.47 from 0.43) and OOA (0.43 from 0.25). However, R is decreased slightly for TOA (0.44 from 0.47).

The consideration of semi-volatile POA does not result in a dramatic improvement in terms of TOA concentrations. However, including semi-volatile POA results in a significant improvement in both HOA and OOA concentrations, which is consistent with previous studies (Jathar et al., 2011; Robinson et al., 2007). As a result, the simulation with the semi-volatile POA better reproduces the observed HOA/OOA ratio. This result is reasonable because the simulation of semi-volatile POA does not include the

total OA and instead allows for POA/SOA reclassification.

### 3.3.2. Direct conversion of POA to SOA

Here, I suggest a simple approach that uses an additional POA (oxygenated POA) tracer to represent semi-volatile POA. Most chemical transport models employ two POA tracers: hydrophobic and hydrophilic POAs. Chemical oxidation and mixing with other soluble aerosols are important processes for changing the hydrophobicity of POA species. Thus, I consider more oxidation in the atmosphere. Therefore, hydrophilic POA is further oxidized to become oxygenated POA, which is analogous to SOA formed from semi-volatile POA, as discussed above. This conversion is simulated using an oxidation process by an OH radical with a rate constant of $4 \times 10^{-11}$ $cm^3$ $molecule^{-1}$ $s^{-1}$ (the same value as in Chapter 3.3.1). Accompanying mass increases for each oxidation process are accounted for using different organic matter to organic carbon (OM/OC) ratios for each POA tracer. I apply different OM/OC ratios, i.e., 1.2 for hydrophobic, 1.8 for hydrophilic, and 2.4 for oxygenated POA, to maintain consistency with the study by Turpin and Lim (2001). They reported that the OM/OC ratios were $1.6 \pm 0.2$ for urban aerosols and $2.1 \pm 0.2$ for nonurban aerosols. In the model, the OM/OC ratio is close to 1.5 in nearby source regions and 2.4 in remote regions where most of the POA is oxidized. These OM/OC ratios are

also within the range measured by Aiken et al. (2008).

The mass increases per one oxidation reaction are 50% (1.8/1.2) for hydrophobic to hydrophilic conversion and 33% (2.4/1.8) for hydrophilic to oxygenated conversion. These increases are comparable to the 50% mass increase suggested by Pye and Seinfeld (2010) and the 40% mass increase suggested by Grieshop et al. (2009). Note that the oxidation reaction occurs in the gas phase in other studies (Grieshop et al., 2009; Pye and Seinfeld, 2010; Robinson et al., 2007). However, this simple approach oxidizes aerosol tracers because it carries only aerosols.

As shown in Table 3.6, the results of the direct conversion are similar to the results reported in Chapter 3.3.1. The HOA concentrations in urban and urban-downwind regions are lower than the observations. However, the magnitude of the low bias is reduced (-42% for urban). The HOA concentrations in rural regions are higher (80%) than those of the observations, indicating that the conversion rate of fresh POA to oxygenated POA in the simple conversion case is lower than that in the case of semi-volatile POA with the VBS approach.

RMSEs are greatly improved in all regions in terms of OOA and HOA. However, the simulated TOA results are slightly worse than the results of the non-volatile POA simulation. Similar to Chapter 3.3.1, the inclusion of semi-volatile POA improves the model performance in terms of HOA/OOA, but the performance of the model remains similar for TOA.

In the comparisons above, I demonstrate that the simple conversion

approach can be as effective as the semi-volatile POA simulations suggested by Robinson et al. (2007), and sometimes even better, especially considering computational efficiency. Although the consideration of semi-volatile POA in both methods does not produce significant improvements in terms of total OA predictions, it does show significant improvements in the HOA/OOA ratios. This is consistent with the results by Jathar et al. (2011) who showed that the simulated SOA to OA ratios were greatly increased and approached the observed ratios after including semi-volatile POA in the simulations.

## 3.4. Global budgets of OA species

I estimate the global budgets of OA species using three different models: the best model with the $4 \times 10^{-11}$ $cm^3$ $molecule^{-1}$ $s^{-1}$ aging constant, the model with the VBS approach with no aging, and the model with the two-product method. The tabulated global source of SOA species using the two-product approach is 23.3 Tg $yr^{-1}$. The estimates using the two-product approach here are also consistent with the 23-30.3 Tg $yr^{-1}$ range reported in previous studies (Henze et al., 2008; Pye and Seinfeld, 2010).

Table 3.7 summarizes the simulated results of the OA budgets. Here, I focus mainly on values of the SOA species because the POA values are identical among the three models. A comparison between the VBS approach with no aging and the two-product scheme shows the effect of the updated yield parameters. A comparison between the model with aging ($4 \times 10^{-11}$ $cm^3$ $molecule^{-1}$ $s^{-1}$) and with no aging shows the effect of chemical aging. I find that the model with aging yields the highest total SOA production, i.e., 39.9 Tg $yr^{-1}$, which is 1.5 times higher than the 26.0 Tg $yr^{-1}$ predicted by the no aging model. Moreover, the updated yield parameters result in relatively minor enhancements in SOA production relative to the two-product model (23.3 Tg $yr^{-1}$).

As expected from the comparison above, the SOA burden with aging

(1.16 Tg) is 30% higher than that with no aging (0.89 Tg). However, this increase is substantially smaller than that for the production of SOA (53% increase) mainly because of the volatility distribution change in SOA. In

Table 3.7. Annual global OA budgets of the VBS approach with aging ($4x10^{-11}$ $cm^3$ $molecule^{-1}$ $s^{-1}$), the VBS approach with no aging and the two-product approach. I multiply the carbon mass of POA by 2.1 to account for non-carbon mass. The burden of gas phase semi-volatiles is listed in parentheses. The net production rate is assumed equal to the deposition flux.

| SOA scheme | 4 x $10^{-11}$ | No aging | Two-product |
|---|---|---|---|
| Production [Tg $yr^{-1}$] | | | |
| - POA | 47.8 | 47.8 | 47.8 |
| - SOA | 39.9 | 26.0 | 23.3 |
| Burden [Tg] | | | |
| - POA | 0.800 | 0.800 | 0.800 |
| - SOA | 1.159 (1.419) | 0.889 (1.722) | 0.908 (1.924) |
| C* = $10^{-2}$ μg $m^{-3}$ | 0.087 (0.001) | | |
| C* = $10^{-1}$ μg $m^{-3}$ | 0.119 (0.004) | | |
| C* = $10^{0}$ μg $m^{-3}$ | 0.332 (0.062) | 0.222 (0.056) | |
| C* = $10^{1}$ μg $m^{-3}$ | 0.274 (0.190) | 0.244 (0.208) | |
| C* = $10^{2}$ μg $m^{-3}$ | 0.186 (0.381) | 0.216 (0.476) | |
| C* = $10^{3}$ μg $m^{-3}$ | 0.161 (0.781) | 0.207 (0.982) | |
| Wet deposition [Tg $yr^{-1}$] | | | |
| - POA | 39.4 | 39.4 | 39.4 |
| - SOA | 35.1 | 22.9 | 20.7 |
| Dry deposition [Tg $yr^{-1}$] | | | |
| - POA | 8.4 | 8.4 | 8.4 |
| - SOA | 4.8 | 3.0 | 2.6 |
| Life time [s] | | | |
| - POA | 6.6 | 6.6 | 6.6 |
| - SOA | 10.6 | 12.5 | 14.2 |

comparison with the no aging case, the volatility distribution for the aging case shifts toward low saturation vapor pressure bins (Table 3.7). Therefore, the aerosol phase is more favorable in the aging case. SOA from the model with aging is more concentrated in the boundary layer where vertical transport is very limited by wet deposition processes, especially in the form of aerosols. Consequently, the lifetime of SOA with aging (10.6 days) is shorter relative to that of SOA with no aging (12.5 days). Similarly, the SOA burden of the no aging case is slightly lower than that predicted using the two-product scheme although the SOA production of the no aging case is higher than that predicted using the two-product method.

Kanakidou et al. (2005) previously estimated 12–70 Tg $yr^{-1}$ of SOA production based on global model simulations with no chemical aging of SOA. Farina et al. (2010) estimated 38.1 Tg $yr^{-1}$ of global SOA production with chemical aging of SOA. Although the best estimate of global SOA production with the VBS approach (39.9 Tg $yr^{-1}$) is higher than that of the two-product scheme (23.3 Tg $yr^{-1}$), it is still lower than the top-down estimates of 50–380 Tg $yr^{-1}$ by Spracklen et al. (2011), obtained using AMS observations and the GLOMAP global chemical transport model. The best estimate of the global OA source using the VBS approach (87.7 Tg $yr^{-1}$) is also lower than the top-down estimate of 315 Tg $yr^{-1}$ by Heald et al.

(2010)[①], estimated based on satellite observations of aerosol optical depth. The global SOA burden using the VBS approach is 1.16 Tg, higher than the 0.98 Tg given by Farina et al. (2010) and lower than the top-down estimate (1.84 Tg) of Spracklen et al. (2011). Finally, the OA burden is 1.96 Tg, slightly higher than the 1.7 Tg from the AeroCom multi-model mean (Textor et al., 2006) but lower than the 5.3 Tg estimated by Heald et al. (2010)[1]. The lifetime of OA in the model is 8.2 days, which is within the range (4.3–11 days) of the AeroCom multi-model study (Textor et al., 2006) and slightly lower than the 9.4 days reported by Farina et al. (2010).

It has been reported that models underestimate SOA concentrations in the free troposphere as well as the boundary layer (Heald et al., 2005; Heald et al., 2011). To examine the effect of chemical aging on SOA in the free troposphere, I plot the increased (aging minus no aging) SOA concentrations in the boundary layer and free troposphere in Figure 3.6. Increases of SOA concentrations are spatially consistent with that of aromatic VOC emissions (Henze et al., 2008), reflecting only the chemical aging of anthropogenic SOA. In the boundary layer, the SOA concentrations are increased to 1.50 μg $m^{-3}$, with a global mean increase of 0.10 μg $m^{-3}$. However, in the free troposphere, this increase is reduced with a global mean increase of 0.04 μg $m^{-3}$ and a maximum increase of 0.20 μg $m^{-3}$. I find that the aerosol phase fraction of semi-volatiles in the aging case is 45%, much higher than that of semi-volatiles with no aging (34%). Due to limited upward transport by the

① I apply an OM/OC ratio of 2.1 to convert TgC to Tg

accompanying wet scavenging with vertical updrafts, the SOA concentration increase due to the chemical aging is reduced as altitude increases.

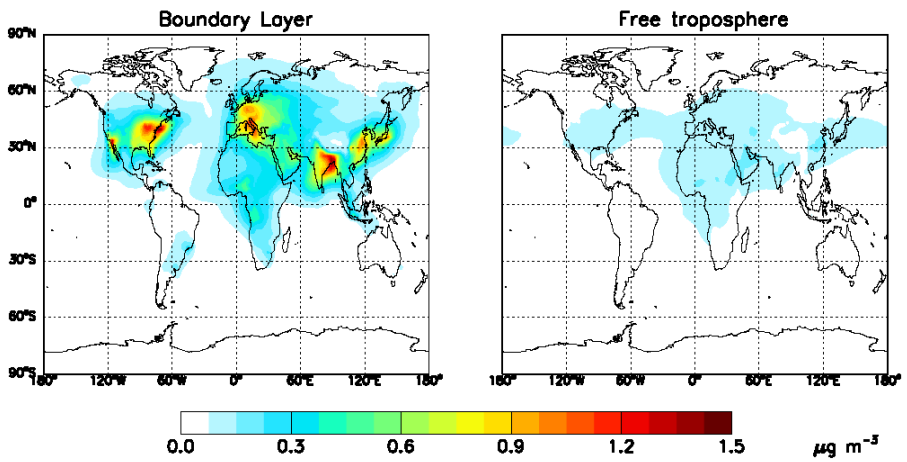


Figure 3.6. The SOA difference map between the VBS with aging ($4 \times 10^{-11}$ $cm^3$ $molecule^{-1}$ $s^{-1}$) and no aging case. The left panel shows the difference in boundary layer (0-1 km) and the right panel shows the difference in free troposphere (2-6.5 km).

## 3.5. Effect of chemical aging on global DRE of SOA

I use the best estimate of SOA concentrations in Chapter 3.4 to compute the clear-sky DRE of SOA at the top of the atmosphere. I first compute the aerosol optical depths (AODs) at 19 spectral wavelength bands for the radiative transfer calculation using the MIE algorithm package (Wiscombe, 1980). A refractive index of 1.53–0.005i, an effective radius of 0.0212 μm, and a density of 1.8 g $cm^{-3}$ are used for all OA species in this calculation (Chin et al., 2002). I use aerosol hygroscopic growth factors from Chin et al. (2002). Then, the calculated AODs at 19 wavelengths (ranging from 0.2 to 4.4 μm) are used in the National Center for Atmospheric Research Column Radiation Model version 2 (NCAR CRM2) for the DRE calculation. The meteorological input data needed for the computation are obtained from the GEOS-5 assimilated meteorological data.

The left panel of Figure 3.7 shows the DRE of SOA for the no aging scenario. The spatial pattern of DRE reflects the aerosol concentrations; the highest DRE values occur in the Northern Hemisphere and in active biomass-burning regions. The area-weighted global mean value is -0.21 W $m^{-2}$, indicating the cooling effect on the Earth's climate.

The right panel of Figure 3.7 shows the changes in DRE of SOA as a result of chemical aging reactions (i.e., DRE of SOA with aging minus that of SOA with no aging). Because the chemical aging adds to the SOA

concentrations, the global mean DRE of SOA is decreased to -0.28 W $m^{-2}$.

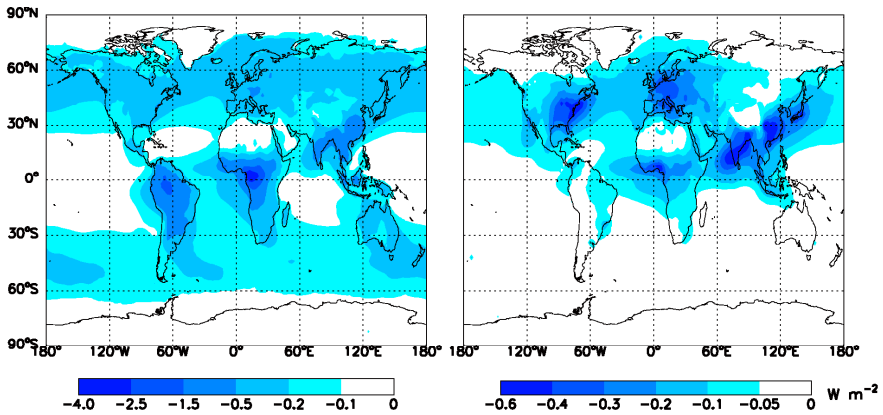


Figure 3.7. Simulated DRE of SOA without aging (left) and increased DRE of SOA after considering chemical aging (right) at the top of the atmosphere (TOA).

The spatial pattern of DRE change is similar to Figure 3.6. Notably, the global mean decrease in the SOA DRE because of chemical aging is -0.07 W $m^{-2}$, comparable to the AeroCom multi-model mean DRF of OA (-0.13 W $m^{-2}$) (Schulz et al., 2006). The AeroCom DRF was calculated based on the difference between pre-industrial and industrial OA concentrations, assuming that SOA is 100% biogenic. Therefore, the anthropogenic SOA DRF is assumed to be negligible in the AeroCom study and in the IPCC AR4 report (Forster et al., 2007).

The effect of chemical aging on the DRE of SOA is more important regionally, especially for industrialized regions, e.g., the eastern United States (-0.29 W $m^{-2}$ over 100°W -70°W, 25°N -50°N), western Europe (-0.20 W $m^{-2}$ over 10°W -50°E, 35°N -70°N), and East Asia (-0.17 W $m^{-2}$ over 100°E -150°E, 10°N -50°N). These increased regional DRE values of SOA are 2.5-4 times higher than the globally increased mean DRE value, which has important implications for regional climates.

## 3.6. Summary

SOA is globally more dominant than POA. However, the SOA formation process and properties are still poorly understood. As a result, SOA models have typically significantly underestimated observations. Global SOA models using the two-product method have not yet considered the chemical aging of SOA, which many studies have shown to be important.

In this Chapter, I implemented the VBS approach for SOA simulation in GEOS-Chem to simulate the chemical aging of SOA and examined its effects on the SOA burden and its climate implications. Using the model with different aging conditions, I conducted extensive evaluations of the model by comparison with observations in various regions (global, the United States, Europe, East Asia) and found that the model with the $4 \times 10^{-11}$ $cm^3$ $molecule^{-1}$ $s^{-1}$ aging constant is most suitable for simulating SOA aging with the VBS approach. I also tested two semi-volatile POA simulations, i.e., the semi-volatile POA with the VBS approach and the simple conversion of POA to SOA. Both simulations showed improved results in terms of HOA and OOA but failed to improve the model results in terms of TOA.

I used the model results to analyze the effect of chemical aging on the global budgets of SOA. The inclusion of chemical aging increased the global SOA production by 53%, from 26.0 Tg $yr^{-1}$ to 39.9 Tg $yr^{-1}$. Moreover,

the global SOA burden was increased by 30%, from 0.89 Tg to 1.16 Tg. Chemical aging reduced the gap between the observation and the model and substantially increased the SOA production relative to previous studies. However, the model still underestimated the observations in urban regions and in the free troposphere, indicating possible missing sources. Further investigation of SOA formation (e.g., in-cloud processing) is needed through observations and improved models.

I computed the DRE of SOA species with aging and no aging conditions. The effect of chemical aging on the global mean SOA DRE was -0.07 W $m^{-2}$, comparable to the AeroCom multi-model mean OA DRF of -0.13 W $m^{-2}$. Because of its patch-like distribution, it is more important regionally, especially for industrialized regions. The DRE decreased over the eastern United States, western Europe, and East Asia because chemical aging was 2.5-4 times higher than the globally decreased mean DRE.

# Chapter 4. A global simulation of brown carbon

In this Chapter, I estimate global primary BrC emissions from open burning and biofuel use based on a reported relationship between AAE and modified combustion efficiency (MCE) (McMeeking, 2008). In addition to the primary source above, I also consider SOC produced from aromatic oxidation as a secondary source of BrC (Hecobian et al., 2010; Jaoui et al., 2008; Lin et al., 2015; Nakayama et al., 2010; Nakayama et al., 2013; Zhong and Jang, 2011). Based on these sources, a global distribution of BrC concentrations is explicitly simulated for the entire year of 2007 using a global 3-D chemical transport model (GEOS-Chem). I evaluate the model by comparing its results with observations in the United States and all over the globe. Using the best estimate of annual mean BrC concentrations, I examine the global direct radiative effect (DRE) of BrC and its effect on photochemistry.

## 4.1. BrC emission estimate methods

I discuss the method to estimate primary and secondary sources of BrC, and provide explicit global BrC emissions. The primary and secondary sources include biomass burning and biofuel use, and the production from aromatic VOCs, respectively. Estimated global emissions are used as input for GEOS-Chem below to explicitly simulate spatial and temporal distributions of BrC concentrations.

### 4.1.1. Primary sources

Biomass burning is the largest source of CA aerosols globally (Bond et al., 2004). OC is primarily emitted during the smoldering (low-temperature burning) phase of combustion (Chakrabarty et al., 2010; Chakrabarty et al., 2014; Schnaiter et al., 2006), whereas BC is preferentially emitted from the flaming (high-temperature burning) phase. Therefore, BrC is also emitted largely during the smoldering phase of burning. Here, I use the relationship between the burning efficiency and the observed aerosol light absorption to estimate the BrC emission from biomass burning.

Previous studies have suggested MCE defined in Eq. (4.1) below to provide quantitative information of burning efficiencies that can be categorized into flaming versus smoldering combustion (Kaufman et al., 1998; Ward et al., 1992; Ward and Hao, 1991). For example, Reid et al.

(2005) used a MCE value of 0.9 to differentiate between flaming (MCE > 0.9) and smoldering combustion (MCE < 0.9).

$$\mathrm{MCE} = \frac{\Delta C_{CO_2}}{\Delta C_{CO_2} + \Delta C_{CO}}, \quad (4.1)$$

where ΔC is the change in species concentration in fire off-gas relative to clean air [molecules $m^{-3}$].

McMeeking (2008) further found a linear relationship between the observed attenuation Ångström exponents and the calculated MCE values from a number of biomass burning samples, as shown in Eq. (4.2).

$$\mathring{A} = -17.34 \times \mathrm{MCE} + 18.20 \quad (4.2)$$

where Å is the AAE of biomass burning samples.

The coefficient of determination (R2) of the relationship in Eq. (4.2) is 0.39, so the associated uncertainty appears to be significant. However, the negative relationship between AAE and MCE in Eq. (4.2) is robust as identified by previous studies (Saleh et al., 2014; Kirchstetter and Thatcher, 2012). For example, absorption of aerosols from biomass burning can be contributed by either BC or BrC, or both (Moise et al., 2015). As discussed above, the absorption of carbonaceous aerosols is mainly caused by BC at high MCE conditions (>0.9); in contrast, the BC/CA ratio is almost zero at low MCE conditions (<0.8) (McMeeking, 2008). Using Eq. (4.2), I calculate AAE values of 0.86 and 4.3 at MCE values of 1.0 and 0.8, respectively, and each calculated AAE is in good agreement with the observed BC (0.86) and BrC AAE (5.0) from biomass burning samples measured by Kirchstetter and

Thatcher (2012). Saleh et al. (2015) also showed that the BC to OC ratio (proportional to MCE) has negative relationship with AAE.

In addition, I can obtain the BrC/BC absorption ratio using AAE. In Chapter 4.1.2, I present a detailed description of the method for estimating the relationship between the BrC/BC absorption ratio and AAE. Here I assume external mixing, and this assumption can cause uncertainties when particles are internally mixed (such as coating effect). For uncertainty analysis, I calculate three BrC/BC absorption cases as shown in Figure 4.1, which shows the estimated BrC/BC absorption ratio at 550 nm as a function of MCE. Different lines indicate different AAEs of BC and BrC according to the Table 4.1 of Kirchstetter and Thatcher (2012). They calculated BC AAE and BrC AAE using 115 wood smoke samples. For the calculation of BrC AAE, BC AAE had to be decided, and they assumed three different BC AAEs (0.86, 1.00, 1.15) based on their smoke samples and previous studies. Resulting BrC AAEs were 5.00, 5.48, and 6.19. I conduct three simulations according to the Figure 1, as described later in this Chapter. For high MCE conditions (>0.95), the BrC contribution to the CA absorption is negligible, whereas it becomes significant for low MCE conditions (<0.85).

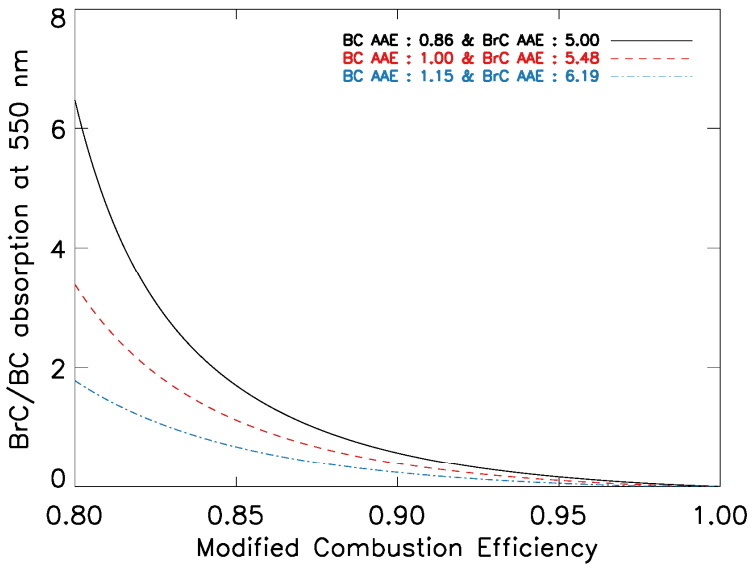


Figure 4.1. Estimated absorption ratios of BrC to BC at 550 nm as a function of MCE. I assume that the CA absorption is only contributed by BC and BrC absorption.

I calculate the MCE of biomass burning based on the FINN (Wiedinmyer et al., 2011) with vegetation dependent emission factors of $CO_2$ and CO using Eq. (4.3) as follows:

$$MCE = \frac{\Delta C_{CO_2}}{\Delta C_{CO_2} + \Delta C_{CO}} = \frac{EF_{CO_2}/MW_{CO_2}}{EF_{CO_2}/MW_{CO_2} + EF_{CO}/MW_{CO}} \quad (4.3)$$

where EF is the emission factor [g-species kg-dry matter$^{-1}$] and MW is the molecular weight [g-species mole$^{-1}$]. .

Finally, mass absorption efficiency (MAE), which is used for converting light absorption to mass concentration, is needed to obtain the BrC/BC mass ratio from the BrC/BC absorption ratio. For the fresh BC MAE at 550 nm, I use the value of 7.5 $m^2$ $g^{-1}$ recommended by Bond and Bergstrom (2006) (Nakayama et al., 2013; Park et al., 2010). For BrC, a large range of MAE values (0.09-4.1 $m^2$ $g^{-1}$ at 550 ± 30 nm) has been reported (Alexander et al., 2008; Cheng et al., 2011; Chung et al., 2012; Clarke et al., 2007; Favez et al., 2009; Hecobian et al., 2010; Hoffer et al., 2006; Kirchstetter et al., 2004; McMeeking, 2008; Yang et al., 2009). The highest MAE (3.6-4.1 $m^2$ $g^{-1}$ at 550 nm) was observed by Alexander et al. (2008), who used transmission electron microscopy to identify the optical properties of individual BrC particles in the atmosphere. Generally, low MAEs were reported when analyzing water soluble organic carbon (WSOC) from water extracts (Cheng et al., 2011; Hecobian et al., 2010; Srinivas and Sarin, 2014), indicating that WSOC may include both BrC and colorless OC. Intermediate MAEs mostly came from optical measurements (Chung et al.,

2012; Favez et al., 2009; Yang et al., 2009). For the primary BrC MAE, I use 1.0 $m^2$ $g^{-1}$ at 550 nm based on McMeeking (2008), who conducted a number of MAE measurements of biomass burning samples (~30 unique fuels tested in ~230 burns) using both filter-based and optical-based methods. In brief, I use the MAE values of 7.5 $m^2$ $g^{-1}$ and 1.0 $m^2$ $g^{-1}$ at 550 nm for BC and primary BrC, respectively. But at a shorter wavelength, higher MAE value was used for primary BrC (e.g., 5.3 $m^2$ $g^{-1}$ at 365 nm as discussed in Chapter 4.3).

Using the results in Figure 4.1 with Eq. (4.3), I calculate the EF (mass) ratio of BrC to OC as summarized in Table 4.1. The EF ratio of BrC to OC differs for each vegetation type and assumed BC AAE (0.86-1.15). Among different vegetation types, cropland burning shows the highest BrC to OC mass ratio, driven by the low MCE and the highest ratio of BC to OC EF. Because I calculate the BrC to OC EF ratio by multiplying the BrC to BC EF ratio by the BC to OC ratio, the high BC to OC ratio can lead to a high BrC to OC ratio. Although Table 4.1 shows the highest BrC/OC ratio from cropland burning, its contribution to the global BrC emission is small because the OC emission from the cropland is the lowest (Wiedinmyer et al., 2011). Instead, the tropical forest burning is the highest, and the resulting total BrC emission from biomass burning is 3.9 ± 1.7 TgC $yr^{-1}$, which contributes about 17 ± 7% of total OC emission from biomass burning (22.7 TgC $yr^{-1}$) (Wiedinmyer et al., 2011).

My method of estimating BrC emissions from biofuel use is similar to

that of estimating emissions from biomass burning. I estimate BrC/OC ratio using the MCE and BC to OC ratio in the same way as the biomass burning estimates. The only difference is that the biofuel emission of each sector is not known (the biomass burning emission is known for each vegetation type). Therefore, I first estimate OC biofuel emissions from each biofuel category with the information given by previous studies (Bond et al., 2007; Bond et al., 2004; Fernandes et al., 2007). Because there is no clear evidence that BrC is emitted by dung, charcoal, and the industrial sector, here I consider only fuelwood and agricultural residue as BrC sources. Fuelwood burning is the largest contributor to biofuel BrC emission. The estimate of BrC/OC mass ratio is 0.271 - 0.663 from biofuel use. Overall results are summarized in Table 4.2. Note that base year of Table 4.2 is 2000 because previous studies reported their values based on 2000. I scale up the emission for 2007 as described in Chapter 4.2.2. Resulting BrC emission from biofuel use is 3.0 ± 1.3 TgC $yr^{-1}$, which is comparable to BrC emission from biomass burning.

Table 4.1. Emission factors (EFs) and calculated parameters used for primary BrC emission estimates. Biomass burning emission is classified for six vegetation types based on the FINN inventory. Here BrC/OC is the mass ratio of BrC to OC emitted from biomass burning and biofuel use.

| **Source Type** | **$CO_2$ EF [g $kg^{-1}$]** | **CO EF [g $kg^{-1}$]** | **MCE** | **OC EF [g $kg^{-1}$]** | **BC EF [g $kg^{-1}$]** | **BrC/OC** | | |
|---|---|---|---|---|---|---|---|---|
| Biomass burning | | | | | | case1 | case2 | case3 |
| Boreal Forest | 1514 | 118 | 0.891 | 7.8 | 0.20 | 0.135 | 0.093 | 0.057 |
| Cropland | 1537 | 111 | 0.898 | 3.3 | 0.69 | 0.946 | 0.652 | 0.400 |
| Savanna/Grassland | 1692 | 59 | 0.948 | 2.6 | 0.37 | 0.189 | 0.123 | 0.067 |
| Temperate Forest | 1630 | 102 | 0.910 | 9.2 | 0.56 | 0.211 | 0.145 | 0.088 |
| Tropical Forest | 1643 | 92 | 0.919 | 4.7 | 0.52 | 0.312 | 0.213 | 0.128 |
| Woody Savannah/Shrubland | 1716 | 68 | 0.941 | 6.6 | 0.50 | 0.123 | 0.081 | 0.046 |
| Biofuel[1)] | | | | | | 0.663 | 0.452 | 0.271 |

1) Detailed information is given in Table 4.2

Table 4.2. Global biofuel consumption estimates, EFs of OC, and OC biofuel emission estimates for each biofuel category. Base year is 2000.

| | | Fuelwood | Crop Residues | Dung | Charcoal | Industrial | Total |
|---|---|---|---|---|---|---|---|
| Biofuel Consumption[1)] [Tg] | | 1351 | 495 | 75 | 39 | 498 | 2457 |
| EF [g/kg][2)] | | 2.97[3)] | 3.3 | 1.8 | 1.3 | 0.91[3)] | 2.6 |
| OC emission [Gg] | | 4010.3 | 1633.5 | 135 | 50.7 | 453.6 | 6281[4)] |
| BrC/OC | case1 | 0.653 | 0.946 | 0.000 | 0.000 | 0.000 | |
| | case2 | 0.442 | 0.652 | 0.000 | 0.000 | 0.000 | |
| | case3 | 0.261 | 0.400 | 0.000 | 0.000 | 0.000 | |

1) From Fernandes et al. (2007)
2) From Bond et al. (2004)
3) Global mean value is estimated from Bond et al. (2004)
4) From GEOS-Chem biofuel OC inventory (carbon_200909) by Bond et al. (2007)

### 4.1.2. Relationship between BrC/BC absorption ratio and AAE

Here I describe a procedure for obtaining the relationship between the BrC/BC absorption ratio and AAE. Assuming no internal mixing and dust influence, total absorption at a certain wavelength (λ) can be expressed as:

$$\alpha_{\lambda,CA} = \alpha_{\lambda,BrC} + \alpha_{\lambda,BC} \quad (4.4)$$

Rewriting Eq. (4.4) using AAE:

$$\alpha_{\lambda_0,CA}\left(\frac{\lambda}{\lambda_0}\right)^{-A_{CA}^{O}} = \alpha_{\lambda_0,BrC}\left(\frac{\lambda}{\lambda_0}\right)^{-A_{BrC}^{O}} + \alpha_{\lambda_0,BC}\left(\frac{\lambda}{\lambda_0}\right)^{-A_{BC}^{O}} \quad (4.5)$$

Dividing each side of Eq. (4.5) by $\alpha_{\lambda_0,BC}$:

$$(1+F)\left(\frac{\lambda}{\lambda_0}\right)^{-A_{CA}^{O}} = F\left(\frac{\lambda}{\lambda_0}\right)^{-A_{BrC}^{O}} + \left(\frac{\lambda}{\lambda_0}\right)^{-A_{BC}^{O}} \quad (4.6)$$

where F is the BrC/BC absorption ratio at $\lambda_0$.

Eq. (4.6) can be solved analytically, and the procedure is described in Chapter 4.1.3. I do not use the analytical relationship because it uses only three wavelengths for the calculations. The Ångström relationship is based on empirical fitting. AAE varies in different wavelength regions, even if I use the same samples. For example, Chung et al. (2012) showed that CA AAE is about 1.2 when the first four wavelengths (370, 470, 520, 590 nm) are used while the CA AAE is 1.35 with the last four wavelengths (590, 660,

880, 950 nm). This discrepancy is much increased in the case of BrC AAE. Liu et al. (2014) showed that BrC AAE varies by approximately 20%, depending on wavelength pairs. Furthermore, if I calculate AAE of BrC using the MAE of Kirchstetter et al. (2004), AAE of BrC in all wavelengths (from 350 to 650 nm, 7 values) is fitted to 5.9 with a $R^2$ of 0.96. However, the AAE of BrC using just two wavelengths is 4.1 for the 350-440 nm and 8.0 for the 550-600 nm, respectively.

Therefore, I calculate the relationship between MCE and F by regression using multiple wavelengths: [300, 350, 400, 450, 500, 550, 600, 650, 700, 750, 800, 850, 900 nm]. If I rewrite Eq. (3.6) for the regression form,

$$\overset{\circ}{A}_{CA} \log(\lambda) + C = -\log\left[ F\left(\frac{\lambda}{\lambda_0}\right)^{-\overset{\circ}{A}_{BrC}} + \left(\frac{\lambda}{\lambda_0}\right)^{-\overset{\circ}{A}_{BC}} \right] \tag{3.7}$$

where the residual term C is

$$C = \overset{\circ}{A}_{CA} \log(\lambda_0) - \log(1+F) \tag{3.8}$$

The left side of Eq. (3.7) has the shape of Ax+B. Therefore, by linear regression analysis, I can obtain $\mathring{A}_{CA}$ (the slope of the regression) as varying F on the right side. For example, when I calculate linear regression for F=4.0, $R^2$ is 0.99 and Angstrom exponent of CA is 4.44. Y-intercept of the numerical fitting is -29.81, which is consistent with Y-intercept (-29.64) from Eq. (3.8). The difference between two Y-intercept values are always within 1%, which shows the numerical fitting with Eq. (3.8) satisfies both

the slope (A) and the intercept (B) at the same time within 1% error. I choose an $Å_{BrC}$ values of {5.0, 5.48, 6.19} and an $Å_{BC}$ values of {0.86, 1.00, 1.15}, following Kirchstetter and Thatcher (2012), who estimated mean $Å_{BrC}$ using several wood samples (87 samples) over the 360 to 700 nm spectrum range. I assign a $\lambda_0$ value of 550 nm. The coefficient of determination ($R^2$) is greater than 0.98 in all the regression analyses. The calculated relationship between MCE and F is plotted in Figure 4.1. As expected, emissions of BrC are increased when MCE is decreased.

## 4.1.3. Analytical derivation of Eq. (4.6)

Here I describe the procedure to obtain the analytical relationship between MCE and F. First, substituting $\lambda_1$ and $\lambda_2$ in Eq. (4.6),

$$(1+\mathrm{F})\left(\frac{\lambda_1}{\lambda_0}\right)^{-\overset{o}{A}_{CA}} = \mathrm{F}\left(\frac{\lambda_1}{\lambda_0}\right)^{-\overset{o}{A}_{BrC}} + \left(\frac{\lambda_1}{\lambda_0}\right)^{-\overset{o}{A}_{BC}} \tag{4.9}$$

$$(1+\mathrm{F})\left(\frac{\lambda_2}{\lambda_0}\right)^{-\overset{o}{A}_{CA}} = \mathrm{F}\left(\frac{\lambda_2}{\lambda_0}\right)^{-\overset{o}{A}_{BrC}} + \left(\frac{\lambda_2}{\lambda_0}\right)^{-\overset{o}{A}_{BC}} \tag{4.10}$$

Assuming AAE between $\lambda_0$ and $\lambda_1$ is equal to AAE between $\lambda_0$ and $\lambda_2$, divide Eq. (4.9) by Eq. (4.10), and rearrange terms:

$$\left(\frac{\lambda_1}{\lambda_2}\right)^{-\overset{o}{A}_{CA}} = \frac{F\left(\frac{\lambda_1}{\lambda_0}\right)^{-\overset{o}{A}_{BrC}} + \left(\frac{\lambda_1}{\lambda_0}\right)^{-\overset{o}{A}_{BC}}}{F\left(\frac{\lambda_2}{\lambda_0}\right)^{-\overset{o}{A}_{BrC}} + \left(\frac{\lambda_2}{\lambda_0}\right)^{-\overset{o}{A}_{BC}}} \tag{4.11}$$

Taking the logarithm of both sides:

$$\overset{o}{A}_{CA} = -\log\left(\frac{F\left(\frac{\lambda_1}{\lambda_0}\right)^{-\overset{o}{A}_{BrC}} + \left(\frac{\lambda_1}{\lambda_0}\right)^{-\overset{o}{A}_{BC}}}{F\left(\frac{\lambda_2}{\lambda_0}\right)^{-\overset{o}{A}_{BrC}} + \left(\frac{\lambda_2}{\lambda_0}\right)^{-\overset{o}{A}_{BC}}}\right) / \log\left(\frac{\lambda_1}{\lambda_2}\right) \tag{4.12}$$

Substituting Eq. (4.2) into Eq. (4.12) gives:

$$\mathrm{MCE} = \left[ 18.2 + \log \left( \frac{F\left(\frac{\lambda_1}{\lambda_0}\right)^{-\mathring{A}_{BrC}} + \left(\frac{\lambda_1}{\lambda_0}\right)^{-\mathring{A}_{BC}}}{F\left(\frac{\lambda_2}{\lambda_0}\right)^{-\mathring{A}_{BrC}} + \left(\frac{\lambda_2}{\lambda_0}\right)^{-\mathring{A}_{BC}}} \right) / \log\left(\frac{\lambda_1}{\lambda_2}\right) \right] / 17.34 \qquad (4.13)$$

After assigning $\mathring{A}_{BrC}$, $\mathring{A}_{BC}$, and the corresponding three wavelengths ($\lambda_0$, $\lambda_1$ and $\lambda_2$) in Eq. (4.13), I obtain the relationship between MCE and F analytically.

### 4.1.4. Secondary source

I consider SOC as a source of BrC in the model based on the observed optical characteristic of SOC, depending on its chemical formation, as follows: 1) anthropogenic (aromatic) SOCs tend to absorb solar radiation more efficiently than biogenic SOCs (Jacobson, 1999; Nakayama et al., 2010; Zhong and Jang, 2011; Zhong et al., 2012); 2) the solar absorption efficiency increases as SOCs undergo atmospheric aging processes (Bones et al., 2010; Lambe et al., 2013; Laskin et al., 2015; Laskin et al., 2010; Updyke et al., 2012); 3) SOCs formed in inorganic seeds have a darker color than others (Jaoui et al., 2008; Nakayama et al., 2013; Zhong and Jang, 2011; Zhong et al., 2012); moreover, SOCs become darker when they undergo aging in the presence of nitrogen-containing inorganic gases and aerosols (Bones et al., 2010; Laskin et al., 2010; Liu et al., 2012).

Among those factors, the first two are more important than the last. For example, the absorbance of aged biogenic SOCs produced in inorganic seeds is much lower than that of fresh anthropogenic SOCs under no-seed conditions (Zhong and Jang, 2011). Furthermore, Lambe et al. (2013) suggested that the effect of NOx on SOC light absorption is small under typical ranges of VOC/NOx. Therefore, here I consider the first two factors for BrC simulations in the model. I assume anthropogenic (aromatic) SOCs with high atmospheric aging as BrC in the model. Atmospheric aging is calculated using the VBS approach with six bins in the model (Jo et al.,

2013), where SOC concentrations of the first two bins are considered as BrC. However, I note that some brown SOCs can be bleached when they undergo photodissociation (Zhong and Jang, 2011; Sareen et al., 2013). Furthermore, browning reactions can be accelerated by cloud and fog processing of aerosols (Moise et al., 2015), which are not considered in this study. More detailed treatments of the chemical aging of BrC are needed in future BrC models.

BrC from anthropogenic SOC has different optical properties (i.e, MAE, imaginary refractive index) compared with BrC from wood burning. Therefore, I apply different optical parameters for the model evaluation (Chapter 4.3) such as 5.3 $m^2$ $g^{-1}$ (McMeeking, 2008) for primary BrC and 1.5 $m^2$ $g^{-1}$ (Nakayama et al., 2010) for secondary BrC at 365 nm (note that the MAE of primary BrC at 550 nm is 1.0 $m^2$ $g^{-1}$ as discussed in Chapter 4.1.1). The estimated annual source of secondary BrC is 5.7 TgC $yr^{-1}$, which contributes 45% of total BrC sources.

## 4.2. Model evaluation

I conduct a model evaluation using the observed light absorption of WSOC measured by Hecobian et al. (2010) and Zhang et al. (2011; 2013) in the United States. The model evaluation allows us not only to validate simulated BrC concentrations but also to examine each source contribution to BrC in the United States. I also use the global SSA observations from the AERONET to evaluate the effect of including BrC on light absorption by aerosols over the globe.

### 4.2.1. United States

Prior to evaluating BrC simulations, I first focus on BC and OC aerosols in the model to examine the general model performance in simulating carbonaceous aerosol concentrations in the United States. I use BC and OC observations from the Interagency Monitoring of Protected Visual Environments (IMPROVE) network for 2007 (Malm et al., 1994). Most sites were situated in rural regions, measuring background concentrations of BC and OC. The data were available every three days; more than 20,000 samples were used for our comparison. For comparison with the model results, I computed the observed monthly mean concentrations of BC and OC averaged on the 2°×2.5° model grid.

Figure 2 shows scatterplot comparisons of the observed and simulated monthly mean BC and OC concentrations in the United States. The model

slightly underestimates both BC and OC over the United States, consistent

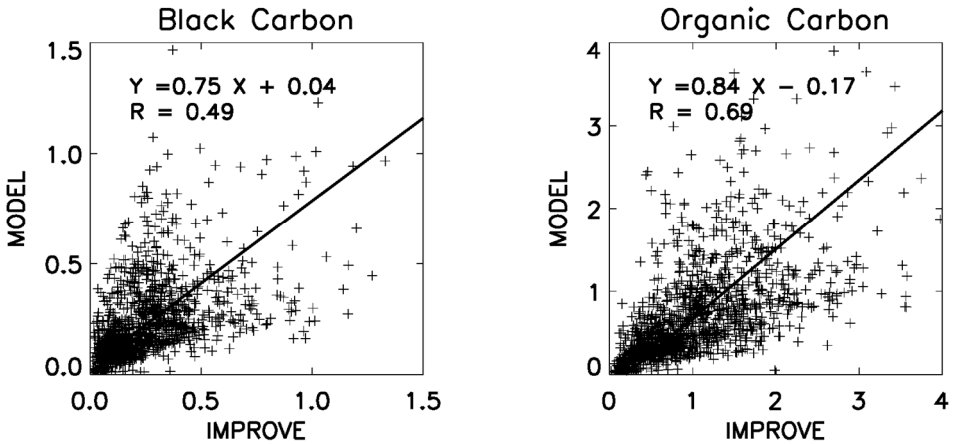


Figure 4.2. Scatterplot of simulated versus observed BC concentrations (left) and OC concentrations (right). Unit is μgC $m^{-3}$. Values are monthly means for 2007. Regression equations and correlations are shown inset. Regression is computed with reduced major axis (RMA) method.

with similar comparisons in Huang et al. (2013). I calculate the annual mean concentrations of the model using the simulated values of model grid boxes corresponding to the IMPROVE network sites. The simulated annual mean BC concentration is 0.22 μgC $m^{-3}$, which is 12% lower than the observed mean value (0.25 μgC $m^{-3}$). However, the bias in the model is larger for OC by 30% (1.16 and 0.81 μgC $m^{-3}$ for observed and simulated OC concentrations, respectively), which is additionally due to the underestimation of SOC in the model (Jo et al., 2013). This low bias for SOC can be reflected in the simulated BrC concentrations, which is discussed later in this Chapter

I use the light absorption observations of WSOC measured using a UV-Vis spectrophotometer and Long-Path absorption Cell by Hecobian et al. (2010), and compare them with the light absorption by BrC in the model. Absorption coefficients of WSOC at 365 nm were measured at 15 sites in the southeastern United States in 2007. Among them, eight sites are in urban areas, and the others are in rural regions. Detailed descriptions of the measurements are available in Hecobian et al. (2010).

Because light absorption observations are measured only for water soluble fractions of OC, and do not include water insoluble components, I separate BrC in the model into water soluble and water insoluble components. The model divides OC (or BrC) into hydrophilic and hydrophobic components. For the comparison, I do not use the simulated

hydrophilic fraction, but instead use an observed WSOC/OC ratio because the assumed division of hydrophobic and hydrophilic fractions of OC and their conversion can be applicable in a global sense, but in a regional sense, it may cause a significant discrepancy. For example, the observed water soluble fraction of the total OC is generally low (on the order of 25%) in the Los Angeles basin (Zhang et al., 2013), on the other hand, the model simulates a high water-soluble fraction of the total OC (63-74%) in this region. For this reason, I decide to use the observed WSOC/OC ratio for the evaluations. In the southeastern United States, the observed WSOC/OC ratio is about 0.58 (Weber et al., 2007; Zhang et al., 2013), which is also used to estimate the water soluble BrC concentrations from the total BrC concentrations in the model.

Because the model simulates a mass concentration of BrC, a conversion from the mass concentration to light absorption is carried out by multiplying MAE values. For BrC from wood burning, I use the MAE value of 5.3 $m^2$ $g^{-1}$ at 365 nm measured by McMeeking (2008) in order to retain the consistency between the emission estimates and the evaluation. For BrC from SOC, I select the MAE of 1.5 $m^2$ $g^{-1}$ at 365 nm calculated by Nakayama et al. (2010).

Figure 4.3 shows monthly mean simulated and observed light absorption coefficients of BrC at 365 nm averaged over all sites in the southeastern United States for 2007. Black circles and colored bars indicate the observed and simulated BrC absorption at 365 nm, respectively, and

different colors in the bar show contributions from different sources. Each panel represents different model simulations with each case for AAE selections as shown in

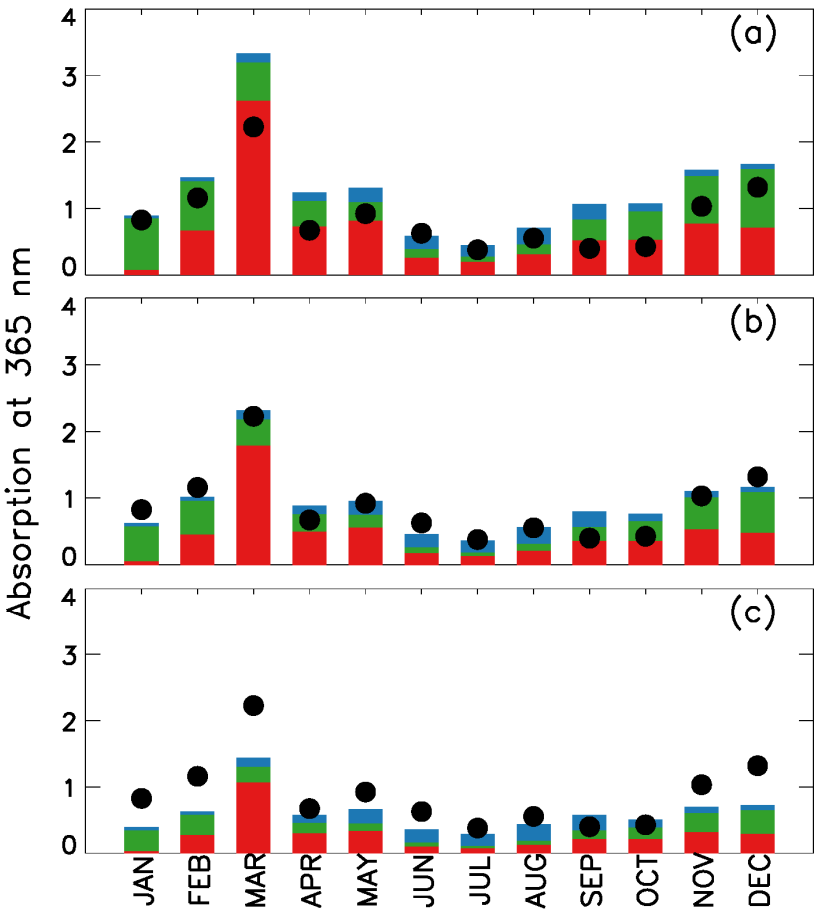


Figure 4.3. Simulated versus observed monthly mean light absorption at 365 nm by water soluble BrC over the southeastern US in 2007. Unit is $Mm^{-1}$. Black circles denote observations, and bar graphs indicate model results for each source: biomass burning (red), biofuel (green), and SOA (blue). Each panel shows the comparisons with different emission estimate cases – (a) case 1, (b) case 2, and (c) case 3.

Figure 4.1 and Table 4.1.

In winter months (November through March), the observed light absorptions were generally high and reached a peak in March. These high absorptions were highly correlated with levoglucosan, which is a marker for biomass burning (Hecobian et al., 2010). During the summer, the observed light absorptions decreased substantially.

The model generally captures the observed seasonal variation with high absorption in the winter, having a peak in March and low absorption in the summer (R of 0.93). On an annual mean basis, I find that the model is too high by 46% for case 1, and is too low by -31% for case 3, relative to the observations, respectively. The model for case 2 is in the best agreement with the observations (4%) on an annual mean basis.

The BrC source contribution in the model is similar to the observed source contribution. Hecobian et al. (2010) showed that biomass burning was the main contributor for the winter season, whereas the SOC contribution increased during the summer season. The simulated seasonal variation is consistent with the observation, as shown in Figure 4.3. The annual mass contribution of SOC to BrC is 38% (in case 2), which is in good agreement with the observed contribution of 32% (Hecobian et al., 2010). Based on the results in Figure 4.3, the model for the case 2 yields

best estimates of BrC emissions.

In addition to the observation by Hecobian et al. (2010), I use the light absorption observations by Zhang et al. (2011; 2013). Measurements were carried out in Atlanta, GA (33.778427N, 84.396181W), Pasadena, CA (34.140528N, 118.122455W), and Riverside, CA (33.97185N, 117.32266W) for a month or less. As discussed above, I apply the observed WSOC/OC ratio to the model BrC concentrations: 26% for the Los Angeles basin (Pasadena and Riverside) (Zhang et al., 2013) and 58% for Atlanta (Weber et al., 2007; Zhang et al., 2013).

Figure 4.4 shows the daily mean observed and simulated light absorption coefficients from the best model (case 2) for Atlanta, Pasadena, and Riverside for 2010. The upper panel shows the comparison of the observed versus simulated light absorption for Atlanta. The highest observed daily absorption occurred on August 24, but the model fails to reproduce it. Furthermore, the model generally overestimates the observed absorption by 44%, and the large discrepancies mainly occur in September. This large discrepancy in September is similar to the result shown in Figure 4.3(b) for 2007.

The middle and lower panels show the comparisons at the Los Angeles basin sites in May and June. The observed mean light absorptions at these sites (0.81 and 0.98 $Mm^{-1}$ for Pasadena and Riverside, respectively) are higher than the observed mean light absorption (0.56 $Mm^{-1}$) for Atlanta. However, the model underestimates the observations by 38% (Pasadena)

and 48% (Riverside). Zhang et al. (2013) showed that the main sources of BrC at these sites were SOC from anthropogenic emissions. The model also shows a high contribution (85%) of the secondary source to the total BrC mass concentrations, but the magnitudes are generally lower than the observations,

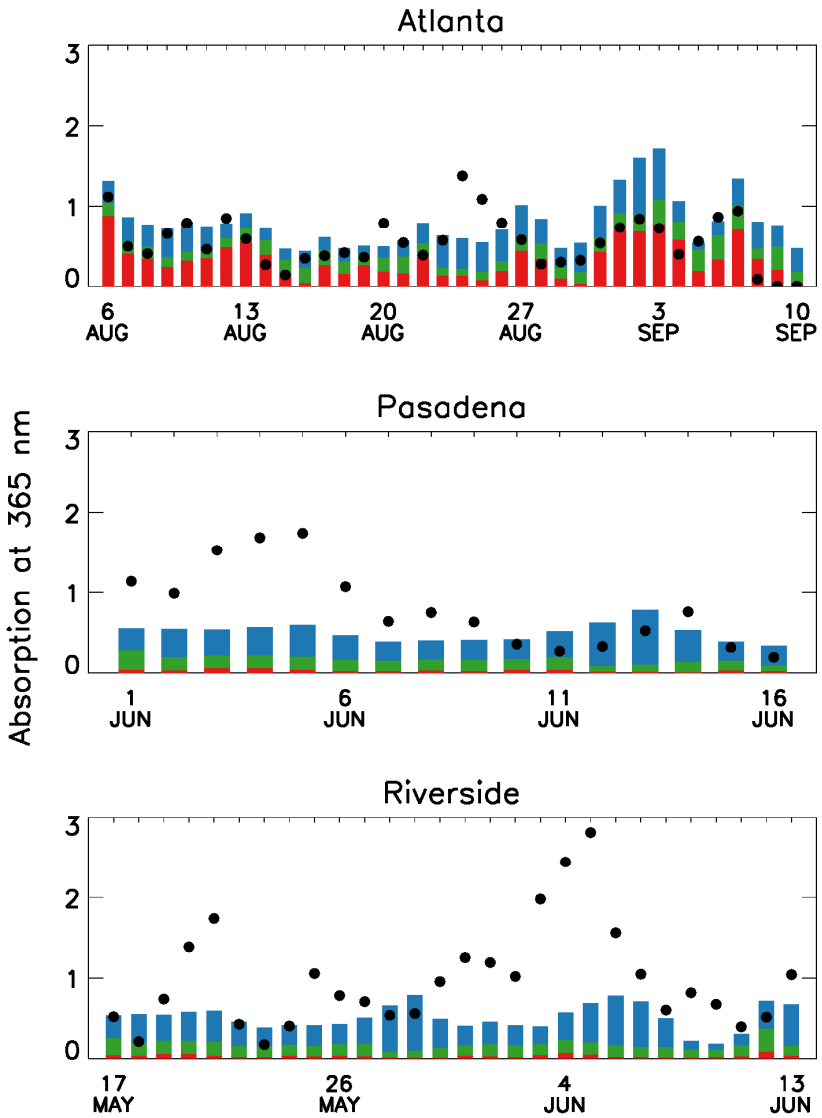


Figure 4.4. Simulated versus observed daily mean light absorption at 365 nm by water soluble BrC over the US in 2010. Unit is $Mm^{-1}$. Black circles denote observations and bar graphs indicate model results for each source – biomass burning (red), biofuel (green), and SOA (blue).

and this low bias is likely related to underestimation of the simulated SOC concentrations using the 1-D VBS (Jo et al., 2013).

I find from the model evaluation over the United States that the model generally captures the observed mean absorption and its seasonal variability in the region where primary sources are dominant. On the other hand, the model underestimates the observed mean absorption in the region with the dominant secondary sources. The low bias is partly explained by the SOC underestimation in the model. However, the underestimations of BrC from SOC (38-48%) are higher than those of SOC (18%), indicating the importance of additional secondary BrC sources that I did not include in the model.

A MAE value for secondary BrC could be another possible reason for the bias in the model. Although chamber studies suggested weak absorbing characteristics of BrC from SOC (Nakayama et al., 2010; Nakayama et al., 2013; Zhong and Jang, 2011), some field observations speculated the existence of strongly-absorbing BrC from SOC (Alexander et al., 2008; Chung et al., 2012). For example, applying the MAE value of 3.5 $m^2$ $g^{-1}$ at 365 nm (a half of the MAE at 365 nm from Alexander et al. (2008)) for secondary BrC yields a similar mean absorption value to the observation over LA basin. Extensive observations of optical characteristics of BrC depending on frthe formation mechanisms would be needed to reduce the associated uncertainties and to improve the model.

### 4.2.2. Evaluation against global AERONET observations

No global observation of BrC is available yet. Here I use the observed SSA at AERONET sites to evaluate the model by focusing on the effect of BrC on the simulated aerosol absorption. I also use observed AOD to evaluate the model capability to simulate aerosol mass concentrations.

For comparisons of AOD and SSA between the model and observations, I use FlexAOD (http://pumpkin.aquila.infn.it/flexaod/), which calculates AOD and SSA using simulated aerosol mass concentrations from GEOS-Chem with the Mie algorithm (Mischenko et al., 2002; Curci et al., 2015).

For optical properties of BrC, I use imaginary refractive indices of BrC from McMeeking (2008) for wood burning sources, and from Nakayama et al. (2010) for SOC sources. Detailed description of the values used in AOD and SSA calculation are provided in Chapter 4.5, where I discuss the DRE of BrC.

Figure 4.5 shows comparisons of monthly mean simulated versus observed AOD at 500 nm and SSA at 440 nm. I find that the model captures the observed AOD quite well with a regression slope of 0.86 and a R of 0.88. However, the model tends to overestimate the observed SSA, implying that the simulated aerosol concentrations appear to have too large a fraction of scattering aerosols. I find that the inclusion of BrC in the model reduces the high bias of simulated SSA by 33% and 23% (lower left and lower right panel of Figure 4.5), indicating a considerable contribution of BrC to

aerosol absorption. Although the statistics suggest a greater improvement with the case 1 in terms of the bias, simulated SSA values at sites in Africa with high BrC concentrations, are too low apart from the regression line (discrepancy > 0.1). This result also supports our selection of the case 2 as the best model for BrC emission estimates.

Despite a decrease of simulated SSA with BrC, the model is still too high relative to the observations. The overestimation might be partly caused by the underestimation of BC emissions from biomass burning (Bond et al., 2013). This is also supported by the fact that the discrepancy gets larger for biomass burning regions, where a difference between the model and AERONET SSA is 40% higher than that in regions with high anthropogenic emissions. Emission factors of BC used in this study are 0.2-0.69 g $kg^{-1}$ (Wiedinmyer et al., 2011), which are lower than the value of 1 g kg-1 used by Chin et al. (2009), who found no significant bias in their model compared with the AERONET SSA. Lin et al. (2014) also reported a small bias in their model compared with AERONET SSA using 4.7 Tg $yr^{-1}$ of global annual biomass burning BC emissions, which is about two times higher than 2.2 Tg $yr^{-1}$ of this study.

In addition to the biomass burning emission of BC, the anthropogenic emission of BC could also contribute to the simulated SSA bias. Cohen and Wang (2014) showed that a global top-down emission of BC is twice as large as the bottom-up estimates of BC based on the Kalman Filter approach. They suggested that BC emissions in East Asia, Southeast Asia, and Eastern

Europe are significantly underestimated in current bottom-up emission inventories.

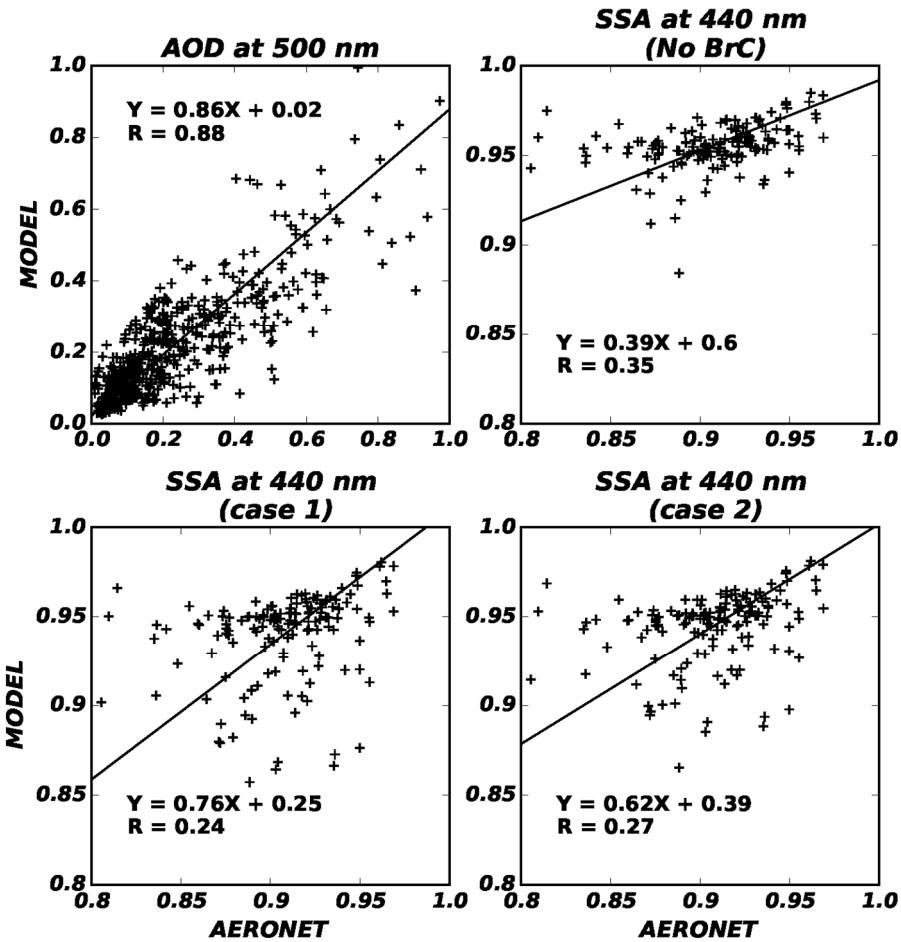


Figure 4.5. Scatterplots of simulated versus observed AOD at 500 nm (upper left), SSA at 440 nm without BrC (upper right), SSA at 440 nm with BrC of case 1 (lower left), and SSA at 440 nm with BrC of case 2 (lower right) for 2007. Reduced major axis regression is shown along with the regression equation and R. Each point indicates monthly averaged AOD or SSA when the number of observation is greater than 10 days.

This issue is critically important, and possibly has an important implication for climate. However, an investigation of BC emissions for the SSA discrepancy above is beyond the scope of our work, and will be conducted in future studies.

Light absorption enhancement of aged BC could also be one of the reasons for the SSA overestimation in the model. Here I use the same optical parameters for all BC in the model. However, Bond et al. (2006) suggested that the absorption of aged BC is about 1.5 times greater than that of fresh BC. BC aging occurs as it is mixed internally with other aerosols. If I assume hydrophilic BC as aged BC in the model and its absorption enhancement by a factor of 1.5 relative to hydrophobic BC, the high bias of simulated SSA is additionally reduced by about 20% (not shown).

I further compare the model against AERONET AAE as shown in Figure 4.6. I find that the model overestimates the observed AAE after including BrC, in part, because the model underestimates BC emissions as discussed above. However, the simulated AAE will be decreased if I increase BC emissions as suggested by the top-down estimate (Cohen and Wang, 2014). For example, for regions (North America, Central America, South America, Southeast Asia, and Australia) where the difference between the BC emission and the top-down estimate is within a factor of 2, I find that the model with BrC shows a better agreement with the observed AAE

(Figure 4.7) and with the observed SSA (Figure 4.8).

Considering all these uncertainties, the evaluation above indicates that the model for the case 2 results in the best estimates of simulated BrC concentrations, which will be used for examining BrC effects on climate and photochemistry, below and other two cases are considered as upper and lower limits of the estimates.

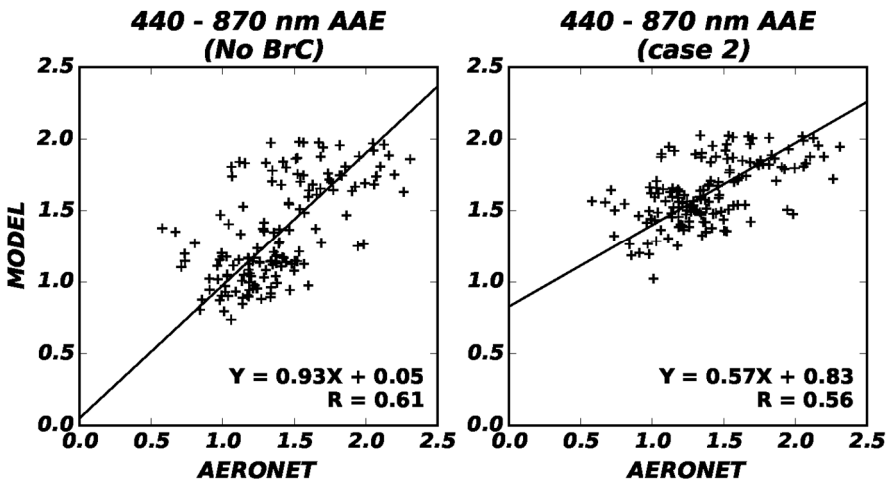


Figure 4.6. Scatterplots of simulated versus AERONET 440 – 870 nm AAE for the without BrC (left) and with BrC of case 2 (right).

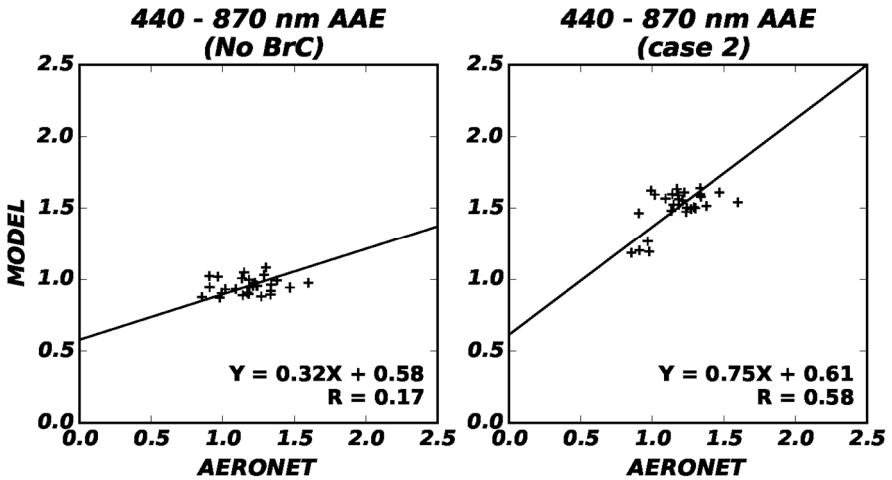


Figure 4.7. Same as Figure 4.6 but for the regions where the BC emission ratios between our model and top-down estimates from Cohen and Wang (2014) are less than 2.

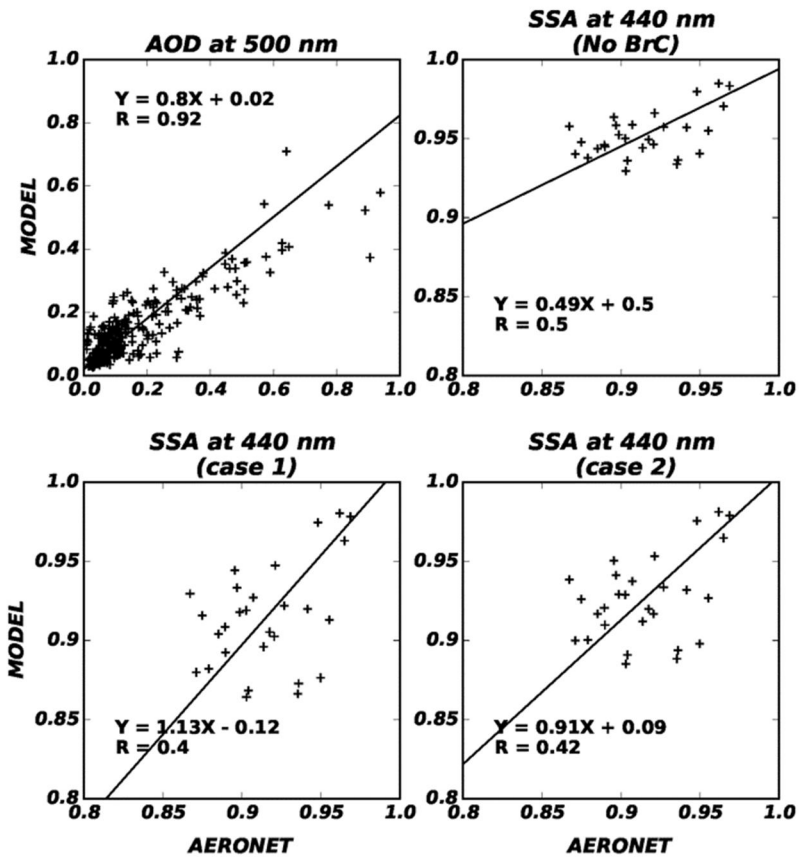


Figure 4.8. Same as Figure 4.5 but for the regions where the BC emission ratios between our model and top-down estimates from Cohen and Wang (2014) are less than 2.

## 4.3. Global budgets

### 4.3.1. Annual surface concentration

Figure 4.9 shows our best estimates of annual mean concentrations of BrC and each source contribution in surface air for 2007. Values are high in regions where biomass burning (Southeast Asia and South America) and biofuel (East Asia and Northeast India) sources are dominant. These primary sources account for 77% of BrC concentrations in surface air. On the other hand, secondary sources are relatively minor in the surface, but their contribution increases in the free troposphere, as discussed in Chapter 4.4.2.

Figure 4.10 shows BrC to BC and OC ratios in surface air in the model. The BrC to BC ratio is highest over the eastern North Pacific and the North Atlantic. This high ratio over the ocean reflects a secondary chemical production, which contributes to BrC but not to BC. Over the continents, the ratio is generally higher in heavy biomass burning regions (South America and Africa) than in industrialized regions (East Asia, Europe, and the eastern United States) because more BrC than BC is emitted from biomass burning.

Similarly, the BrC to OC ratio is also high over the oceans because of secondary BrC, the concentrations of which increase with atmospheric aging. Over the continents, the ratio is smaller reflecting relatively fresh emissions of OC from anthropogenic sources that do not directly contribute to BrC. I find that the BrC to OC ratio is relatively high in regions with large biofuel use (North India and Central Asia). Although China is one of the largest

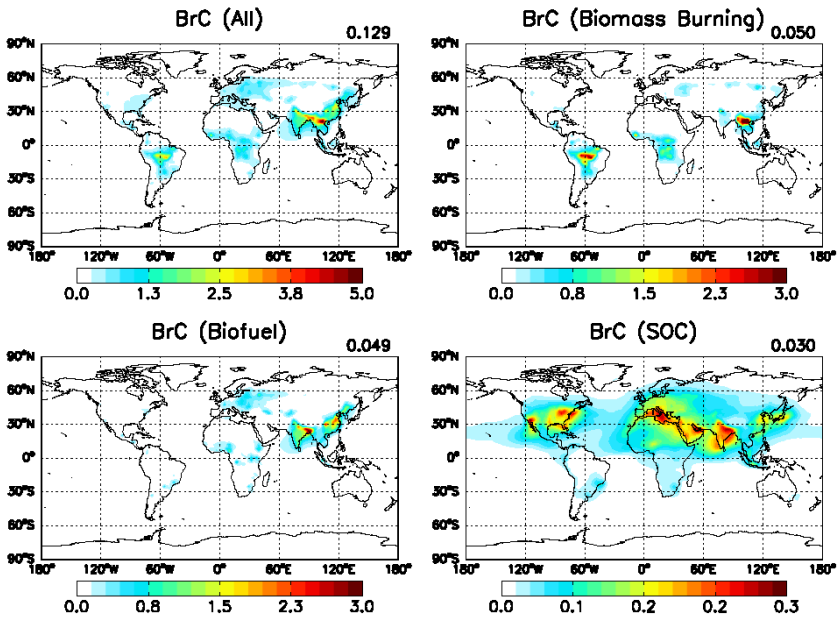


Figure 4.9. Annual surface map of total BrC (top left) and BrC from three source categories: biomass burning (top right), biofuel (bottom left), and SOC (bottom right). Mean values are presented in the upper right corner of each panel. Unit is μgC $m^{-3}$.

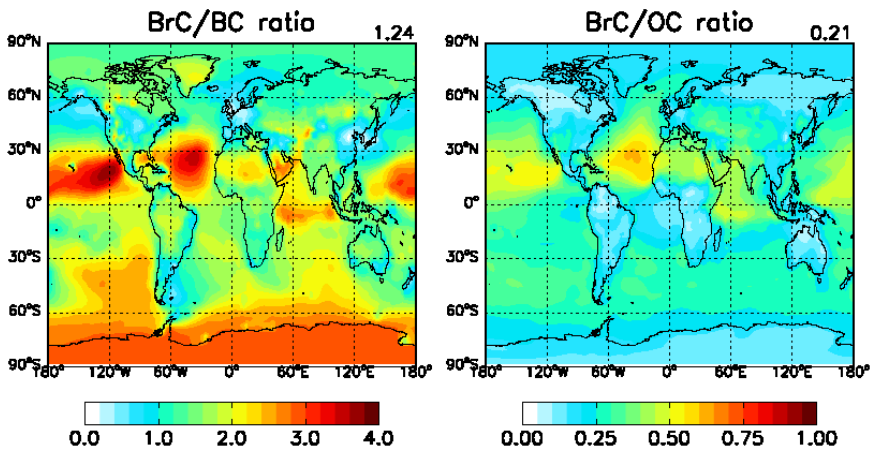


Figure 4.10. Annual mean ratios of BrC to BC (left) and OC (right) in surface air. Global mean values are presented in the upper right corner of each panel.

emission source regions for BrC (Figure 4.9), both BrC to BC and BrC to OC ratios are relatively low because of high concentrations of BC and OC. Our global mean BrC to BC and BrC to OC ratios at the surface are 1.24 and 0.21, respectively and are lower than the ratio (3.4 of BrC to BC ratio and 0.43 of BrC to OC ratio in terms of burden) of Feng et al. (2013), but higher than the ratio (1.0 of BrC to BC ratio) used in Park et al. (2010).

### 4.3.2. Tropospheric budget of BrC

Table 4.3 summarizes our best estimates of the global tropospheric budgets of BrC, along with BC and OC. The global BrC source is 12.5 ± 3.0 TgC $yr^{-1}$, which accounts for 27% of OC sources. Although the biofuel emission (6.5 TgC $yr^{-1}$) is three times lower than the biomass burning emission (22.7 TgC $yr^{-1}$) for OC, the biofuel emission (3.0 ± 1.3 TgC $yr^{-1}$) becomes significant for BrC, contributing about 43% of primary sources. The secondary source of BrC is 5.7 TgC $yr^{-1}$, and is comparable to the primary sources (6.8 ± 3.0 TgC $yr^{-1}$).

Wet deposition is the main removal process for BrC, and accounts for 86 % of total removal processes. The remaining loss is due to dry deposition. The contribution of wet deposition to total deposition of BrC is similar to

that of OC (82%), because I treat BrC scavenging similarly to that of OC. Because secondary BrC is produced all over the troposphere (not only at the surface) and is hydrophilic, most secondary BrC is removed by wet deposition processes (92%).

The global burden of BrC shows the highest contribution from secondary BrC (50 %) compared to primary contributions from biomass burning (30 %) and biofuel (20 %). This result is opposite to the source contributions in surface air shown in Figure 4.9. The contribution of secondary BrC to the atmospheric burden is twice as high as the contribution of secondary BrC to the surface concentration (23%), reflecting a relatively large production of BrC in the free troposphere as well as limited export of primary BrC from the surface to the free troposphere.

Our BrC lifetime is 5.8 days, which is lower than that of OC (7.9 days) because of different contributions of the secondary sources for BrC and OC. The latter species includes a larger fraction of secondary species (52%), the lifetime of which is usually longer than that of POC especially for not aged biogenic SOC (Jo et al., 2013). No significant difference between the lifetimes of BrC and BC exists because BrC, which is more hydrophilic than BC, is more prone to wet scavenging than BC.

Table 4.3. Global tropospheric budgets of BrC compared to those of OC and BC. Uncertainties are indicated in the parentheses.

| Unit : [GgC] | BrC | | | OC | BC | BrC/OC | BrC/BC |
|---|---|---|---|---|---|---|---|
| Sources | Biomass burning | 3857 | (±1689) | | | 0.27 (±0.06) | 1.83 (±0.43) |
| | Biofuel | 2965 | (±1281) | | | | |
| | Anthropogenic SOC | 5690 | | | | | |
| | Total | 12512 | (±2970) | 46929 | 6847 | | |
| Wet Deposition | Biomass burning | 3169 | (±1389) | | | 0.28 (±0.07) | 1.97 (±0.45) |
| | Biofuel | 2358 | (±1018) | | | | |
| | Anthropogenic SOC | 5244 | | | | | |
| | Total | 10771 | (±2407) | 38681 | 5458 | | |
| Dry Deposition | Biomass burning | 688 | (±301) | | | 0.21 (±0.07) | 1.25 (±0.41) |
| | Biofuel | 607 | (±263) | | | | |
| | Anthropogenic SOC | 445 | | | | | |
| | Total | 1740 | (±564) | 8272 | 1397 | | |
| Burden | Biomass burning | 59 | (±26) | | | 0.19 (±0.05) | 1.84 (±0.41) |
| | Biofuel | 40 | (±18) | | | | |
| | Anthropogenic SOC | 98 | | 1021 | 107 | | |

| | | | | | |
|---|---|---|---|---|---|
| | Total | 197 | (±44) | | |
| Lifetime [days] | Biomass burning | 5.6 | (±0.0) | | |
| | Biofuel | 5.0 | (±0.0) | | |
| | Anthropogenic SOC | 6.3 | | | |
| | Total | 5.8 | (±0.1) | 7.9 | 5.7 |

## 4.4. Direct radiative effect of BrC

I use imaginary refractive indices of BrC as a function of wavelength for radiative transfer calculations to account for the wavelength dependency of the BrC absorption. Imaginary refractive indices in the literature have a wide range of values, even from the same sources, such as wood burning (Chakrabarty et al., 2010; Kirchstetter et al., 2004; McMeeking, 2008). In order to maintain the consistency with BrC emission estimates from primary sources, I use the imaginary refractive indices reported by McMeeking (2008), which are 0.18, 0.14, and 0.10 at 370, 405, and 532 nm, respectively. The values are interpolated with the AAE at every 50 nm wavelength interval for the radiative transfer calculations. For secondary BrC, values

from Nakayama et al. (2010) are used with 0.047 and 0.007 at 355 and 532 nm, respectively, based on the measurements for SOC from toluene.

I calculate AOD, SSA, and asymmetry parameter using FlexAOD, which is described in Chapter 4.3.2. Note that I calculate DRE rather than DRF. DRE is the instantaneous radiative impact of all atmospheric particles on the Earth's energy balance, and DRF is the change in DRE from pre-industrial to present-day (Heald et al., 2014). I use the Rapid Radiative Transfer Model for GCMs (RRTMG) (Iacono et al., 2008) for DRE calculations. Wavelengths used for the calculation are 300, 304, 393, 533, 702, 1010, 1270, 1462, 1784, 2046, 2325, 2788, 3462, and 8021 nm. MERRA reanalysis data are used for albedo and other meteorological variables.

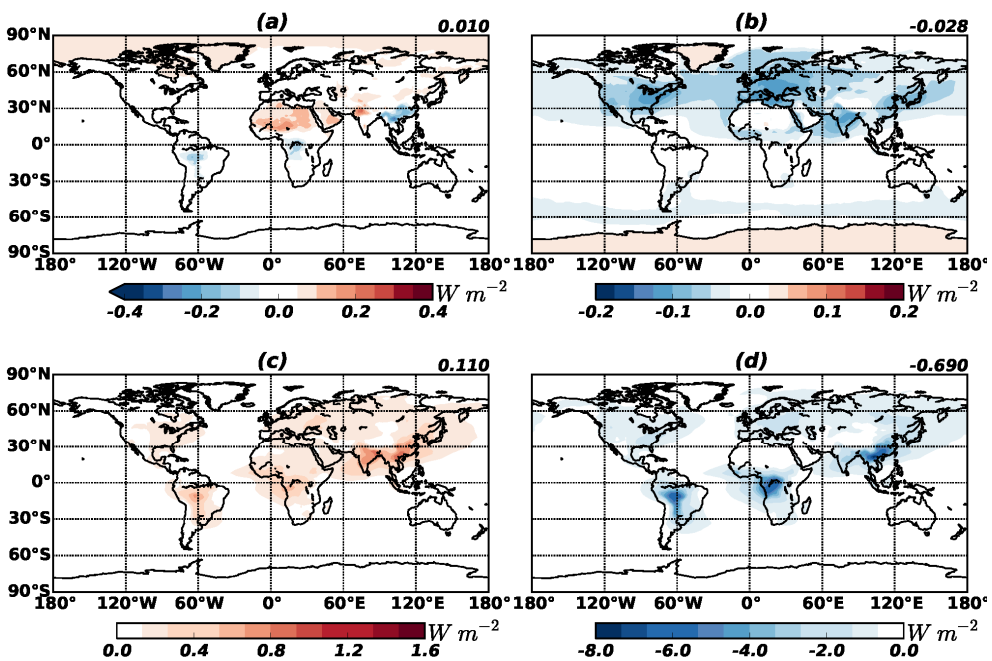


Figure 4.11. DRE of BrC at the top of the atmosphere. Upper panels are for

radiative effect of BrC from primary sources (a) and from secondary sources (b). The DRE increase of OC owing to the absorption of BrC is shown in (c) (i.e. the DRE of OC with absorbing BrC minus the DRE of OC including BrC as scattering OC, which is typically assumed in previous studies). Radiative effect of total OC (BrC is assumed to be scattering OC) is represented in (d). The 70°S–70°N averages are shown in the upper right corner of each panel.

Figures 4.11(a) and 4.11(b) show the clear sky DRE values of primary and secondary BrC concentrations. Because the imaginary refractive indices of BrC are between those of strongly absorbing BC and scattering OC, the global mean DRE of BrC is close to zero, as shown in (a) and (b).

Although the DRE of BrC at the top of the atmosphere is nearly zero, the increased DRE of OC after considering BrC absorption (usually considered as scattering OC) is 0.11 W $m^{-2}$, as shown in Figure 4.11(c). The DRE of OC without BrC absorption is -0.69 W $m^{-2}$ (Figure 4.11(d)), and this value is increased to -0.58 W $m^{-2}$ after considering BrC absorption. Consequently, the cooling effect of OC is reduced by 16%.

Despite the negligible effect of BrC on DRE or DRF, its significance manifests for OC DRF estimates, which have been conducted based on the assumption of scattering OC. For example, AeroCom phase II simulations calculated -0.03 W $m^{-2}$ as the global mean DRF of POC from fossil fuel and biofuel, and -0.06 W $m^{-2}$ for that of SOC (Myhre et al., 2013). Because the biofuel emission is about twice as large as the fossil fuel emission (Bond et al., 2007), and one-half of OC from biofuel is BrC, one-third of the POC from fossil fuel and biofuel is BrC. Therefore, one-third of DRF (-0.01 W $m^{-2}$) of POC in AeroCom is related to BrC, whose DRF is close to zero. For SOC, because the pre-industrial biogenic SOC concentration is similar to present-day conditions, almost all DRF of SOC is from anthropogenic SOC. Based on previous SOC studies (Henze et al., 2008; Jo et al., 2013; Murphy and Pandis, 2010), approximately one-third of anthropogenic SOC is highly aged, and can thus be assumed to be BrC in this simple estimation. As a result, one-third of DRF (-0.02 W $m^{-2}$) of SOC in AeroCom is related to BrC. The total DRF of BrC that was assumed to be scattering OC in the AeroCom study is -0.03 W $m^{-2}$. Because DRF of BrC is almost negligible, the negative DRF of OC (-0.09 W $m^{-2}$) in AeroCom could likely be overestimated by 50%. I think, however, the warming effect of BrC on the negative DRF or DRE of OC would be a low-end value because our best model likely underestimates BrC concentrations especially from the secondary source.

## 4.5. Effect on ozone photochemistry

BrC absorption, particularly at UV wavelengths, has an important implication for ozone photochemistry. Here I examine the effect of BrC absorption on photochemistry by updating photolysis rate calculations in GEOS-Chem following Martin et al. (2003). Table 4.4 shows the calculated extinction efficiency and SSA of important aerosols at 0.4 μm, which affect UV extinction, and thus photolysis rate calculations, in the model. Values of OC, BC, and inorganic aerosols are from GEOS-Chem, in which I update aerosol optical properties by adding those of BrC. I include optical

properties of primary and secondary BrC separately because they differ substantially. For example, SSA values of primary BrC are smaller than those of secondary BrC, and thus have a greater impact on UV radiation. Compared with other aerosols, SSA values of BrC are generally lower than those of OC and inorganic aerosols, but higher than those of BC.

Martin et al. (2003) showed that the effects of aerosols on photolysis rates increased CO by 5-15 ppbv in the remote Northern Hemisphere (annual mean concentrations less than 140 ppbv). This increase resulted in an improved model agreement with observations, but there was a still gap between the model and the observations. In our simulation with BrC, CO concentration is further increased by 0.2-1.9 ppbv in remote Northern Hemisphere regions (annual mean concentrations less than 140 ppbv in the model). On the other hand, OH concentrations are decreased by 0-10% in the boundary layer over the Northern Hemisphere (maximum decreases occur in regions with high BrC concentrations, shown in Figure 4.9). The change of OH owing to BrC is about one-third of the OH change according to the overall aerosol effects from Martin et al. (2003). Therefore, the inclusion of BrC significantly affects tropospheric chemistry, especially for regions with heavy biomass burning and biofuel emissions.

Finally, I quantify the effects of BrC on global $NO_2$ photolysis rates and ozone concentrations at the surface. Figure 4.12 shows changes in annual $NO_2$ photolysis rates and $O_3$ concentrations in surface air owing to BrC absorption. Although BrC absorption is included, there are no

significant changes (less than 1%) of the global mean $NO_2$ photolysis rate and $O_3$ concentration in surface air. However, the effect of BrC appears to be important for regions with high BrC concentrations. I find a maximum decrease of the annual mean $NO_2$ photolysis rate by 8% in surface air over Asia where the resulting reduction of $O_3$ concentration is up to -2 ppbv (6% of annual mean surface $O_3$ concentration). I also find that the BrC effect has a strong seasonal variation such that it is maximized in the spring when surface $O_3$ concentration is decreased up to -13% in Asia because of high BrC concentration (55 μgC $m^{-3}$). This maximum $O_3$ decrease by BrC (-13%) is similar to the $O_3$ decrease (15%) by fire aerosols in Jiang et al. (2012).

Table 4.4. Extinction efficiencies and SSAs of selected aerosols at 0.4 μm used for calculating photolysis rates in GEOS-Chem. SNA indicates inorganic salt comprised of sulfate, nitrate and ammonium aerosols.

| 0.4 μm | RH | BrC (Primary) | BrC (Secondary) | OC | BC | SNA |
|---|---|---|---|---|---|---|
| Extinction Efficiency | 0% | 1.4644 | 1.2922 | 1.3933 | 0.6229 | 1.2147 |
| | 50% | 1.6995 | 1.5645 | 1.4967 | 0.6229 | 1.6566 |
| | 70% | 1.7873 | 1.6781 | 1.5815 | 0.6229 | 1.8440 |
| | 90% | 1.8386 | 1.7474 | 1.8485 | 0.4607 | 2.2568 |
| | 99% | 2.2696 | 2.4390 | 2.5870 | 0.4181 | 2.9655 |
| Single Scattering Albedo | 0% | 0.5621 | 0.8683 | 0.9735 | 0.1935 | 1.0000 |
| | 50% | 0.5474 | 0.8584 | 0.9841 | 0.1935 | 1.0000 |
| | 70% | 0.5422 | 0.8540 | 0.9873 | 0.1935 | 1.0000 |
| | 90% | 0.5342 | 0.8480 | 0.9927 | 0.3004 | 1.0000 |
| | 99% | 0.5412 | 0.8372 | 0.9977 | 0.5233 | 1.0000 |

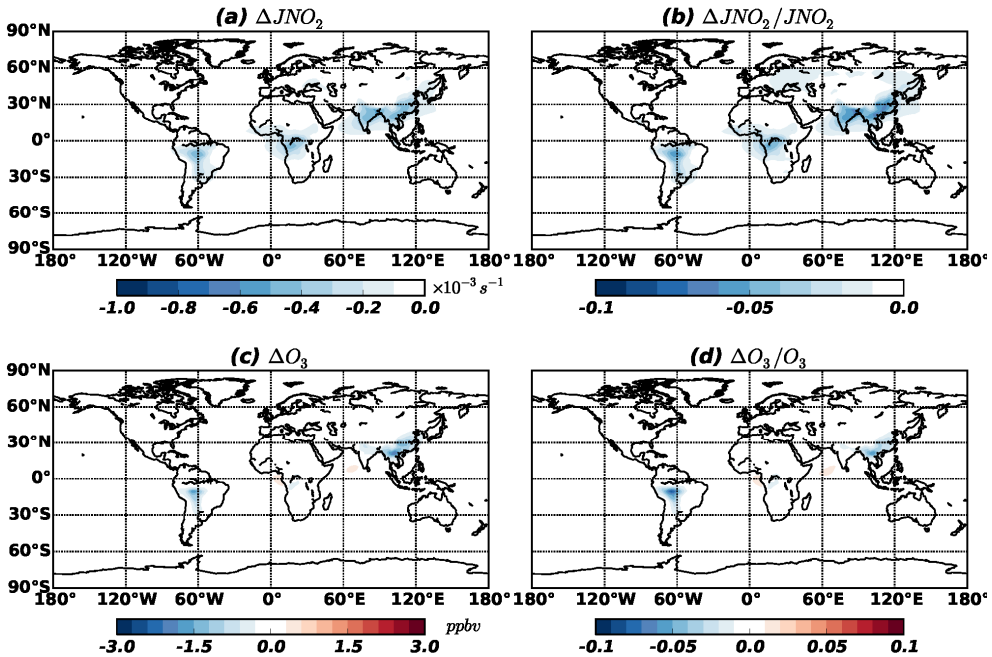


Figure 4.12. Changes in annual $NO_2$ photolysis rate (a,b) and $O_3$ concentration (c,d) at the surface due to BrC absorption.

## 4.6. Summary

OC has been considered to be a scattering aerosol, but emerging evidence has shown that some OC can efficiently absorb solar radiation. This absorbing OC is called BrC. With increasing recognition of its importance, especially for solar absorption at UV and short visible wavelengths, quantification of its spatial and temporal distribution is much needed for the study of climate and air quality issues. Here I conducted an explicit global BrC simulation for the full year of 2007 using a global 3-D chemical transport model (GEOS-Chem), and examined its implication for climate and O3 photochemistry.

I first estimated primary BrC emissions from biomass burning and biofuel use based on the relationship betIen AAE and MCE. The estimates of primary BrC emissions are 3.9 ± 1.7 and 3.0 ± 1.3 TgC $yr^{-1}$ from biomass burning and biofuel use, respectively. The secondary BrC source is estimated to be 5.7 TgC $yr^{-1}$ from the aromatic oxidation.

With explicit BrC emissions, a coupled oxidant-aerosol simulation was conducted for 2007 to obtain the spatial and temporal distributions of BrC concentrations. I first evaluated the model by comparing the simulated versus observed BrC absorption in the United States and found that the model successfully reproduced the observed seasonal variation of light absorption by WSOC in the southeastern United States, whereas the model significantly underestimated secondary BrC over the Los Angeles basin.

Our budget analysis showed that BrC from primary sources are dominant (77%) in surface air, but BrC from secondary sources becomes important with increasing altitudes. For example, BrC from secondary sources accounts for the 50% of the tropospheric BrC burden, which is higher than its 23% contribution to surface BrC concentrations. Our global mean value of the BrC to BC ratio is 1.83 for the whole atmosphere, and 1.24 for the surface, which significantly differs from the values used in previous studies.

Using the best results, I estimated the DRE of BrC to be close to zero at the top of the atmosphere because the imaginary refractive indices of BrC are in the midpoint between those of BC and OC. Despite a negligible

contribution to DRE, the inclusion of BrC absorption in the model offsets the negative radiative effect of OC by 0.11 W $m^{-2}$ (16%).

Finally, I included BrC absorption in photolysis rate calculations in the model. I found that the $NO_2$ photolysis rate is decreased up to 8%, especially for Asia, where BrC concentration is high. Resulting annual surface $O_3$ concentrations are decreased up to -2 ppbv (6%). This effect is more important in the spring, when a typical $O_3$ maximum occurs in Asia, where the effect of BrC decreases the surface $O_3$ concentration by up to -13%.

Many chemical transport models and air quality models have included the effect of aerosols on photolysis rate calculations, but have not considered the BrC effect. Based on our analysis, BrC absorption could have a significant direct impact on regional air quality by being involved in $O_3$ photochemical formation. Its significance, however, can be expanded to the globe by its effect on the atmospheric oxidation capacity, which has an indirect but important implication for global air quality and climate.

# Chapter 5. Key factors of single scattering albedo calculation

In this Chapter, I focus the analysis on four factors: physical parameters of BC, mixing state, dust size distributions, and the presence of BrC. I conduct global simulations for 2008 – 2010 using the GEOS-Chem model. First, I extensively evaluate simulated aerosol mass concentrations and aerosol optical properties by comparing the model with observations from global aerosol observation networks - global AMS dataset, the Surface

PARTiculate mAtter Network (SPARTAN), and AERONET for 2008 – 2010. Multiple sensitivity simulations are also carried out to examine the effects of individual factors on calculated SSA. Finally, using the simulation results, I estimate aerosol DRE and its sensitivity to assumed factors, which will confer us some insights in the climatic implication of current global climate models (GCMs).

Table 5.1. Global emissions used in this Chapter from 2008 to 2010.

| Emission type | Species | | | | | | |
|---|---|---|---|---|---|---|---|
| | $NO_x$ [TgN $yr^{-1}$] | $SO_x$ [TgS $yr^{-1}$] | $NH_3$ [TgN $yr^{-1}$] | BC [TgC $yr^{-1}$] | OC [TgC $yr^{-1}$] | Dust [Tg $yr^{-1}$] | Sea salt [Tg $yr^{-1}$] |
| Anthropognenic | 30.0 | 55.0 | 39.3[1)] | 5.5 | 12.1 | | |
| Biomass burning | 4.3 | 0.9 | 3.3 | 1.9 | 16.2 | | |
| Volanic | | 13.9 | | | | | |
| Oceanic DMS | | 16.8 | | | | | |
| Lightning | 7.1 | | | | | | |
| Soil | 10.2 | | | | | | |
| Aircraft | 0.8 | 0.1 | | | | | |
| Dust | | | | | | 1165.2 | |
| Sea salt | | | | | | | 3321.8 |
| Total | 52.5 | 86.7 | 42.6 | 7.4 | 28.3 | 1165.2 | 3321.8 |

1) Include agriculture sector

## 5.1. Aerosol optical property calculation

### 5.1.1. FlexAOD

I calculate AOD, SSA, and asymmetry parameter using FlexAOD, which is a GEOS-Chem post-processing tool for aerosol optical property calculations (Curci et al., 2015). FlexAOD uses the Mie theory (Mishchenko et al., 2002) with input data including size distributions, refractive indices, particle density, and hygroscopic growth factors of each aerosol species. Aerosol mixing state and its effects on AOD, SSA, and asymmetry parameter are also considered. I assume three different mixing states - external mixing, homogeneous internal mixing, and core-shell internal

mixing. Each aerosol is assumed to be formed by a single chemical species in case of the external mixing. The homogeneous internal mixing assumes all aerosols are well mixed, and the core-shell internal mixing assumes an insoluble well-mixed core is coated by a concentric well-mixed soluble shell. A detailed description of the aerosol optical property calculation with different mixing states can be found in Section 2 of Curci et al. (2015).

### 5.1.2. Input parameters for FlexAOD

Table 5.2 summarizes the input parameters used in the Mie calculation of FlexAOD. The values in Table 5.2 are the same as the input parameters used in online aerosol optical property and photolysis rate calculations in the standard GEOS-Chem v10.1. Input parameters in GEOS-Chem were initially from the Optical Properties of Aerosols and Clouds (OPAC) database (Hess et al., 1998) and Chin et al. (2002), which was described in Martin et al. (2003).

Here I briefly discuss significant updates after Martin et al. (2003). The log-normal distribution is assumed for aerosols except for soil dust,

which follows the Gamma distribution. Geometric standard deviations of inorganic aerosols, OA, and BC are reduced from 2.0 (OPAC) to 1.6 based on measurements from the optical particle counter instrument during the ICARTT 2004 field campaign (Drury et al., 2010). Inorganic aerosols follow the refractive index and hygroscopic growth factors (HGFs) of water-soluble component (WASO), which is changed from those of sulfate droplets (SUSO) in OPAC. HGFs of OA are updated to 1.35 at 95% RH based on the chamber and field observations by Jimenez et al. (2009). The geometric mean radius of BC is 0.020 μm, which is increased from 0.012 μm. The density of BC is increased to 1.8 g $cm^{-3}$ (Bond and Bergstrom, 2006) from 1.0 g $cm^{-3}$ by OPAC (Hess et al., 1998). These BC-related parameter changes lead to significant changes in aerosol absorption, which is discussed in the following Chapter.

Table 5.2. Input parameters used in the Mie calculation for FlexAOD. The log-normal distribution with geometric mean radius ($r_g$) and geometric standard deviation ($\sigma_g$) are assumed to aerosols except for dust, which follows the gamma distribution with gamma A and gamma B. Particle density ($\rho$), refractive index (RI), and hygroscopic growth factors (HGF) are also presented.

| | | | | Sea salt | | Dust | | | |
|---|---|---|---|---|---|---|---|---|---|
| | Inorganics | OA | BC | Accumulation | Coarse | Bin1 (0.1~1.0 μm) | Bin2 (1.0~1.8 μm) | Bin3 (1.8~3.0 μm) | Bin4 (3.0~6.0 μm) |
| $r_g$ (μm) | 0.0695[a] | 0.073[b] | 0.020[e] | 0.085[g] | 0.401[g] | | | | |
| $\sigma_g$ | 1.6[b] | 1.6[b] | 1.6[b] | 1.5[g] | 1.8[g] | | | | |
| Gamma | | | | | | | A = 0.9, B = 0.2 | | |
| $\rho$ (g cm$^{-3}$) | 1.7[c] | 1.8[a] | 1.8[f] | 2.2[a] | | 2.5 | 2.65 | 2.65 | 2.65 |
| RI at 550 nm | 1.53 - 0.006i[a] | 1.53 - 0.006i[a] | 1.74 - 0.44i[a] | 1.50 - $10^{-8}$i[a] | | | 1.558 - 0.0014i[h] | | |
| HGF at 50% | 1.34[a] | 1.14[d] | 1.0[c] | 1.81[a] | 1.81[a] | | 1.0 | | |
| HGF at 95% | 1.88[a] | 1.35[d] | 1.50[c] | 2.89[a] | 2.92[a] | | 1.0 | | |

a) OPAC (Hess et al., 1998)
b) Drury et al. (2010)
c) GOCART (Chin et al., 2002)
d) Jimenez et al. (2009)
e) http://wiki.seas.harvard.edu/geos-chem/index.php/Aerosol_optical_properties#Overview
f) Bond and Bergstrom (2006)
g) Jaegle et al. (2011)
h) Sinyuk et al. (2003)

### 5.1.3. Effects of size distribution and refractive index of BC on light absorption

As discussed in Chapter 1.3, BC particles are aggregated together (Alexander et al., 2008), which makes it difficult to choose the appropriate radius of BC for the Mie calculation (Koch et al., 2009). Here I examine the sensitivity of BC absorption with respect to the choice of geometric mean radius ($r_g$) and geometric standard deviation ($\sigma$) using the Mie theory. Using a BC column concentration of 0.25 mg $m^{-2}$, I calculate absorption AOD (AAOD) for 1 – 200 nm ($r_g$) and 1.2, 1.6, and 2.0 ($\sigma$) as shown in Figure 5.1(a). Values are generally within the reported ranges of global mean BC AAODs ($0.8 \times 10^{-3} – 3.5 \times 10^{-3}$) from AeroCom phase Ⅰ models, although I do not consider a hygroscopic growth. Red star and blue rectangle symbols indicate OPAC ($r_g$ = 12 nm and $\sigma$ = 2.0) and GEOS-Chem default size distributions ($r_g$ = 20 nm and $\sigma$ = 1.6). I find that the uses of these two size distributions lead to very similar AAODs (< 1% difference), resulting from the combined effects of increased $r_g$ and decreased $\sigma$.

Figure 5.1(b) represents calculated BC AAOD as a function of real and imaginary refractive index. BC AAOD increases as imaginary refractive index increases and real refractive index decreases. Red star and blue triangle indicate BC AAODs using refractive indices from OPAC (1.74 - 0.44i) and Bond and Bergstrom (2006) (1.95 - 0.79i), respectively. BC AAOD using the refractive index of 1.95 - 0.79i is 49% higher than that using the refractive index of 1.74 - 0.44i. A similar result was reported by

Stier et al. (2007), who also found that their AAOD using 1.95 - 0.79i was 52% higher than that using 1.74 - 0.44i in the ECHAM5-HAM model.

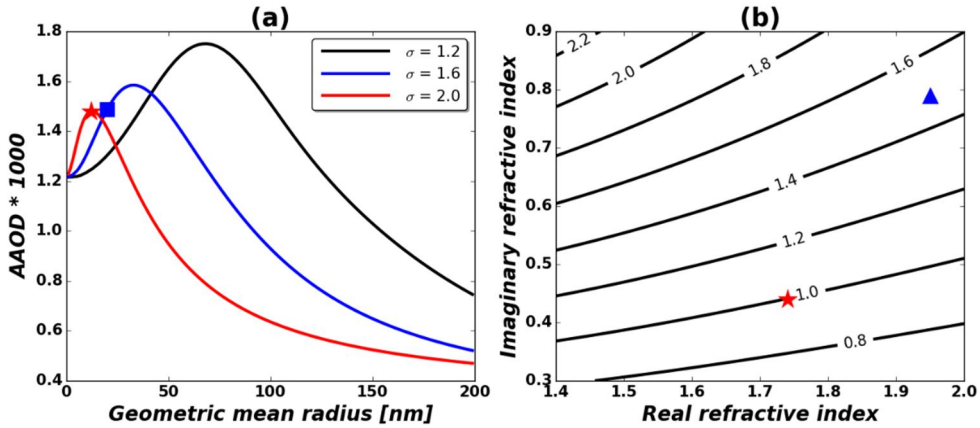


Figure 5.1. (a) Calculated BC AAOD at 550 nm (y-axis) as a function of geometric mean radius ($r_g$) [nm] (x-axis). Three different geometric standard deviations (σ) are assumed – 1.2 (black line), 1.6 (blue line), and 2.0 (red line). Red star and blue rectangle symbols indicate OPAC ($r_g$ = 12 nm and σ = 2.0) and GEOS-Chem default conditions ($r_g$ = 20 nm and σ = 1.6), respectively. Refractive index of 1.95 - 0.79i is used for this calculation. (b) Calculated BC AAOD (multiplied by 1000, contour line) as a function of real refractive index (x-axis) and imaginary refractive index (y-axis). Red star and blue triangle symbols represent BC AAODs using refractive index by OPAC (1.74 - 0.44i) and Bond and Bergstrom (2006) (1.95 - 0.79i), respectively. $r_g$ of 20 nm and σ of 1.6 are assumed in this calculation. For both plots, BC column concentration of 0.25 mg $m^{-2}$ and particle density of 1.8 g $cm^{-3}$ are used. Hygroscopic growth is not counted in this calculation.

### 5.1.4. FlexAOD simulations

Using aerosol mass concentrations from GEOS-Chem simulations above, I carry out a number of FlexAOD simulations by changing the input parameters of BC as shown in Table 5.3 to examine the sensitivity of calculated aerosol absorption to assumed input parameters. For example, the GEOS case indicates a FlexAOD simulation using GEOS-Chem default values as of v10-01. The OPAC database is used for the OP sensitivity case. Refractive index of 1.95 - 0.79i is used for BB, BBR, and BBHR cases with different geometric radiuses of BC. The geometric mean radius of 0.065 μm is adapted from Bond et al. (2013). I additionally assume the geometric mean radius of 0.1 μm, which seems to be higher than that used by previous studies (Bond et al., 2013; Wang et al., 2014) but still within the range of the AeroCom study (Koch et al., 2009).

After the sensitivity simulations in Table 5.3, I further consider different mixing states, effects of brown carbon, and observationally constrained dust size distributions. I add tag names for representing these factors. As discussed in Chapter 5.1.1, I consider three mixing states of external, homogeneous internal, and core-shell internal - "_E", "_H", and "_C" tag names are added to base case names in Table 5.3, respectively. If the sensitivity case includes BrC absorption, "_BR" tag name is added. I also implement in the model new dust size distributions suggested by Kok (2011) and Zhang et al. (2013). Kok (2011) suggested new dust size distributions based on the physics of the scale-invariant fragmentation of

brittle materials. Based on the dust size distribution by Kok (2011), Zhang et al. (2013) further developed the dust size distribution with constraints from in-situ measurements. "_DK" and "_DI" tag names are applied when I use dust size distributions by Kok (2011) and Zhang et al. (2013), respectively. For instance, "GEOS_BR_DI_H" means the model with GEOS-Chem default input parameters, brown carbon, dust size distribution by Zhang et al. (2013), and the homogeneous internal mixing assumption.

Table 5.3. Input parameters of BC for sensitivity simulation cases in this study.

| Case | Refractive index | Mean Radius [μm] | Sigma | Density [g $cm^{-3}$] |
|---|---|---|---|---|
| GEOS | 1.74 - 0.44i | 0.02 | 1.6 | 1.8 |
| OP | 1.74 - 0.44i | 0.0118 | 2.0 | 1.0 |
| BB | 1.95 - 0.79i | 0.02 | 1.6 | 1.8 |
| BBR | 1.95 - 0.79i | 0.065 | 1.6 | 1.8 |
| BBHR | 1.95 - 0.79i | 0.1 | 1.6 | 1.8 |

## 5.2. Model evaluation

### 5.2.1. Global aerosol mass concentration

I use the AMS dataset (Zhang et al., 2007) and the SPARTAN observations (Snider et al., 2015) to evaluate simulated mass concentrations of aerosols globally. Because the observations were available for multi years (AMS: 2000~2008, SPARTAN: 2013~2015), I focus the evaluation on observed monthly variation using the monthly mean value of the simulation averaged for 2008–2010. Year to year variability is not considered in this evaluation similar to previous studies (Jo et al., 2013; Spracklen et al., 2011; Yu, 2011).

Figure 5.2 shows point-to-point comparisons of the simulated monthly mean sulfate, nitrate, ammonium, and organic aerosol concentrations with the AMS network observations. Statistical parameters including the regressions slope, y-intercept (Y-ict), correlation coefficient (R), normalized mean bias (NMB), and root mean square error (RMSE) are presented in Table 5.4. I find that the model successfully reproduces observed inorganic aerosol concentrations with correlation coefficients of 0.62-0.78 and regression slopes of 0.69-0.84. Compared to Chapter 3.2.1, the model shows an improved performance in terms of statistics (e. g. RMSEs are decreased by 22-45%). These improvements are attributed to the different emission inventory used in this Chapter.

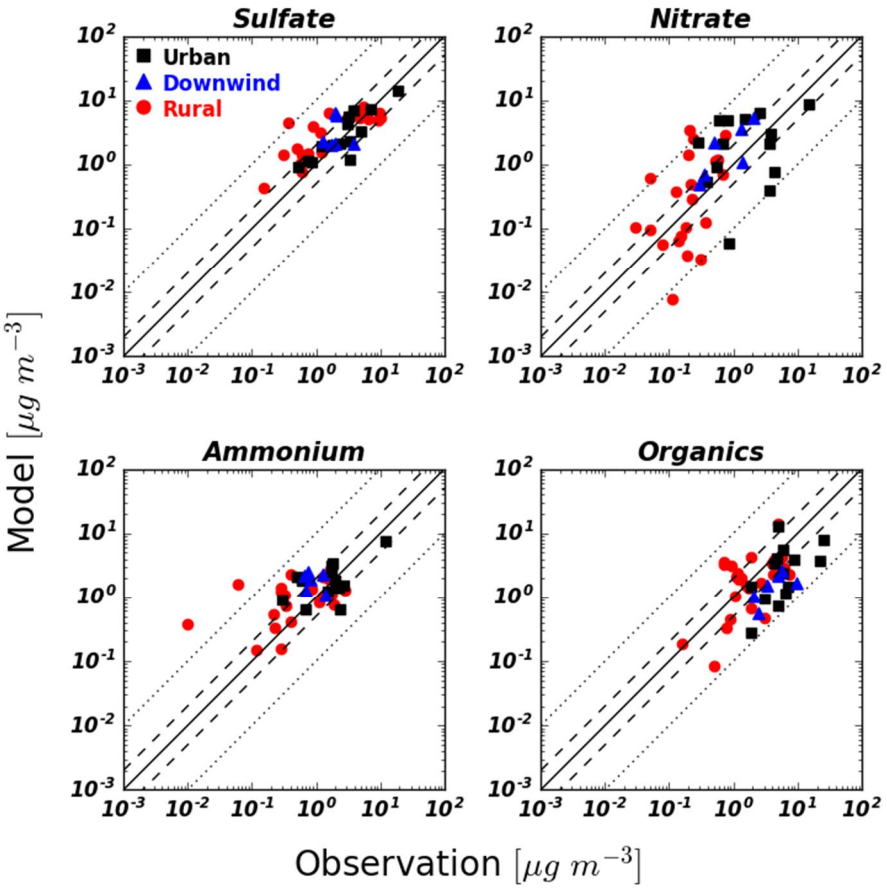


Figure 5.2. Point-to-point comparisons of the simulated sulfate, nitrate, ammonium, and organics to the AMS network observations. I multiply organic matter to organic carbon ratio of 2.1 to organics to account for the non-carbon mass. The 1:1 line (solid), 2:1 lines (dashed), 10:1 lines (dotted) are indicated.

In contrast to inorganic aerosols, the model shows a low correlation coefficient (0.36) and a high RMSE (4.77 μg $m^{-3}$) for OA. This result is consistent with the evaluation of OA against AMS in the previous literature (Jo et al., 2013; Yu, 2011). A low bias (-37%) in the model is mainly caused by poor SOA simulations, which still show a considerable gap from observations as pointed out by the recent AeroCom intercomparison study for OA (Tsigaridis et al., 2014).

Figure 5.3 shows scatter plots of BC, sulfate, nitrate, ammonium, dust, and $PM_{2.5}$ between SPARTAN observations and the model results. Statistical parameters are also shown in Table 5.4. I find that the model performance for inorganic aerosols is degraded, especially for nitrate aerosols. Different observation years are one of the reasons for the discrepancy between evaluations against the AMS (2000-2008) and the SPARTAN (2013-2015). There have been decreasing trends in $NO_x$ emissions and column concentrations over the United States and Europe during the past decade (Curier et al., 2014; Granier et al., 2011; Simon et al., 2014), and the United States and Europe are main regions for the AMS observation network (Zhang et al., 2007). Therefore, there is a possibility that these two different global observation networks (AMS and SPARTAN) represent different nitrate concentration levels. I find that the nitrate overestimation mainly occurs over the United States (7 of 19 points above 10:1 line in Figure 3) and South Asia (7 of 19 points above 10:1 line in Figure 3). The nitrate overestimation of GEOS-Chem is consistently

reported by previous studies for the United States (Heald et al., 2012; Schiferl et al., 2014; Zhang et al., 2012; Zhu et al., 2013), South Asia (Gu and Liao, 2015), and East Asia (Wang et al., 2013). There have been some efforts to find the possible cause of the nitrate overestimation (e. g. the uptake efficiency of $N_2O_5$ on aerosols, the reaction rate for the formation of nitric acid, dry deposition velocity, boundary layer height, and the uptake of nitric acid on coarse mode dust or sea salt), but this issue is not still resolved yet (Heald et al., 2012; Zhang et al., 2012; Zhu et al., 2013). An investigation of nitrate overestimation is beyond the scope of this study, and will be conducted in future studies.

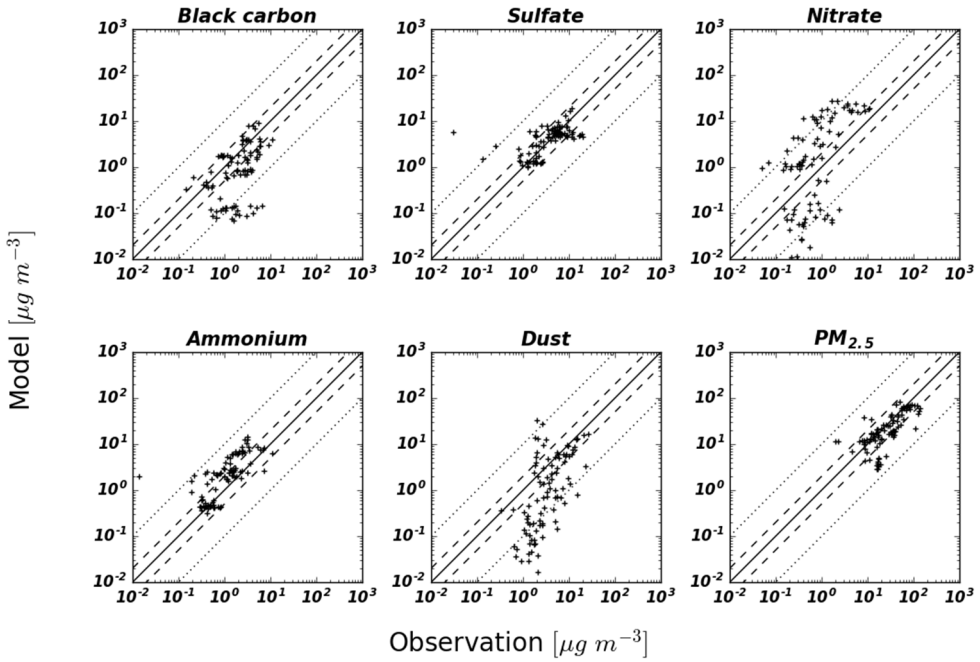


Figure 5.3. Scatter plots of BC, sulfate, nitrate, ammonium, dust, and $PM_{2.5}$ between SPARTAN observations (x-axis) and the model (y-axis). The 1:1 line (solid), 2:1 lines (dashed), 10:1 lines (dotted) are indicated.

The comparison of BC shows the relatively better result with a regression slope of 0.94, compared to nitrate. However, BC concentration is underestimated by 37%, and this underestimation occurs mainly in Manila (10 of 13 points below 10:1 line in Figure 5.3). I find that the model grid box corresponding to this site mostly consists of the sea (Figure 5.4). The spatial resolution of the model (2° x 2.5°) is too coarse to capture local sources on the island.

For the comparison of dust, I infer observed dust mass concentrations following the SPARTAN speciation of Snider et al. (2016). They calculated the dust mass by multiplying [Al + Fe + Mg] by 10 based on the elemental composition of natural dust by Wang (2015). Although this calculation seems oversimplified, I find that the method of Snider et al. (2016) is similar to the method of Malm et al. (1994) for estimating dust mass concentrations based on observed trace metal concentrations (regression slope of 1.0 and correlation of 0.98). Similar to BC, dust concentrations in the model are lower by 25% relative to the observations. This underestimation is also chiefly induced by the coarse resolution of the model at island sites (Manila and Bandung, Figure 5.5).

Simulated $PM_{2.5}$ concentrations are generally in good agreement with the observations (R = 0.76) with slight low bias in mean concentrations (-24%). The performance of the model is comparable to that of global $PM_{2.5}$ estimates constrained by satellite AOD observations (R = 0.73-0.81 and regression slopes of 0.68-0.96) (van Donkelaar et al., 2015), which gives

some confidences in reproducing AOD and SSA.

Table 5.4. Statistical parameters for the evaluation of the model against global aerosol mass concentration observation networks. Regressions slopes and Y-intercepts are computed using the reduced-major-axis method (Hirsch and Gilroy, 1984).

| Network | Species | Slope | Y-ict | R | NMB | RMSE |
|---|---|---|---|---|---|---|
| AMS | Sulfate | 0.77 | 1.31 | 0.78 | 0.17 | 2.25 |
| | Nitrate | 0.84 | 0.68 | 0.62 | 0.40 | 2.04 |
| | Ammonium | 0.69 | 0.71 | 0.78 | 0.21 | 1.18 |
| | Organics | 0.59 | 0.18 | 0.36 | -0.37 | 4.77 |
| SPARTAN | BC | 0.94 | -0.80 | 0.47 | -0.37 | 2.20 |
| | Sulfate | 0.75 | 1.02 | 0.48 | -0.05 | 3.84 |
| | Nitrate | 3.60 | 0.45 | 0.68 | 2.92 | 7.66 |
| | Ammonium | 1.72 | 0.48 | 0.59 | 1.01 | 3.03 |
| | Dust | 1.14 | -1.88 | 0.38 | -0.25 | 6.00 |
| | $PM_{2.5}$ | 0.70 | 2.37 | 0.76 | -0.24 | 21.65 |

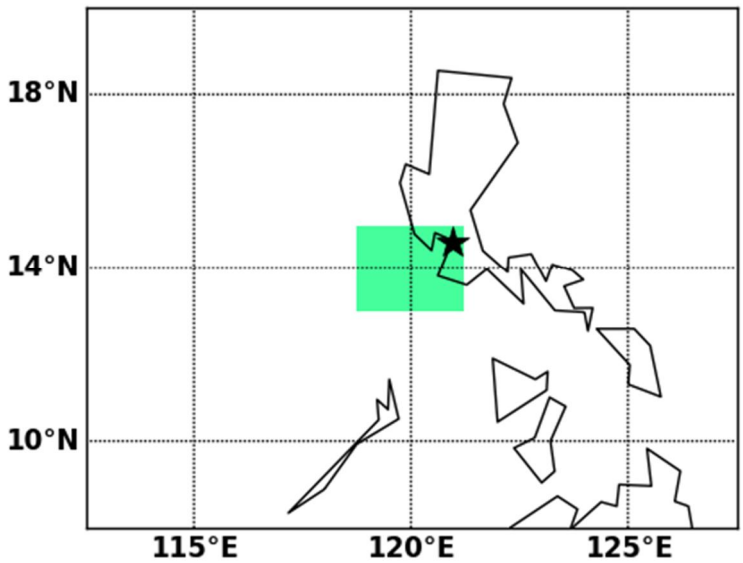


Figure 5.4. Observation site of SPARTAN network at Manila, Philippines. Black star indicates observation point and green box represents model grid box for the observation site.

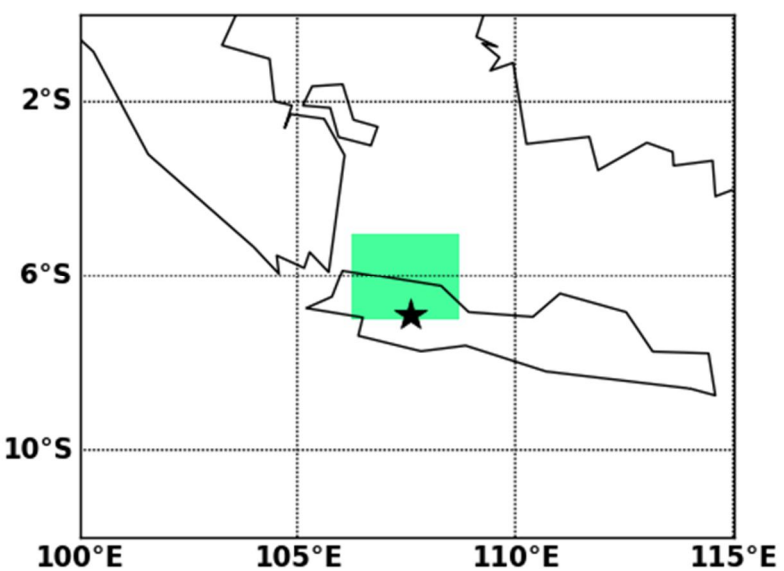


Figure 5.5. Same as Figure 5.4 but for the observation site of SPARTAN network at Bandung, Indonesia.

### 5.2.2. AOD and SSA

The model appears to well capture the spatial and temporal (monthly) variability of observed $PM_{2.5}$ above. It may result from the combination of the nitrate overestimation and the OA underestimation. To ensure the reliability of the model for AOD and SSA evaluation in this Chapter, I also select simulated results at AERONET sites, which meet the following criteria: (1) Differences between the monthly mean observed and simulated concentrations of each aerosol species (inorganics, OA, BC, and dust) should be less than a factor of two at surface networks (AMS and SPARTAN). (2) Sites of the AERONET and the AMS (or SPARTAN) should be in the same model grid or adjacent model grids. I can apply stricter criteria for our data selection, but they make too few data available for the analysis. The conclusions, however, are found to be insensitive to the criteria used as discussed below.

Figure 5.6(a) shows the scatterplot of simulated versus observed AOD at 500 nm with the base case (GEOS_E). I find that the statistics of AOD evaluation is very similar to those of $PM_{2.5}$. Slopes are 0.68 and 0.70, correlation coefficients are 0.76, and NMBs are -20% and -24%, for AOD and $PM_{2.5}$, respectively. From this result, I conclude that aerosol optical property calculation in FlexAOD is properly performed. When I filter out data at AERONET sites using the criteria above, the model shows the improved statistics against the observations – NMB is reduced to -10% and

the correlation coefficient is increased to 0.82 (Figure 5.6(b)).

Figure 5.7(a) and 5.7(b) are points to points comparisons of SSA with all AERONET sites for 440 nm and 870 nm. The model well simulates SSA at 870 nm in common with the evaluation of AOD at 500 nm, but significantly overestimates the observed SSA at 440 nm. The SSA of the model (0.949) is higher than that of the AERONET (0.897) by 0.052. In other words, the model underestimates the observed absorption (1-SSA) by -50%. Although the model underestimates BC by -37%, the model also underestimates scattering aerosols ($PM_{2.5}$ minus BC) by -23%. Therefore, this SSA overestimation can be caused by other factors rather than the underestimation of BC mass concentration. This overestimation is similar to the result in Chapter 4.4.2 with the GEOS-Chem version 9.1.2 against AERONET. The reasons for this overestimation will be investigated in following Chapters.

Figure 5.7(c) and 5.7(d) represent comparison results similar to the Figure 5.7(a,b) but using filtered data. The model shows the improved result especially for SSA at 440 nm - correlation is increased to 0.5 from 0.34, which is analogous to the evaluation result of AOD at 500 nm. From these results, I conclude that the model simulation capability of AOD and SSA is improved when I select AERONET sites where the model shows good results against the AMS and SPARTAN network. Hereafter, I use these filtered AERONET sites for the sensitivity studies below.

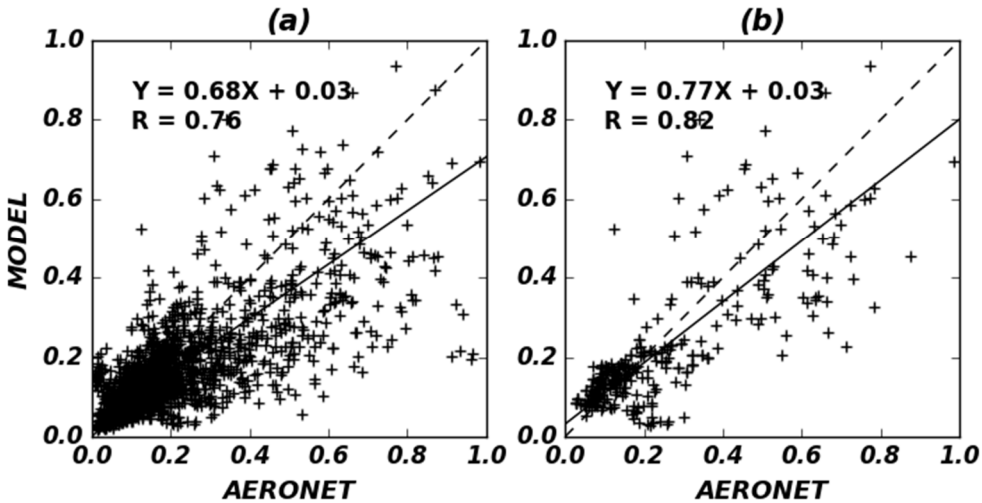


Figure 5.6. Scatter plot of simulated versus observed AOD at 500 nm from 2008 to 2010 for (a) all AERONET points and (b) AERONET points constrained by model evaluation against AMS and SPARTAN network. Reduced major axis regression is shown along with the regression equation and R. Each point indicates monthly averaged AOD when the number of observation is greater than 10 days.

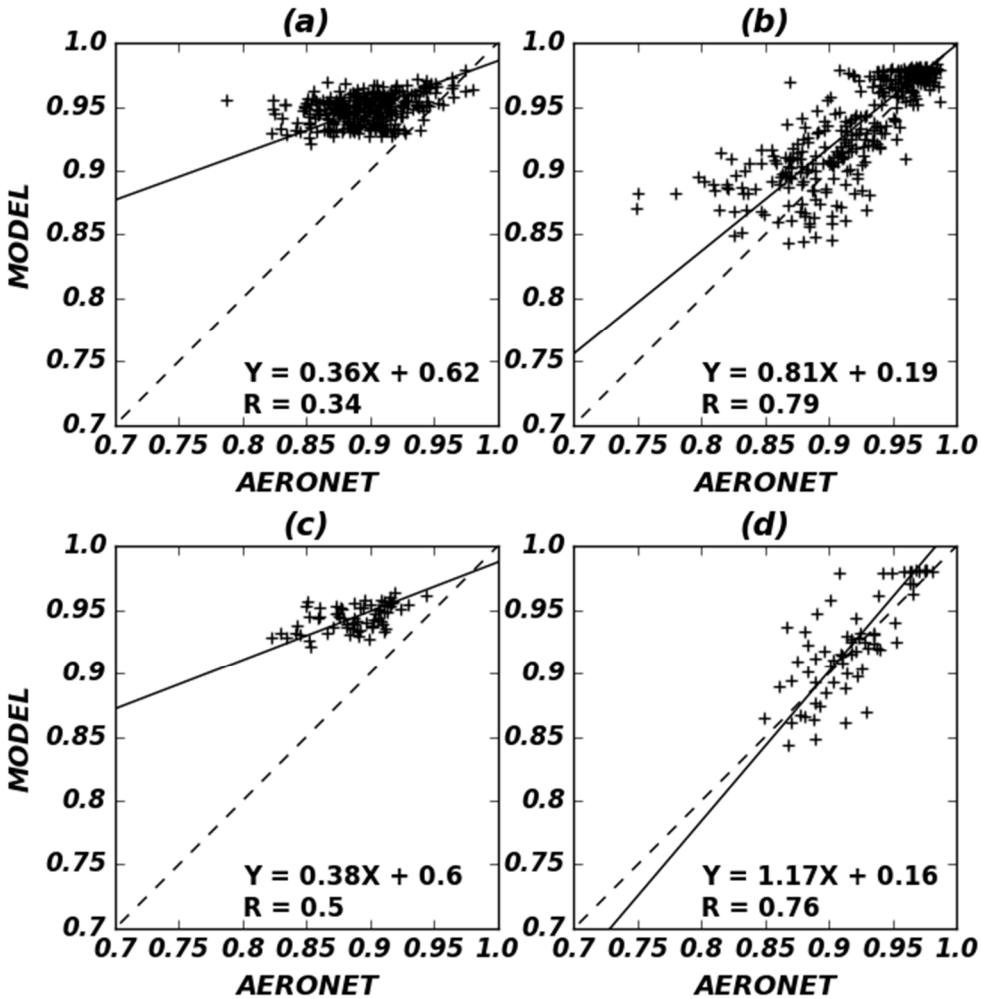


Figure 5.7. Scatter plots of simulated versus observed SSA at 440 (a,c) and 870 nm (b,d) from 2008 to 2010. All available AERONET sites are used for (a,b) and filtered AERONET sites are used for (c,d). Reduced major axis regression is shown along with the regression equation and R. Each point indicates monthly averaged SSA when the number of observation is greater than 10 days, and AOD at 440 nm is greater than 0.4.

## 5.3. SSA sensitivity

In this Chapter, I investigate the sensitivity of calculated SSA values to four factors: BC physical properties, aerosol mixing states, the inclusion of BrC, and dust size distributions. I compare calculated values against the observed SSA at 440 and 870 nm from the AERONET sites over the globe. I thoroughly examine statistics of simulated versus observed SSA for the ensemble of AERONET sites in this Chapter to find out the best parameters for the global SSA estimation.

Figure 5.8 shows the comparisons of calculated versus observed SSAs at 440 nm. Calculated values are from four different cases: OP_E, BB_E, BBR_E, and BBHR_E. Corresponding input parameters used in each case are shown in Table 5.3. Calculated mean values of all cases range from 0.927 to 0.952, which are by 4.4-7.2% higher than the observed mean SSA of 0.888. The lowest value is from OP_E, which is mainly caused by the lowest BC particle density of 1.0 g $cm^{-3}$. Because the particle density is inversely proportional to the number concentration for a given mass concentration, it causes the increase of BC absorption.

The effects of BC internal mixings on SSA calculation is shown in Figure 5.9. I find that both homogeneous and core-shell internal mixing assumptions lead to a significant decrease of SSA (0.812-0.851) at 440 nm. Furthermore, NMBs of AOD are decreased to -52% with internal mixing

cases (GEOS_H and GEOS_C) from -10% with external mixing case (GEOS_E) (Table 5.7). The decreased AODs with internal mixing compared to the external mixing are by -34 – -37% and are because of the decrease of aerosol numbers with the increased size of each aerosol, which is consistent with the previous study by Curci et al. (2015).

The inclusion of BrC absorption also reduces the SSA overestimation (Figure 5.10(a)). Mean SSA is decreased by 0.015. The regression slope is also increased from 0.38 to 0.53. The correlation coefficient is also slightly increased (0.56). Statistics of AOD at 500 nm for GEOS_BR_E are almost the same as those of GEOS_E, because there is no change of mixing states and size distributions of aerosols (Table 5.4).

The use of dust size distributions suggested by Kok (2011) (GEOS_DK_E) and Zhang et al. (2013) (GEOS_DI_E) improves the agreement of calculated SSA with the observations at 440 nm in terms of regression slopes and biases (Figure 5.10(b) and (c)). However, correlations are slightly degraded as a result of more widely scattered points affected by high dust concentrations. SSA with the GEOS_DK_E case is lower than that in GEOS_DI_E case owing to the relatively larger mass of coarse mode dust aerosols in Kok (2011).

Figure 5.11 shows the combined effects of both BrC absorption and dust size distribution on the 440 nm SSA calculation. All four sensitivity cases show improved results although there still exists the overestimation of SSA in the model. I speculate that this remaining gap could be reduced

when I consider strongly absorbing BrC as some studies reported (Alexander et al., 2008; Chung et al., 2012). However, it is too uncertain whether the strongly absorbing BrC is dominant globally. The reported BrC absorptions vary by two orders of magnitude (Jo et al., 2016). More studies are needed to clarify the presences of strongly absorbing BrC.

On the other hand, I find that the correlation coefficient and regression slope decrease as the radius of BC increases. I surmise that the use of spherule size radius (~0.02 μm) seems to be more appropriate than the aggregate size radius (~0.1 μm) for the calculation with the Mie theory. However, this result can be affected by many factors and therefore it is difficult to generalize the use in this study.

Contrary to the comparisons of the SSA at 440 nm, the model shows different results for the SSA at 870 nm (Figure 5.12). Aerosol absorption at 870 nm is mainly affected by BC rather than BrC and dust (Yang et al., 2009). Therefore, these differences are mainly caused by size distributions and refractive indices of BC. Since BC is the only contributor to aerosol absorption at 870 nm, I find that the effects of BC refractive index on SSA are more important for the 870 nm than for the 440 nm. The 870 nm SSA decrease by the use of higher refractive index (BB_BR_DI_E - GEOS_BR_DI_E) is -0.017, the absolute magnitude of which is larger than the 440 nm SSA decrease of -0.011 (Table 5.6).

Considering all the evaluations for AOD and SSA above, I find that the GEOS_BR_DI_E case shows the best performance against AERONET

observations. In the following Chapter, I use this case for the DRE calculation and calculate the effects of sensitivity factors on the DRE change.

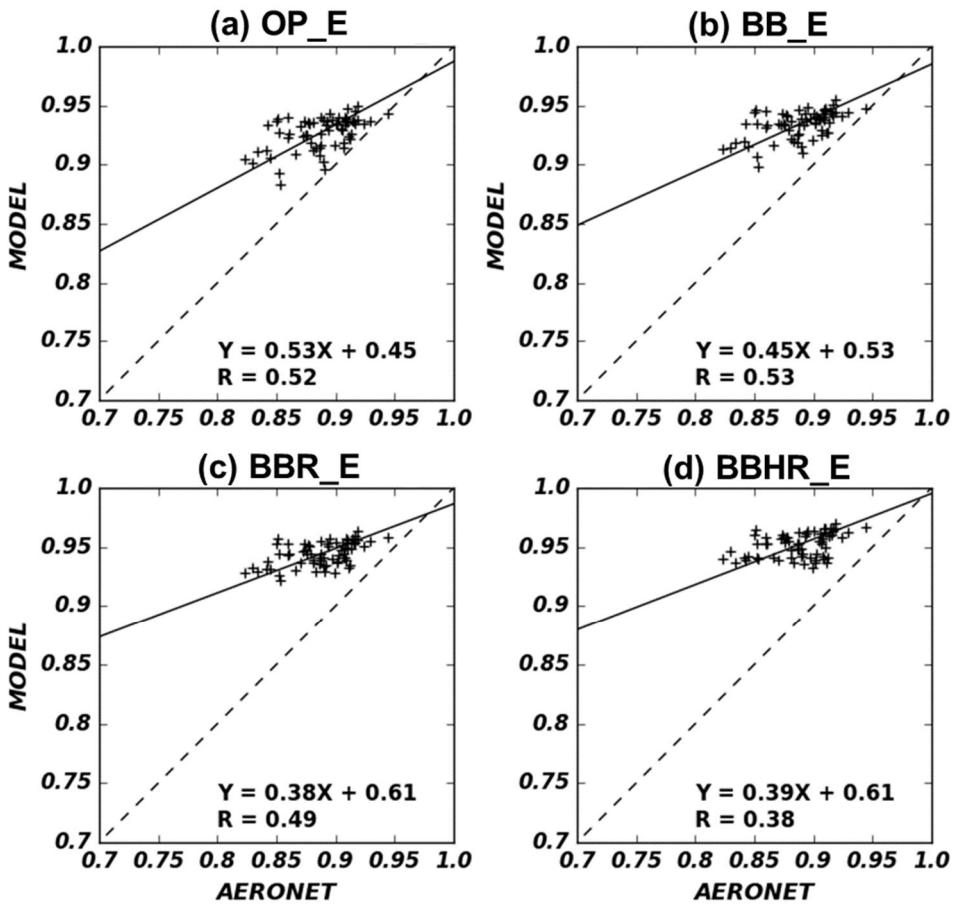


Figure 5.8. Scatter plots of simulated versus observed SSA at 440 nm for sensitivity simulations of (a) OP_E, (b) BB_E, (c) BBR_E, and (d) BBHR_E.

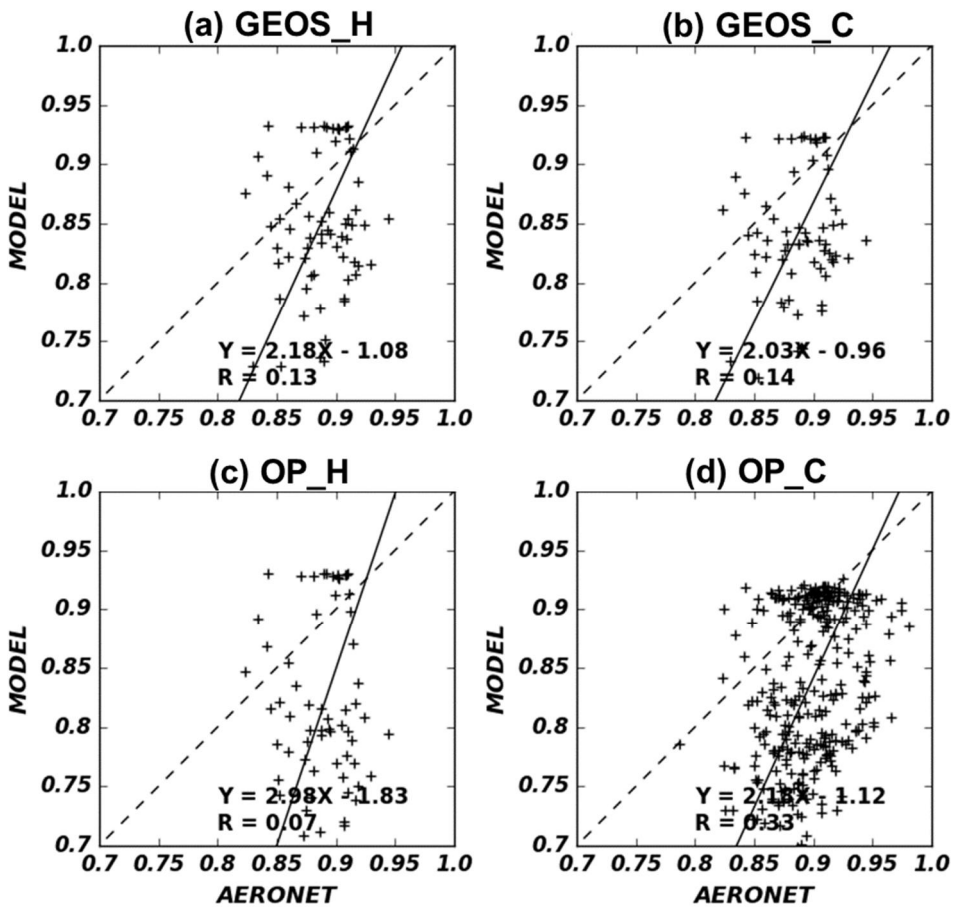


Figure 5.9. Same as Figure 6 but for sensitivity cases of (a) GEOS_H, (b) GEOS_C, (c) OP_H, and (d) OP_C

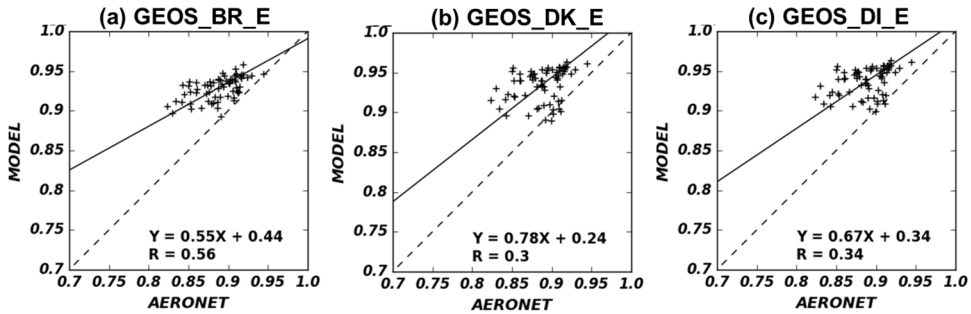


Figure 5.10. Same as Figure 5.6 but for sensitivity cases of (a) GEOS_BR_E, (b) GEOS_DK_E, and (c) GEOS_DI_E.

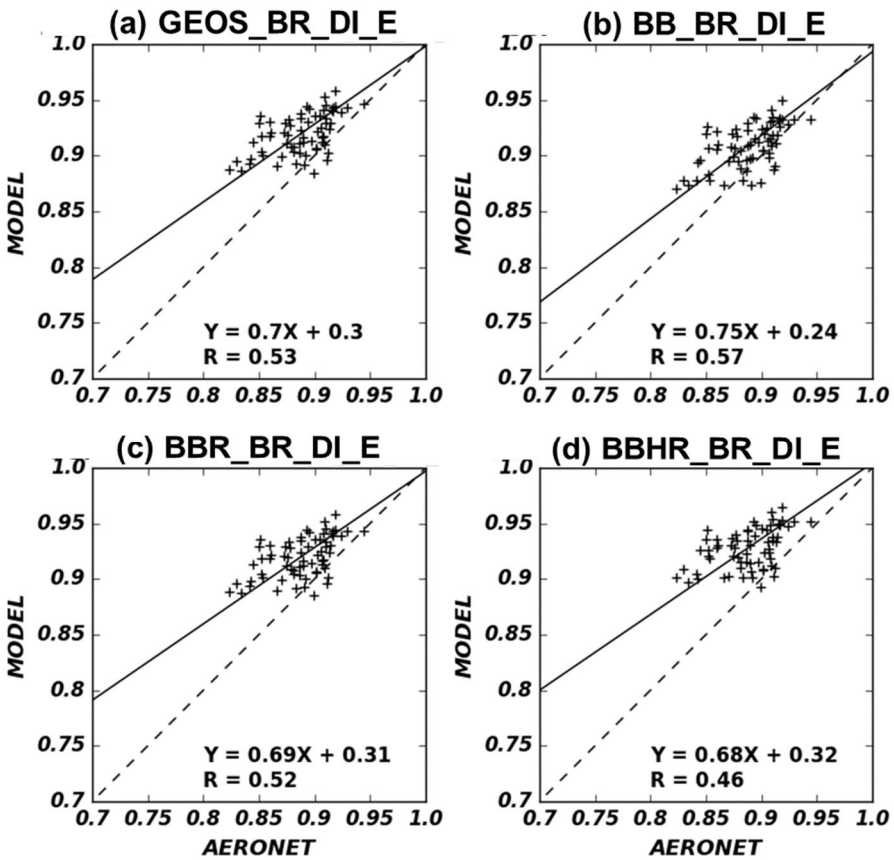


Figure 5.11. Same as Figure 5.6 but for sensitivity cases of (a) GEOS_BR_DI_E, (b) BB_BR_DI_E, (c) BBR_BR_DI_E, and (d) BBHR_BR_DI_E.

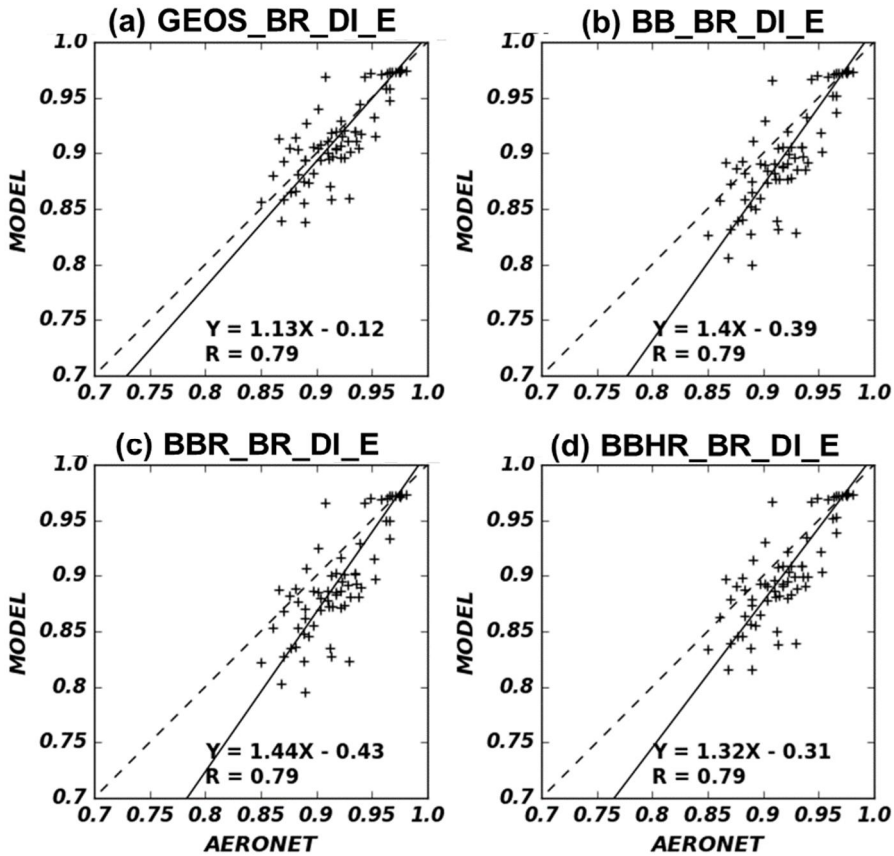


Figure 5.12. Same as Figure 5.9 but for SSA at 870 nm.

Table 5.5. Statistical parameters for the comparison between the simulated and the observed SSA at 440 nm. Observed mean SSA is 0.888.

| Cases | Slope | Yict | R | RMSE | Mean | Mean bias |
|---|---|---|---|---|---|---|
| GEOS_E | 0.38 | 0.60 | 0.50 | 0.061 | 0.944 | 0.057 |
| OP_E | 0.53 | 0.45 | 0.52 | 0.045 | 0.927 | 0.039 |
| BB_E | 0.45 | 0.53 | 0.53 | 0.051 | 0.934 | 0.046 |
| BBR_E | 0.38 | 0.61 | 0.49 | 0.061 | 0.944 | 0.057 |
| BBHR_E | 0.39 | 0.61 | 0.38 | 0.069 | 0.952 | 0.064 |
| GEOS_H | 2.18 | -1.08 | 0.13 | 0.070 | 0.851 | -0.037 |
| GEOS_C | 2.03 | -0.96 | 0.14 | 0.072 | 0.842 | -0.045 |
| OP_H | 2.98 | -1.83 | 0.07 | 0.110 | 0.812 | -0.076 |
| OP_C | 2.53 | -1.43 | 0.09 | 0.099 | 0.817 | -0.071 |
| GEOS_BR_E | 0.55 | 0.44 | 0.56 | 0.046 | 0.929 | 0.041 |
| GEOS_DK_E | 0.78 | 0.24 | 0.30 | 0.054 | 0.934 | 0.047 |
| GEOS_DI_E | 0.67 | 0.34 | 0.34 | 0.055 | 0.936 | 0.049 |
| GEOS_BR_DK_E | 0.79 | 0.22 | 0.49 | 0.038 | 0.917 | 0.029 |
| BB_BR_DK_E | 0.82 | 0.18 | 0.54 | 0.030 | 0.906 | 0.018 |
| BBR_BR_DK_E | 0.77 | 0.23 | 0.48 | 0.038 | 0.917 | 0.030 |
| BBHR_BR_DK_E | 0.78 | 0.23 | 0.41 | 0.046 | 0.925 | 0.038 |
| GEOS_BR_DI_E | 0.70 | 0.30 | 0.53 | 0.039 | 0.920 | 0.032 |
| BB_BR_DI_E | 0.75 | 0.24 | 0.57 | 0.031 | 0.909 | 0.021 |
| BBR_BR_DI_E | 0.69 | 0.31 | 0.52 | 0.039 | 0.920 | 0.032 |
| BBHR_BR_DI_E | 0.68 | 0.32 | 0.46 | 0.047 | 0.928 | 0.040 |

Table 5.6. Same as Table 5.5 but for SSA at 870 nm. Observed mean SSA is 0.918.

| Cases | Slope | Yict | R | RMSE | Mean | Mean bias |
|---|---|---|---|---|---|---|
| GEOS_E | 1.17 | -0.16 | 0.76 | 0.026 | 0.923 | 0.005 |
| OP_E | 1.63 | -0.60 | 0.77 | 0.041 | 0.898 | -0.020 |
| BB_E | 1.45 | -0.42 | 0.77 | 0.033 | 0.908 | -0.010 |
| BBR_E | 1.49 | -0.46 | 0.77 | 0.035 | 0.904 | -0.014 |
| BBHR_E | 1.35 | -0.33 | 0.77 | 0.029 | 0.912 | -0.006 |
| GEOS_H | 1.58 | -0.56 | 0.70 | 0.043 | 0.898 | -0.020 |
| GEOS_C | 1.83 | -0.81 | 0.73 | 0.063 | 0.871 | -0.047 |
| OP_H | 2.09 | -1.05 | 0.72 | 0.071 | 0.868 | -0.050 |
| OP_C | 2.28 | -1.25 | 0.74 | 0.093 | 0.843 | -0.075 |
| GEOS_BR_E | 1.16 | -0.14 | 0.76 | 0.025 | 0.923 | 0.005 |
| GEOS_DK_E | 1.12 | -0.12 | 0.79 | 0.025 | 0.909 | -0.009 |
| GEOS_DI_E | 1.15 | -0.14 | 0.79 | 0.024 | 0.913 | -0.005 |
| GEOS_BR_DK_E | 1.13 | -0.12 | 0.79 | 0.024 | 0.913 | -0.005 |
| BB_BR_DK_E | 1.40 | -0.39 | 0.79 | 0.036 | 0.897 | -0.021 |
| BBR_BR_DK_E | 1.44 | -0.43 | 0.79 | 0.038 | 0.893 | -0.025 |
| BBHR_BR_DK_E | 1.30 | -0.29 | 0.79 | 0.031 | 0.901 | -0.017 |
| GEOS_BR_DI_E | 1.10 | -0.10 | 0.79 | 0.024 | 0.909 | -0.009 |
| BB_BR_DI_E | 1.37 | -0.37 | 0.79 | 0.038 | 0.892 | -0.026 |
| BBR_BR_DI_E | 1.41 | -0.40 | 0.80 | 0.041 | 0.889 | -0.029 |
| BBHR_BR_DI_E | 1.27 | -0.27 | 0.80 | 0.033 | 0.897 | -0.021 |

Table 5.7. Statistical parameters for the comparison between the simulated and the observed AOD at 500 nm. Observed mean AOD is 0.250.

| Cases | Slope | Yict | R | RMSE | Mean | Mean bias |
|---|---|---|---|---|---|---|
| GEOS_E | 0.769 | 0.03 | 0.82 | 0.137 | 0.224 | -0.026 |
| OP_E | 0.791 | 0.03 | 0.82 | 0.135 | 0.230 | -0.021 |
| BB_E | 0.780 | 0.03 | 0.82 | 0.136 | 0.227 | -0.023 |
| BBR_E | 0.784 | 0.03 | 0.82 | 0.136 | 0.228 | -0.022 |
| BBHR_E | 0.775 | 0.03 | 0.82 | 0.137 | 0.226 | -0.025 |
| GEOS_H | 0.489 | 0.00 | 0.73 | 0.214 | 0.120 | -0.130 |
| GEOS_C | 0.488 | 0.00 | 0.73 | 0.214 | 0.120 | -0.130 |
| OP_H | 0.490 | 0.00 | 0.73 | 0.213 | 0.121 | -0.129 |
| OP_C | 0.489 | 0.00 | 0.73 | 0.213 | 0.121 | -0.130 |
| GEOS_BR_E | 0.777 | 0.03 | 0.83 | 0.135 | 0.226 | -0.024 |
| GEOS_DK_E | 0.631 | 0.05 | 0.78 | 0.158 | 0.204 | -0.046 |
| GEOS_DI_E | 0.652 | 0.04 | 0.79 | 0.153 | 0.208 | -0.043 |
| GEOS_BR_DK_E | 0.641 | 0.05 | 0.78 | 0.156 | 0.206 | -0.045 |
| BB_BR_DK_E | 0.652 | 0.05 | 0.78 | 0.154 | 0.208 | -0.042 |
| BBR_BR_DK_E | 0.656 | 0.05 | 0.79 | 0.153 | 0.210 | -0.041 |
| BBHR_BR_DK_E | 0.647 | 0.05 | 0.78 | 0.155 | 0.207 | -0.043 |
| GEOS_BR_DI_E | 0.661 | 0.04 | 0.80 | 0.150 | 0.209 | -0.041 |
| BB_BR_DI_E | 0.672 | 0.04 | 0.80 | 0.149 | 0.212 | -0.038 |
| BBR_BR_DI_E | 0.676 | 0.04 | 0.80 | 0.148 | 0.213 | -0.037 |
| BBHR_BR_DI_E | 0.667 | 0.04 | 0.80 | 0.149 | 0.211 | -0.040 |

## 5.4. Implication for global DRE

Here I calculate the global clear-sky DRE of selected sensitivity simulations in Figure 5.13 by using the rapid radiative transfer model for GCMs (generation circulation models) (RRTMGs) (Iacono et al., 2008). MERRA reanalysis data are used for albedo and other meteorological variables.

Figure 5.13(a) shows the annual mean DRE of the reference simulation (GEOS_E) for 2008-2010. Globally, annual mean DREs are negative except for Northern Africa where weakly absorbing dust concentrations are very high. Absolute magnitudes of DRE are high in regions with heavy biomass burning (Central Africa) and anthropogenic (East Asia) emissions. These global distributions are similar to the result by Heald et al. (2014) (Figure 3 in their paper). Annual mean DRE is -2.62 W $m^{-2}$, which is also comparable to the annual mean DRE (-2.75 W $m^{-2}$) for 2010 by Heald et al. (2014).

The inclusion of BrC absorption increases the DRE by 0.07 W $m^{-2}$, especially for regions with high biomass burning (Africa) and biofuel (Asia) emissions (Jo et al., 2016) as shown in Figure 5.13(e). Note that BrC absorption could be underestimated in this study as discussed in Chapter 5.3, and in turn, the DRE increase by BrC could be underestimated. The DRE increase after modifying the dust size distribution is 0.17 W $m^{-2}$ (Figure 5.13(f)), which is more than two times higher than the DRE increase by BrC

absorption. When I consider both BrC absorption and observationally constrained dust size distribution, the increment of the DRE is 0.26 W $m^{-2}$ (Figure 5.13(g)), which accounts for 10% of the DRE of the reference case.

The inclusion of BrC absorption (-0.015) leads to a more effective decrease of SSA at 440 nm than the change of dust size distribution (-0.008) as shown in Table 5.5. However, their effects on the DRE are different. The relatively higher DRE change (0.17 W $m^{-2}$) shown in Figure 5.13(f) is mainly caused by high dust burden (14.4 Tg), which is 10 – 100 times higher than BC (0.1 Tg) or OA (1.4 Tg) burden. Note that the DRE is calculated by using AOD (~proportional to burden) as well as SSA. Therefore, I conclude that the size distribution of dust plays an important role in the DRE estimation by models, as also reported by Kok et al. (2017).

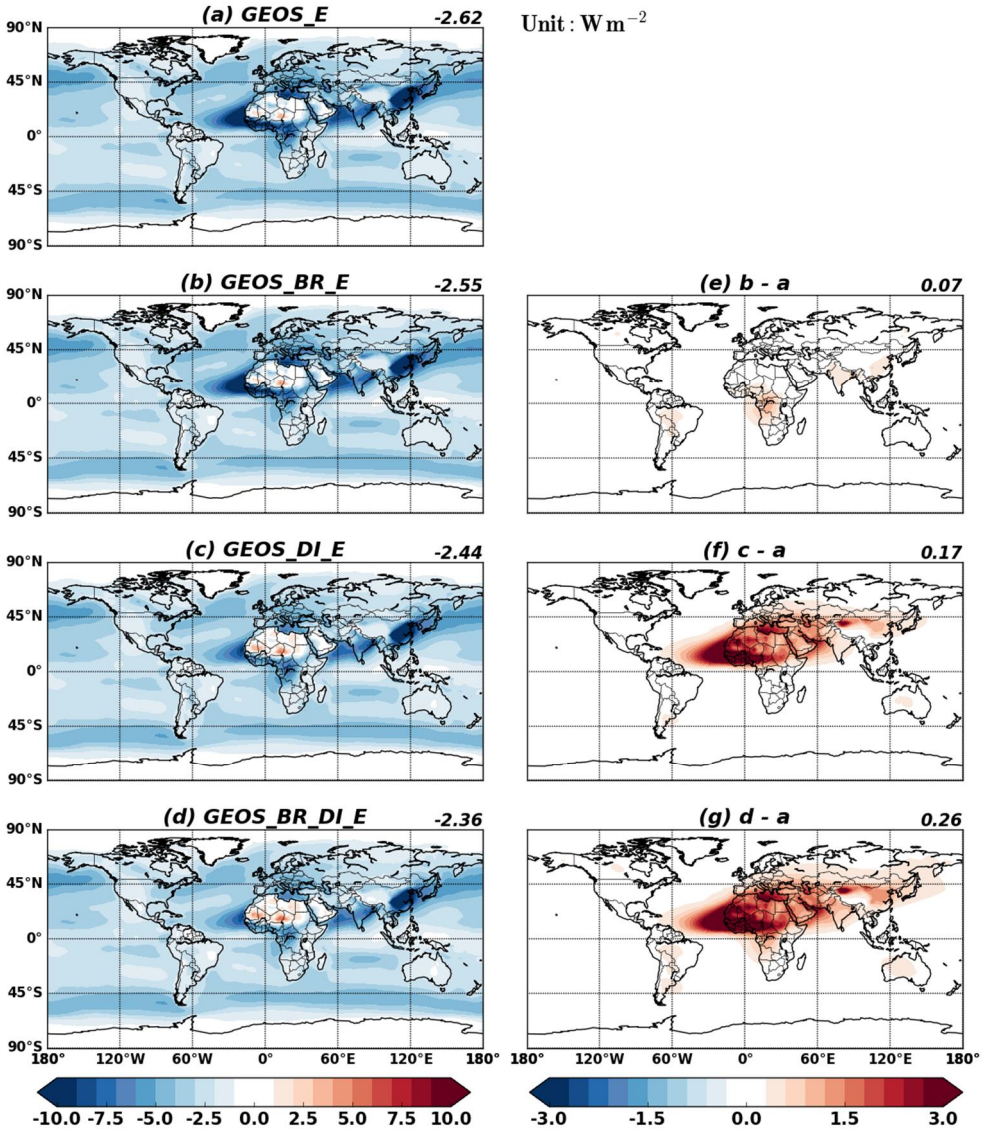


Figure 5.13. Calculated DREs at the top of the atmosphere. Left panels are DREs of (a) GEOS_E, (b) GEOS_BR_E, (c) GEOS_DI_E, and (d) GEOS_BR_DI_E cases. The changes compared with the GEOS_E case are shown in right column.

## 5.5. Suggestions

Although I found that the GEOS_BR_DI_E case showed the best performance against AERONET AOD and SSA, it is difficult to confirm that it can be applied to other studies. There were many factors simultaneously affecting AOD and SSA calculation such as hygroscopic growth factor, which was not discussed in detail. However, I could identify some findings noticeable to future modeling studies using the Mie theory for the aerosol optical property calculations:

1. There was no significant difference of calculated BC absorptions using input parameters of OPAC database and Bond and Bergstrom (2006). The refractive index of Bond and Bergstrom (2006) (1.95 – 0.79i) was higher than that of OPAC (1.74 – 0.44i), and the resulting BC absorption of Bond and Bergstrom (2006) was 49% higher than that of OPAC. However, the low BC particle density of OPAC (1.0 g $cm^{-3}$) increased the BC number concentration and AOD, which enhanced the BC absorption. I found that the mean SSA of OP_E (0.927) was slightly lower than that of BB_E (0.934) (Table 5). Although many previous studies did not provide BC density they used for the Mie calculation (Feng et al., 2013; Jo et al., 2016; Lin et al., 2014), an assumed BC density was critical to SSA calculation and should be provided in the future intercomparison study.

2. The model with external mixing assumption showed the better performance than the model with internal mixing assumptions in a global

sense. Drury et al. (2010) also showed the similar result against aircraft observations. However, there have been many observational studies indicating internal mixture of aerosols (Moffet and Prather, 2009; Oshima et al., 2009; Shiraiwa et al., 2008). There was a possibility that observation points I used were mainly affected by fresh aerosols. Further studies with considering photochemical aging time are needed.

3. The SSA calculation of models in previous studies have been mostly evaluated at 440 – 550 nm (Dai et al., 2015; Jo et al., 2016; Lin et al., 2014). However, SSAs at both shorter and longer wavelengths should be evaluated together for the model evaluation. The calculated SSA could show different performances for different wavelengths because they are affected by different aerosols and wavelength-dependent physical characteristics.

4. BrC absorption and observationally constrained dust size distribution should be considered for the SSA calculation in the model, especially for the shorter wavelength. These factors reduced SSA at shorter wavelength, resulting in a decrease of positive SSA bias at 440 nm generally found in global models.

5. The changes of dust size distribution led to a significant increase of the global DRE, whose value (0.17 W $m^{-2}$) was more than two times higher than the global DRE increase by BrC absorption (0.07 W $m^{-2}$). Global models likely underestimate the global dust DRE because of the overestimation of fine mode dust and underestimation of the coarse mode dust as shown Kok et al. (2017), who constrained the global dust size

distribution using global observations and models.

# Chapter 6. Modeling organic aerosols during KORUS-AQ

East Asia is one of the crucial regions for OAs whose primary anthropogenic sources account for about one-fourth of the global emissions. During KORUS-AQ campaign, not only OAs but also their precursors and oxidants were extensively observed in South Korea, one of the most highly polluted areas in East Asia. I use here a nested version (0.25° X 0.3125°) of the GEOS-Chem to examine the production and distribution of OA during KORUS-AQ. I update the SOA simulation in GEOS-Chem (v10.1) by implementing the recently proposed SOA simulation schemes from Jo et al. (2013) and Hodzic et al. (2016). I evaluate the model by comparing it against aircraft observations and examine the model performance of OA over East Asia.

## 6.1. Observed characteristics of OA

Here I investigate the sources and evolutions of OA with the various aircraft measurements of aerosols and gases during KORUS-AQ campaign. There were 20 research flights (~150 hours) from 2 May to 10 June 2016 over South Korea. They observed air masses influenced by long-range transport, heavy traffic, petrochemical complex, biomass burning, and stagnant conditions.

Figure 6.1 shows the observed mean trends of BC (black) and OA (green) concentrations. Generally, the mean OA concentration increases as the research flight number increases. There were two research flights whose mean OA concentration is higher than 15 μg $m^{-3}$, and these research flights were conducted over Daesan petrochemical complex region. Lowest OA and BC concentrations were observed in the flight number 7, and mean observation altitude of which is a lot higher than that of other research flights.

Mean trends of observed OA/BC and O:C ratio are represented in Figure 6.2. The lowest mean O:C ratio is 0.7, which indicates highly oxidized OA classified as LV-OOA (Canagaratna et al., 2015). Furthermore, these high O:C ratio are higher than those of previous aircraft campaigns including SOAR-1, AMAZE-08, MILAGRO (Heald et al., 2010). The high O:C ratio is usually related with primary biomass burning emissions or

secondary production by chemical aging processes, which is further discussed below.

Figures 6.3-6.6 show the relationship between observed OA

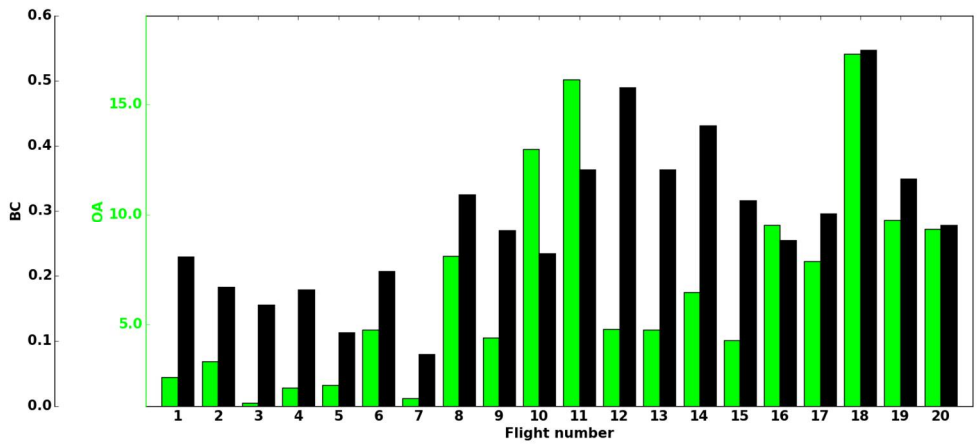


Figure 6.1. Observed mean OA (green) and BC (black) concentrations (y-axis) during KORUS-AQ as a function of research flight number (x-axis). Units are μg $sm^{-3}$ and μgC $sm^{-3}$ for the OA and BC, respectively.

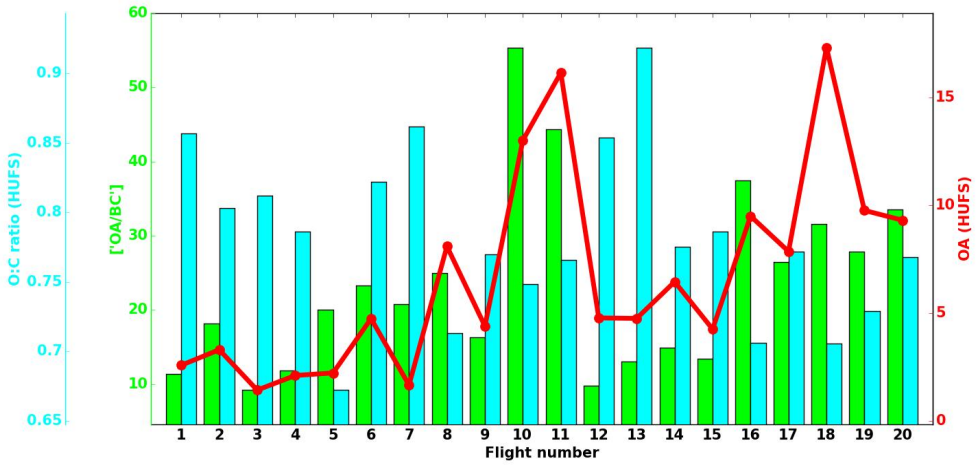


Figure 6.2. Observed mean O:C ratio (sky-blue bar), OA/BC ratio (green bar), and OA concentration (red line). Unit of OA is μg $sm^{-3}$.

concentrations and parent VOC concentrations (monoterpene, isoprene, benzene, and toluene). Observed OA concentrations are positively correlated with all four parent VOC concentrations. Point to point correlations between OA and parent VOCs are around 0.4, except for OA and monoterpene (0.15). Therefore, some OA concentrations are the product from the oxidation of parent VOCs, but there should be other processes as revealed in the low correlation coefficients (0.15 ~ 0.41).

I calculate the photochemical aging time by using observed benzene to toluene ratio in order to examine the effect of chemical aging on OA concentration. Calculated photochemical aging time shows the high positive correlation (0.66) with the observed O:C ratio of OA (Figure 6.7). The O:C

ratio increases as the photochemical aging time increases because of the oxidation of OA by chemical reactions in the atmosphere (Donahue et al., 2012; Jimenez et al., 2009; Denjean et al., 2015). However, the oxidation of OA does not result in the increase of OA mass concentrations as shown in Figure 6.8. A recent study by Hodzic et al. (2015) showed that the photolytic loss of OA significantly affected the OA concentrations. This photolytic loss of OA seems to be significant process rather than the functionalization reactions which can increase the mass concentration of OA.

The relationship between OA and soil dust is also investigated. Figure 6.9 represents the OA concentrations as a function of $Ca^{2+}$ concentrations which is usually used for the calculation of suspended dust particle concentration (Malm et al., 1994; Snider et al., 2016). I find that there is no apparent relationship between the OA and $Ca^{2+}$. The mean OA mass concentration is the lowest when the $Ca^{2+}$ mass concentration is in the highest range (1.0 – 5.0 μg $sm^{-3}$).

Finally, the influence of biomass burning on OA is investigated with the acetonitrile ($CH_3CN$) concentration which has been known as a molecular marker of biomass burning. I find that the strong positive relationship between the observed OA and the acetonitrile concentrations (Figure 6.10). The point to point correlation is 0.73, which is the higher than the correlations of the OA and other chemical species above. Furthermore, there is also a strong positive relationship between the OA and BC (Figure 6.11). These results indicate the high contribution of primary sources on the

OA mass concentrations, especially from the biomass burning sources.

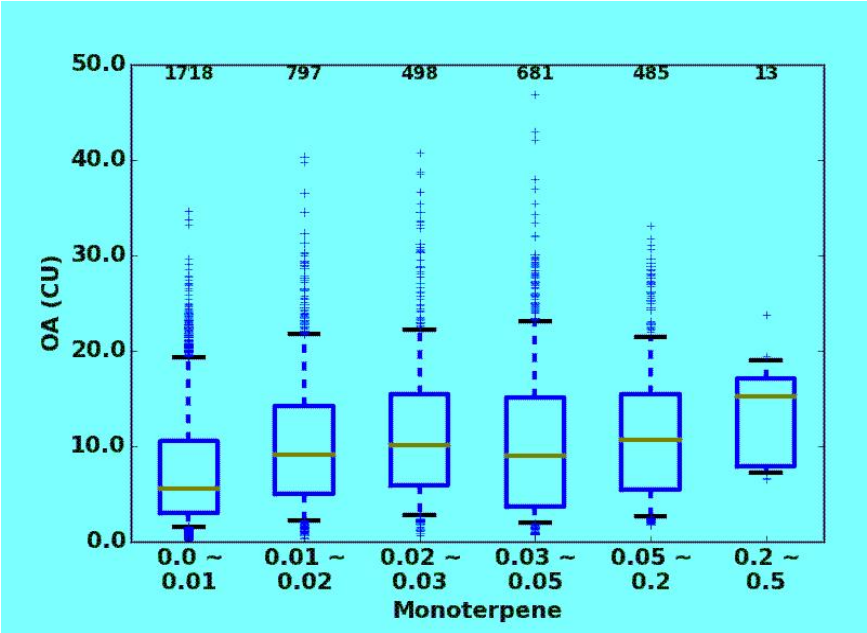


Figure 6.3. The OA concentration as a function of monoterpene concentration. The box and whisker plots show the median (red line), 25$^{th}$ and 75$^{th}$ percentiles (boxes), and 10$^{th}$ and 90$^{th}$ percentiles (whiskers) below 2km. Units are μg sm$^{-3}$ and ppbv for the OA and the monoterpene, respectively.

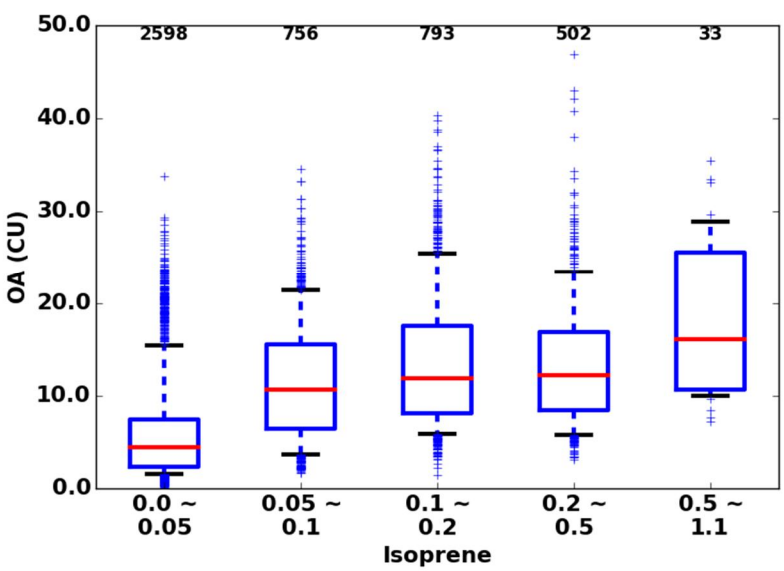


Figure 6.4. Same as Figure 6.3 but for the OA concentration as a function of isoprene concentration. Unit of the isoprene is ppbv.

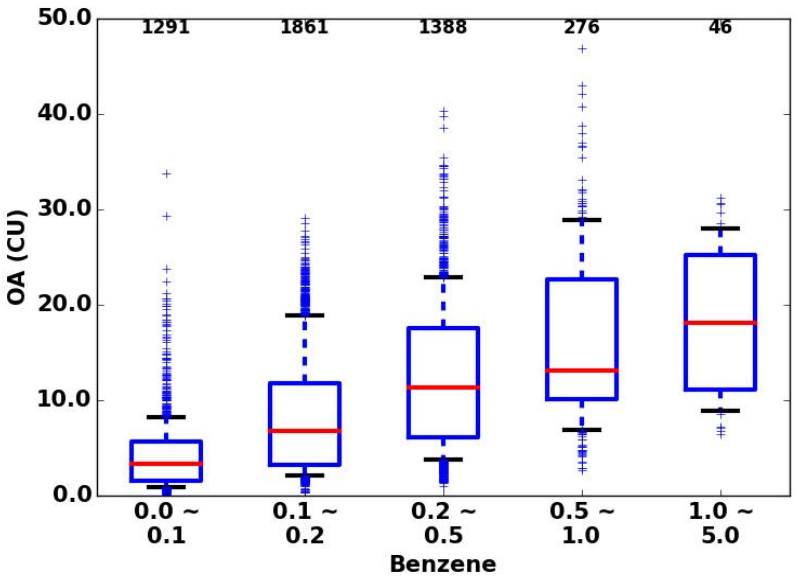


Figure 6.5. Same as Figure 6.3 but for the OA concentration as a function of benzene concentration. Unit of the benzene is ppbv.

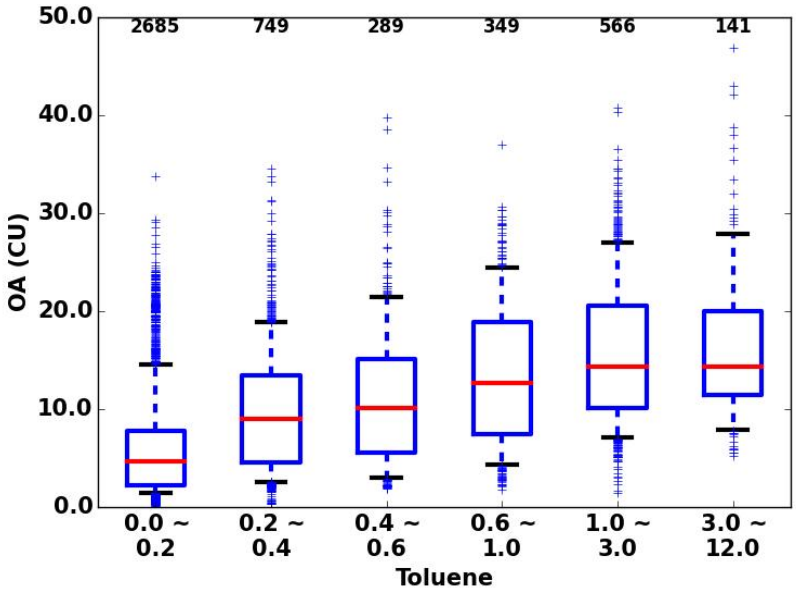


Figure 6.6. Same as Figure 6.3 but for the OA concentration as a function of toluene concentration. Unit of the toluene is ppbv.

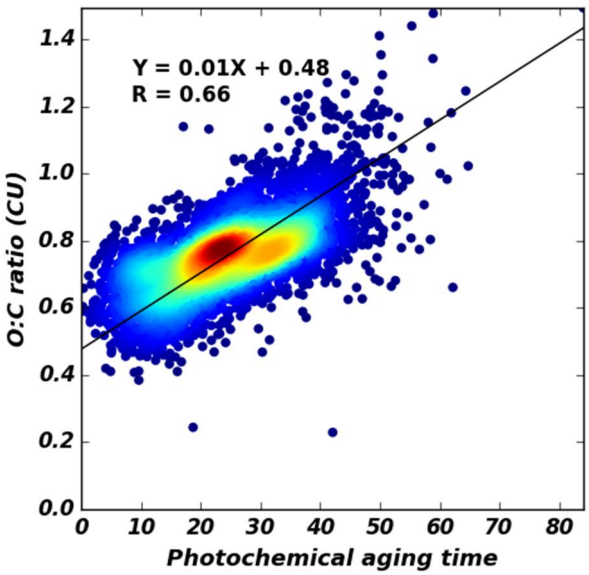


Figure 6.7. Scatterplot between the observed O:C ratio and calculated photochemical aging time. Unit of photochemical aging time is hour.

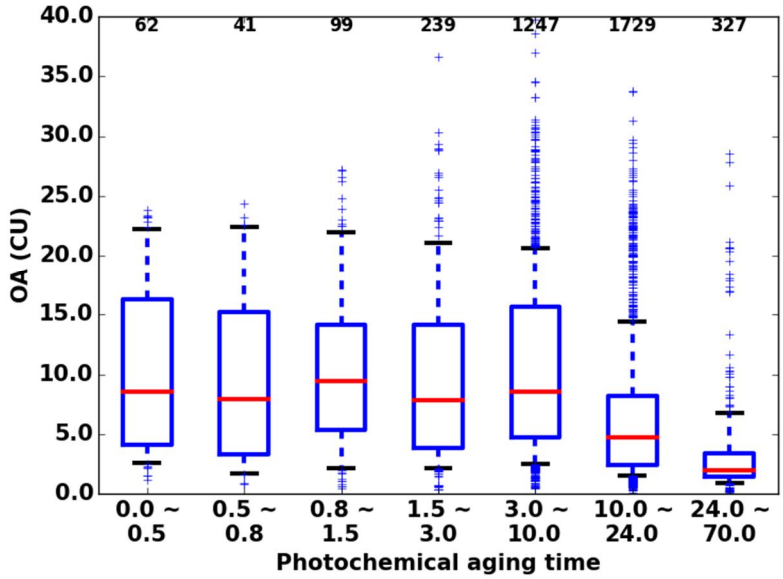


Figure 6.8. Same as Figure 6.3 but for the OA concentration as a function of photochemical aging time. Unit of the photochemical aging time is hour.

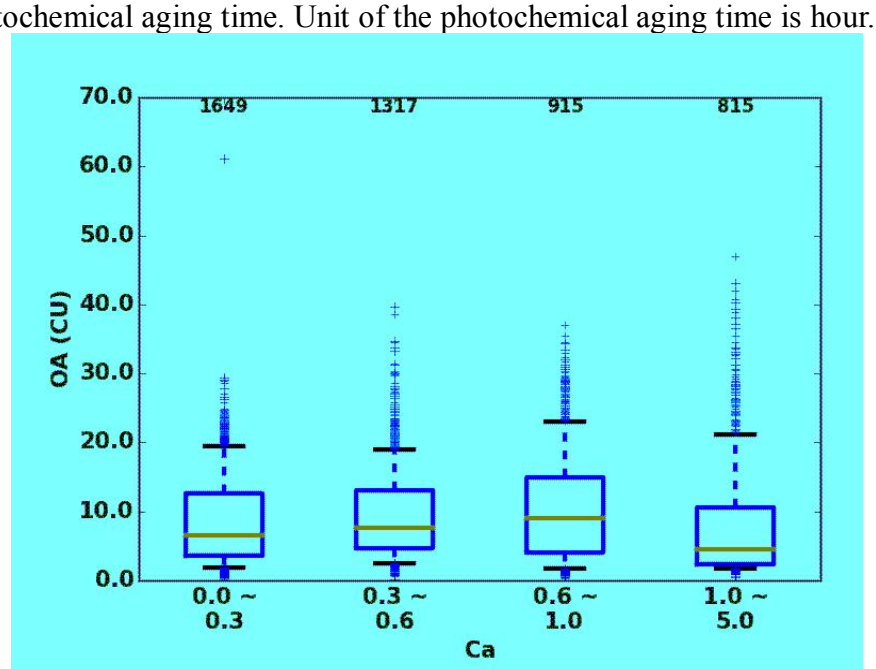


Figure 6.9. Same as Figure 6.3 but for the OA concentration as a function of $Ca^{2+}$. Unit of $Ca^{2+}$ is μg $sm^{-3}$.

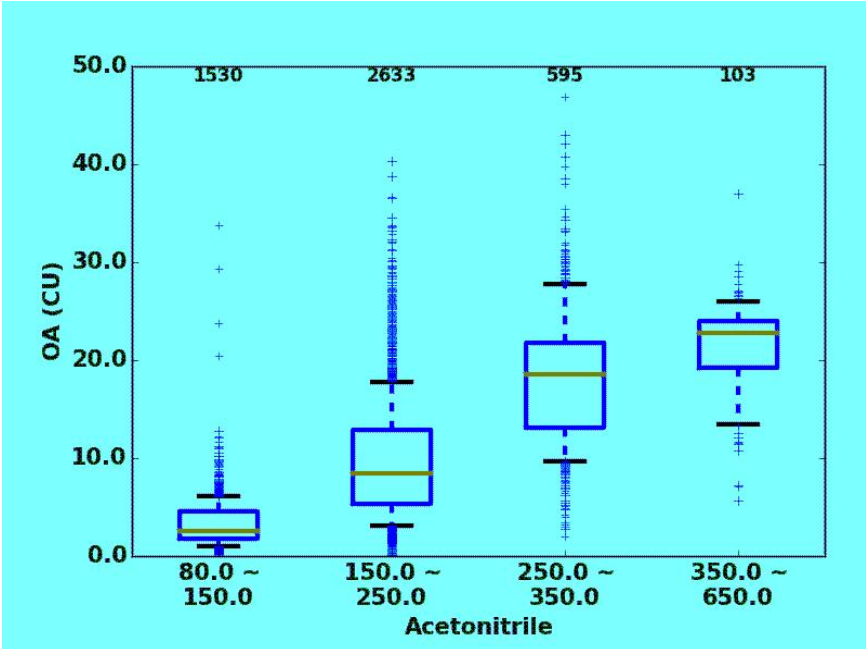


Figure 6.10. Same as Figure 6.4 but for the OA concentration as a function of acetonitrile ($CH_3CN$). Unit of acetonitrile is pptv.

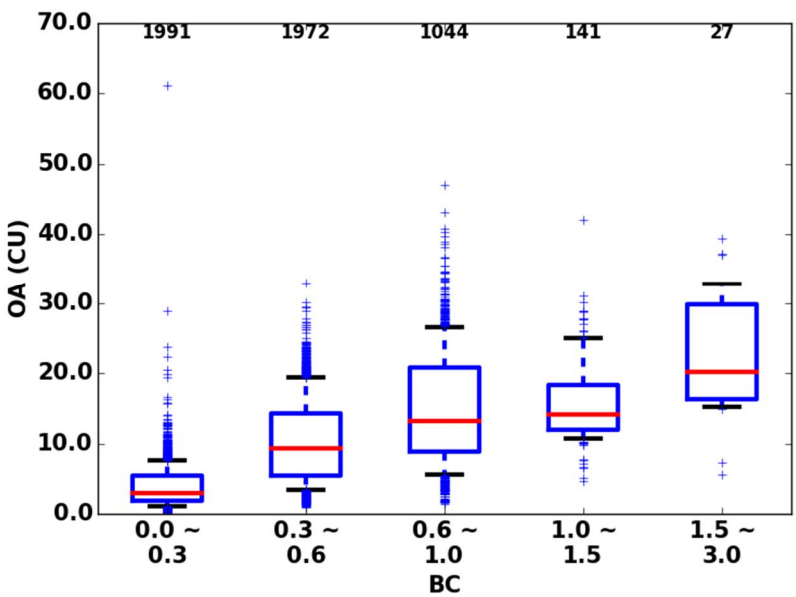


Figure 6.11. Same as Figure 6.4 but for the OA concentration as a function of BC. Unit of BC is $\mu gC\ m^{-3}$.

## 6.2. Evaluation of simulated OA and its implication

GEOS-Chem v10.1 uses the SOA simulation scheme from Pye et al. (2010), which includes NOx-dependent SOA yields and nitrate radical oxidation isoprene. Based on this scheme, I implement the SOA simulation scheme developed in Chapter 3 (Jo et al., 2013) to GEOS-Chem v10.1. Furthermore, I also implement the SOA simulation scheme recently developed by Hodzic et al. (2016). Hodzic et al. (2016) updated the SOA scheme of Jo et al. (2013) by including wall-corrected yields, photolytic and heterogeneous oxidation loss processes. I evaluate simulated OA concentrations with three different SOA schemes above to investigate the effects of SOA scheme on the OA simulations.

Following the work by Hodzic et al. (2016), I further consider the SOA formation from the oxidation of alkanes with higher molecular weights (SVOC and IVOC) for the SOA schemes by Jo et al. (2013) and Hodzic et al. (2016). The emissions of SVOCs and IVOCs are considered based on the report by Jathar et al. (2014). I include SVOC emissions as 60% of POA emissions and IVOC emissions as 20% of total NMVOC emissions.

Figure 6.12 shows the comparison between simulated and observed of BC and OA. The model simulates fairly well the BC concentration with a correlation of 0.71 and NMB of 6%. Because BC is chemically inert and not produced by secondary processes in the atmosphere, the BC concentrations are mainly affected by emission and transport processes in the model.

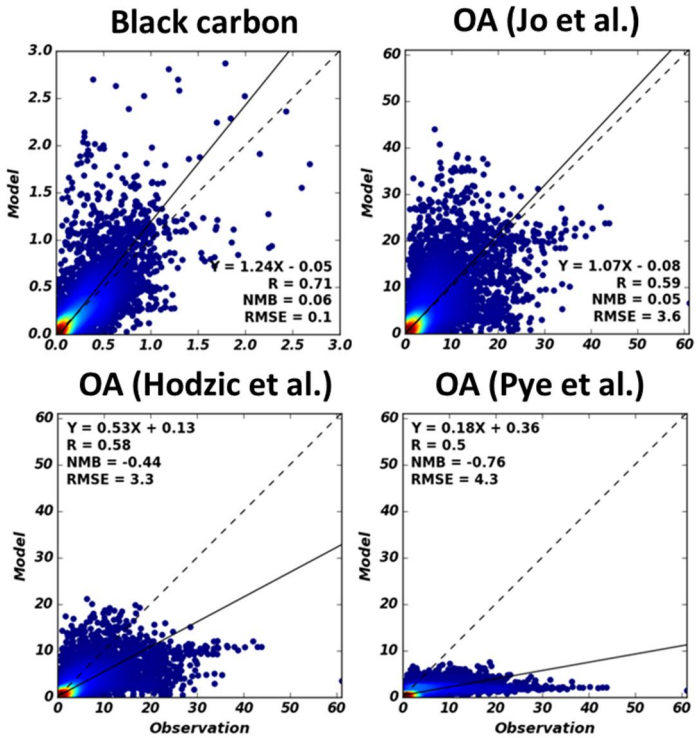


Figure 6.12. Scatterplots of the modeled (y-axis) versus observed (x-axis) BC and OA. Units are μgC $sm^{-3}$ and μg $sm^{-3}$ for the BC and OA, respectively.

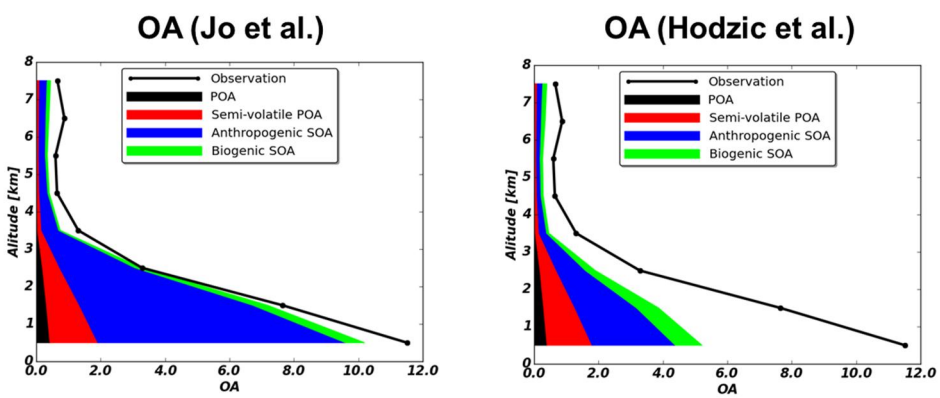


Figure 6.13. Mean vertical profiles of OA concentrations. Observations are shown in black line. Shaded colors indicate the simulated OA concentrations from different sources. Model values are sampled along the flight tracks. Unit is μg $sm^{-3}$.

Therefore, the transport processes seem to be well simulated in the model.

On the other hand, OA concentration is highly affected by chemical reactions in the atmosphere. The base model simulation (Pye et al., 2010) shows the significant underestimation of OA (-76%), which is mainly caused by the absence of chemical aging reactions in this SOA scheme. The model with Hodzic et al. (2016) scheme shows the improved result in terms of NMB, but still underestimates the observed OA concentration (-44%). I find that the model with Jo et al. (2013) scheme shows similar mean OA concentration in comparison with the observed OA: NMB is 5%, and the regression slope is 1.07. However, there are many points the model overestimates or underestimates in the scatterplot, resulting in higher RMSE (3.6 μg $sm^{-3}$) than that (3.3 μg $sm^{-3}$) by the model with the SOA scheme of Hodzic et al. (2016).

Figure 6.13 represents the mean vertical profiles of OA concentrations for observations (black line) and models (shaded colors). Similar vertical shapes are shown for the observation and the model with Jo et al. (2013) scheme. The contribution of anthropogenic SOA is the highest, which results from the chemical aging reactions with the VBS. On the other hand, the model with Hodzic et al. (2016) scheme underestimates the observed OA by a factor of two due to additional loss processes of SOA (photolytic and heterogeneous oxidation loss processes). However, it shows higher concentrations for biogenic SOA in comparison to the model with Jo et al. (2013) scheme because of increased wall-corrected yields.

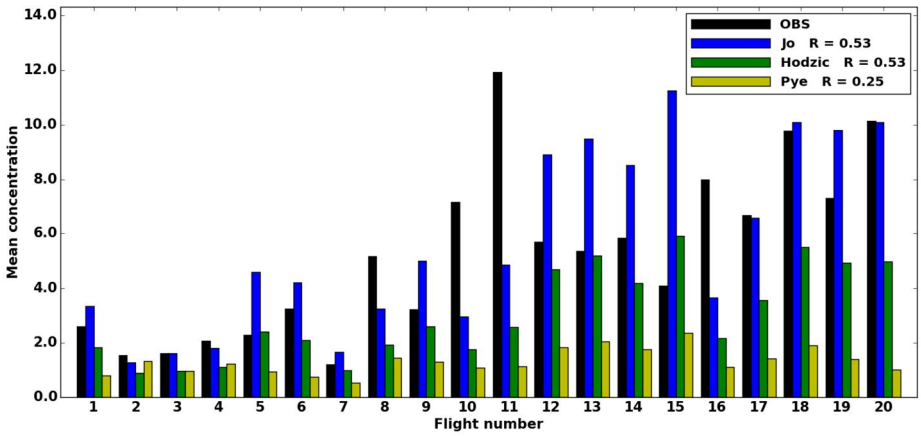


Figure 6.14. Mean OA concentration trends during KORUS-AQ for the observation (black) and simulation results (blue, green, and yellow).

I calculate the mean OA concentration trends during KORUS-AQ for the observation and model (Figure 6.14). Although the model with Jo et al. (2013) scheme shows similar mean OA concentration compared to the observed mean OA (Figures 6.12 and 6.13), there is a factor of two difference in some research flights such as flight number 11. The observed OA concentration in the research flight number 11 (12 μg $sm^{-3}$) is more than two times higher than the simulated OA concentration (5 μg $sm^{-3}$). During the flight number 11, the highest acetonitrile concentration was observed (mean concentration of 270 pptv). However, the biomass burning inventory (FINN version 1.5) shows almost negligible emission amount during the day of flight number 11. Because 91% of burned area in the Korean peninsula is less than 1 ha, it is difficult to detect the biomass burning emissions with the satellite. Further study is needed to detect and make appropriate biomass burning emissions.

On the other hand, the model with Jo et al. (2013) scheme overestimates the observed OA concentrations by two times in the flight number 15. However, the model with Hodzic et al. (2016) scheme shows no significant overestimation in this flight. As shown in Figure 6.8, the observation indicates photolytic loss process of OA and the model with Hodzic et al. (2016) scheme employs it. Although there are large uncertainties in calculating loss rate of photolytic loss (Hodzic et al., 2015), both the observations and models indicate the necessity of representing the photolytic loss of OA.

# Chapter 7. Summary and conclusion

Aerosols dominate the uncertainty associated with the total anthropogenic driving of climate change. This large uncertainty was caused by the limitation of models reproducing various characteristics of aerosols in the real atmosphere. The main goal of this dissertation was to reduce the gap between observations and models. The objectives of the dissertation were to (1) improve the simulation capability of OA mass concentration by considering the chemical aging process of SOA (2) develop the method to explicitly simulate BrC in the model (3) examine key factors of SSA calculation (4) investigate the model performance in a heavily polluted urban atmosphere.

To improve the simulation capability of OA mass concentration, I implemented the VBS approach for SOA simulation in GEOS-Chem to simulate the chemical aging of SOA and examined its effects on the SOA burden and its climate implications. Using the model with different aging conditions, I conducted extensive evaluations of the model by comparison with observations in various regions (global, the United States, Europe, East Asia) and found that the model with the $4 \times 10^{-11}$ $cm^3$ $molecule^{-1}$ $s^{-1}$ aging constant is most suitable for simulating SOA aging with the VBS approach. I computed the DRE of SOA species with aging and no aging conditions. The effect of chemical aging on the global mean SOA DRE was -0.07 W $m^{-2}$,

comparable to the AeroCom multi-model mean OA DRF of -0.13 W $m^{-2}$. Because of its patch-like distribution, it was more important regionally, especially for industrialized regions. The DRE decreased over the eastern United States, western Europe, and East Asia because chemical aging was 2.5-4 times higher than the globally decreased mean DRE.

For the estimate of OA absorption, I first estimated primary BrC emissions from biomass burning and biofuel use based on the relationship between AAE and MCE. The estimates of primary BrC emissions were 3.9 ± 1.7 and 3.0 ± 1.3 TgC $yr^{-1}$ from biomass burning and biofuel use, respectively. The secondary BrC source was estimated to be 5.7 TgC $yr^{-1}$ from the aromatic oxidation. With explicit BrC emissions, a coupled oxidant-aerosol simulation was conducted for 2007 to obtain the spatial and temporal distributions of BrC concentrations. I first evaluated the model by comparing the simulated versus observed BrC absorption in the United States and found that the model successfully reproduced the observed seasonal variation of light absorption by WSOC in the southeastern United States, whereas the model significantly underestimated secondary BrC over the Los Angeles basin. Using the best results, I estimated the DRE of BrC to be close to zero at the top of the atmosphere because the imaginary refractive indices of BrC are in the midpoint between those of BC and OC. Despite a negligible contribution to DRE, the inclusion of BrC absorption in the model offset the negative radiative effect of OC by 0.11 W $m^{-2}$ (16%).

Optical/physical properties of aerosols and their effects on the Mie

calculation were also investigated. I examined the sensitivity of SSA calculation to physical properties of absorbing aerosols: BC, brown carbon (BrC), and dust. The base model with external mixing was successful at reproducing the observed variability of both $PM_{2.5}$ and AOD ($R \sim 0.76$), although the model underestimated their magnitudes by about 20%. I found that that physical parameters, which generally have received less attention than mass loadings, can bring about large uncertainties to DRF estimation. For example, if the geometric mean radius of BC was increased from 12 nm to 20 nm, BC absorption was increased by 11% when the geometric standard deviation is 1.6, but it is decreased by 5% when the geometric standard deviation is 2.0. The inclusion of BrC and size distribution of dust also significantly affected SSA, especially for 440 nm. I found the remarkable improvement for SSA at 440 nm when I considered BrC and observationally-constrained dust size distribution.

Finally, I examined the characteristics of OA during the KORUS-AQ campaign. I found that the observed OA showed high O:C ratio in comparison with previous aircraft campaigns. The observed OA during KORUS-AQ was strongly related with the acetonitrile concentration which has been known as biomass burning marker. High OA/BC ratio in this campaign also revealed the relationship between the observed OA and biomass burning emissions. I evaluated the model with recently proposed SOA schemes from Pye et al. (2010), Jo et al. (2013), and Hodzic et al. (2016). I found that the model with Jo et al. (2013) relatively well

represented the observed OA mass concentrations, but the result was significantly changed for some flight observations. I found that the model underestimated the observed OA by two times when the OA is heavily affected by biomass burning because of the underestimation of biomass burning emissions. On the other hand, the model overestimated the observed OA by two times if the model does not account photolytic loss of OA which should be considered in models.

# Bibliography

Aggarwal, S. G. and Kawamura, K.: Carbonaceous and inorganic composition in long-range transported aerosols over northern Japan: Implication for aging of water-soluble organic fraction, Atmospheric Environment, 43, 2532-2540, 2009.

Aiken, A.: Mexico City aerosol analysis during MILAGRO using high resolution aerosol mass spectrometry at the urban supersite(T 0)- Part 1: Fine particle composition and organic source apportionment, Atmospheric Chemistry and Physics, 9, 6633-6653, 2009.

Aiken, A. C., DeCarlo, P. F., Kroll, J. H., Worsnop, D. R., Huffman, J. A., Docherty, K. S., Ulbrich, I. M., Mohr, C., Kimmel, J. R., and Sueper, D.: O/C and OM/OC ratios of primary, secondary, and ambient organic aerosols with high-resolution time-of-flight aerosol mass spectrometry, Environmental Science & Technology, 42, 4478-4485, 2008.

Akagi, S., Yokelson, R., Wiedinmyer, C., Alvarado, M., Reid, J., Karl, T., Crounse, J., and Wennberg, P.: Emission factors for open and domestic biomass burning for use in atmospheric models, Atmospheric Chemistry and Physics, 11, 4039-4072, 2011.

Alexander, B., Park, R. J., Jacob, D. J., Li, Q., Yantosca, R. M., Savarino, J., Lee, C., and Thiemens, M.: Sulfate formation in sea□salt aerosols: Constraints from oxygen isotopes, Journal of Geophysical Research: Atmospheres (1984–2012), 110, 2005.

Alexander, D. T. L., Crozier, P. A., and Anderson, J. R.: Brown carbon spheres in East Asian outflow and their optical properties, Science, 321, 833, 2008.

Andreae, M. and Gelencser, A.: Black carbon or brown carbon? The nature of light-absorbing carbonaceous aerosols, Atmospheric Chemistry and Physics, 6, 3131-3148, 2006.

Andreae, M. O. and Merlet, P.: Emission of trace gases and aerosols from biomass burning, Global Biogeochemical Cycles, 15, 955-966, 2001.

Bahadur, R., Praveen, P. S., Xu, Y., and Ramanathan, V.: Solar absorption by elemental and brown carbon determined from spectral observations, Proceedings of the National Academy of Sciences, 109, 17366-17371, 2012.

Batmunkh, T., Kim, Y., Lee, K., Cayetano, M., Jung, J., Kim, S., Kim, K., Lee, S., Kim, J., and Chang, L.: Time-Resolved Measurements of PM2.

5 Carbonaceous Aerosols at Gosan, Korea, Journal of the Air & Waste Management Association, 61, 1174-1182, 2011.

Bergstrom, R., der Gon, H. v., Prévôt, A., Yttri, K., and Simpson, D.: Modelling of organic aerosols over Europe(2002-2007) using a volatility basis set(VBS) framework: application of different assumptions regarding the formation of secondary organic aerosol, Atmospheric Chemistry and Physics, 12, 8499-8527, 2012.

Bey, I., Jacob, D. J., Yantosca, R. M., and Logan, J. A.: Global modeling of tropospheric chemistry with assimilated meteorology- Model description and evaluation, Journal of Geophysical Research, 106, 073-023,095, 2001.

Birch, M. and Cary, R.: Elemental carbon-based method for monitoring occupational exposures to particulate diesel exhaust, Aerosol Science and Technology, 25, 221-241, 1996.

Bond, T. C. and Bergstrom, R. W.: Light absorption by carbonaceous particles: An investigative review, Aerosol Science and Technology, 40, 27-67, 2006.

Bond, T. C., Bhardwaj, E., Dong, R., Jogani, R., Jung, S., Roden, C., Streets, D. G., and Trautmann, N. M.: Historical emissions of black and organic carbon aerosol from energy-related combustion, 1850-2000, Global Biogeochemical Cycles, 21, 2007.

Bond, T. C., Doherty, S. J., Fahey, D. W., Forster, P. M., Berntsen, T., DeAngelo, B. J., Flanner, M. G., Ghan, S., Kärcher, B., Koch, D., Kinne, S., Kondo, Y., Quinn, P. K., Sarofim, M. C., Schultz, M. G., Schulz, M., Venkataraman, C., Zhang, H., Zhang, S., Bellouin, N., Guttikunda, S. K., Hopke, P. K., Jacobson, M. Z., Kaiser, J. W., Klimont, Z., Lohmann, U., Schwarz, J. P., Shindell, D., Storelvmo, T., Warren, S. G., and Zender, C. S.: Bounding the role of black carbon in the climate system: A scientific assessment, Journal of Geophysical Research, doi: 10.1002/jgrd.50171, 2013. n/a-n/a, 2013.

Bond, T. C., Habib, G., and Bergstrom, R. W.: Limitations in the enhancement of visible light absorption due to mixing state, Journal of Geophysical Research: Atmospheres (1984–2012), 111, 2006.

Bond, T. C., Streets, D. G., Yarber, K. F., Nelson, S. M., Woo, J. H., and Klimont, Z.: A technology-based global inventory of black and organic carbon emissions from combustion, Journal of Geophysical Research, 109, 14203, 2004.

Bones, D. L., Henricksen, D. K., Mang, S. A., Gonsior, M., Bateman, A. P., Nguyen, T. B., Cooper, W. J., and Nizkorodov, S. A.: Appearance of strong absorbers and fluorophores in limonene-O3 secondary organic aerosol due to NH4+-mediated chemical aging over long time scales,

Journal of Geophysical Research, 115, D05203, 2010.

Canagaratna, M., Jayne, J., Jimenez, J., Allan, J., Alfarra, M., Zhang, Q., Onasch, T., Drewnick, F., Coe, H., and Middlebrook, A.: Chemical and microphysical characterization of ambient aerosols with the aerodyne aerosol mass spectrometer, Mass Spectrometry Reviews, 26, 185-222, 2007.

Canagaratna, M., Jimenez, J., Kroll, J., Chen, Q., Kessler, S., Massoli, P., Hildebrandt Ruiz, L., Fortner, E., Williams, L., and Wilson, K.: Elemental ratio measurements of organic compounds using aerosol mass spectrometry: characterization, improved calibration, and implications, Atmospheric Chemistry and Physics, 15, 253-272, 2015.

Carlton, A. G., Turpin, B. J., Altieri, K. E., Seitzinger, S. P., Mathur, R., Roselle, S. J., and Weber, R. J.: CMAQ model performance enhanced when in-cloud secondary organic aerosol is included: Comparisons of organic carbon predictions with measurements, Environmental science & technology, 42, 8798-8802, 2008.

Chakrabarty, R., Moosmüller, H., Chen, L. W. A., Lewis, K., Arnott, W., Mazzoleni, C., Dubey, M., Wold, C., Hao, W., and Kreidenweis, S.: Brown carbon in tar balls from smoldering biomass combustion, Atmospheric Chemistry and Physics, 10, 6363-6370, 2010.

Chakrabarty, R. K., Pervez, S., Chow, J. C., Watson, J. G., Dewangan, S., Robles, J., and Tian, G.: Funeral pyres in South Asia: Brown carbon aerosol emissions and climate impacts, Environmental Science & Technology Letters, 1, 44-48, 2014.

Cheng, Y., He, K. B., Zheng, M., Duan, F. K., Du, Z. Y., Ma, Y. L., Tan, J. H., Yang, F. M., Liu, J. M., and Zhang, X. L.: Mass absorption efficiency of elemental carbon and water-soluble organic carbon in Beijing, China, Atmospheric Chemistry and Physics, 11, 11497-11510, 2011.

Chin, M., Diehl, T., Dubovik, O., Eck, T., Holben, B., Sinyuk, A., and Streets, D.: Light absorption by pollution, dust, and biomass burning aerosols: a global model study and evaluation with AERONET measurements, Annales Geophysicae, 27, 3439-3464, 2009.

Chin, M., Ginoux, P., Kinne, S., Torres, O., Holben, B. N., Duncan, B. N., Martin, R. V., Logan, J. A., Higurashi, A., and Nakajima, T.: Tropospheric Aerosol Optical Thickness from the GOCART Model and Comparisons with Satellite and Sun Photometer Measurements, Journal of Atmospheric Sciences, 59, 461-483, 2002.

Cho, S. Y. and Park, S. S.: Resolving sources of water-soluble organic carbon in fine particulate matter measured at an urban site during winter, Environmental Science: Processes & Impacts, 15, 524-534,

2013.

Choi, J.-K., Heo, J.-B., Ban, S.-J., Yi, S.-M., and Zoh, K.-D.: Chemical characteristics of PM< sub> 2.5</sub> aerosol in Incheon, Korea, Atmospheric Environment, 2012. 2012.

Chow, J. C., Watson, J. G., Pritchett, L. C., Pierson, W. R., Frazier, C. A., and Purcell, R. G.: The DRI thermal/optical reflectance carbon analysis system: description, evaluation and applications in US air quality studies, Atmospheric Environment, 27, 1185-1201, 1993.

Chung, C., Kim, S. W., Lee, M., Yoon, S. C., and Lee, S.: Carbonaceous aerosol AAE inferred from in-situ aerosol measurements at the Gosan ABC super site, and the implications for brown carbon aerosol, Atmospheric Chemistry and Physics, 12, 6173-6184, 2012.

Chung, S. and Seinfeld, J.: Global distribution and climate forcing of carbonaceous aerosols, Journal of Geophysical Research, 107, 4407, 2002.

Clarke, A., McNaughton, C., Kapustin, V., Shinozuka, Y., Howell, S., Dibb, J., Zhou, J., Anderson, B., Brekhovskikh, V., and Turner, H.: Biomass burning and pollution aerosol over North America: Organic components and their influence on spectral optical properties and humidification response, Journal of Geophysical Research, 112, D12S18, 2007.

Cohen, J. B. and Wang, C.: Estimating global black carbon emissions using a top□down Kalman Filter approach, Journal of Geophysical Research: Atmospheres, 119, 307-323, 2014.

Cooke, W., Liousse, C., Cachier, H., and Feichter, J.: Construction of a 1 x 1 fossil fuel emission data set for carbonaceous aerosol and implementation and radiative impact in the ECHAM4 model, Journal of Geophysical Research, 104, 22137-22162, 1999.

Curci, G., Hogrefe, C., Bianconi, R., Im, U., Balzarini, A., Baró, R., Brunner, D., Forkel, R., Giordano, L., Hirtl, M., Honzak, L., Jiménez-Guerrero, P., Knote, C., Langer, M., Makar, P. A., Pirovano, G., Pérez, J. L., San José, R., Syrakov, D., Tuccella, P., Werhahn, J., Wolke, R., Žabkar, R., Zhang, J., and Galmarini, S.: Uncertainties of simulated aerosol optical properties induced by assumptions on aerosol physical and chemical properties: An AQMEII-2 perspective, Atmospheric Environment, 115, 541-552, 2015.

Curier, R., Kranenburg, R., Segers, A., Timmermans, R., and Schaap, M.: Synergistic use of OMI NO 2 tropospheric columns and LOTOS–EUROS to evaluate the NO x emission trends across Europe, Remote Sensing of Environment, 149, 58-69, 2014.

Dai, T., Shi, G., and Nakajima, T.: Analysis and evaluation of the global aerosol optical properties simulated by an online aerosol-coupled non-hydrostatic icosahedral atmospheric model, Advances in Atmospheric Sciences, 32, 743-758, 2015.

Denjean, C., Formenti, P., Picquet-Varrault, B., Camredon, M., Pangui, E., Zapf, P., Katrib, Y., Giorio, C., Tapparo, A., Temime-Roussel, B., Monod, A., Aumont, B., and Doussin, J. F.: Aging of secondary organic aerosol generated from the ozonolysis of α-pinene: effects of ozone, light and temperature, Atmos. Chem. Phys., 15, 883-897, 2015.

Diehl, T., Heil, A., Chin, M., Pan, X., Streets, D., Schultz, M., and Kinne, S.: Anthropogenic, biomass burning, and volcanic emissions of black carbon, organic carbon, and SO2 from 1980 to 2010 for hindcast model experiments, Atmospheric Chemistry and Physics Discussions, 12, 24895-24954, 2012.

Dommen, J., Metzger, A., Duplissy, J., Kalberer, M., Alfarra, M., Gascho, A., Weingartner, E., Prevot, A., Verheggen, B., and Baltensperger, U.: Laboratory observation of oligomers in the aerosol from isoprene/NOx photooxidation, Geophysical Research Letters, 33, 2006.

Donahue, N., Epstein, S., Pandis, S., and Robinson, A.: A two-dimensional volatility basis set: 1. organic-aerosol mixing thermodynamics, Atmospheric Chemistry and Physics, 11, 3303-3318, 2011.

Donahue, N., Kroll, J., Pandis, S., and Robinson, A.: A two-dimensional volatility basis set-Part 2: Diagnostics of organic-aerosol evolution, Atmospheric Chemistry and Physics, 12, 615-634, 2012a.

Donahue, N., Robinson, A., Stanier, C., and Pandis, S.: Coupled partitioning, dilution, and chemical aging of semivolatile organics, Environmental Science & Technology, 40, 2635-2643, 2006.

Donahue, N. M., Henry, K. M., Mentel, T. F., Kiendler-Scharr, A., Spindler, C., Bohn, B., Brauers, T., Dorn, H. P., Fuchs, H., and Tillmann, R.: Aging of biogenic secondary organic aerosol via gas-phase OH radical reactions, Proceedings of the National Academy of Sciences, 109, 13503-13508, 2012b.

Drury, E., Jacob, D. J., Spurr, R. J., Wang, J., Shinozuka, Y., Anderson, B. E., Clarke, A. D., Dibb, J., McNaughton, C., and Weber, R.: Synthesis of satellite (MODIS), aircraft (ICARTT), and surface (IMPROVE, EPA□ AQS, AERONET) aerosol observations over eastern North America to improve MODIS aerosol retrievals and constrain surface aerosol concentrations and sources, Journal of Geophysical Research: Atmospheres (1984–2012), 115, 2010.

Dzepina, K., Volkamer, R., Madronich, S., Tulet, P., Ulbrich, I., Zhang, Q., Cappa, C., Ziemann, P., and Jimenez, J.: Evaluation of recently-

proposed secondary organic aerosol models for a case study in Mexico City, Atmospheric Chemistry and Physics, 9, 5681-5709, 2009.

Eidels-Dubovoi, S.: Aerosol impacts on visible light extinction in the atmosphere of Mexico City, The Science of the Total Environment, 287, 213-220, 2002.

Fairlie, T., Jacob, D., Dibb, J., Alexander, B., Avery, M., van Donkelaar, A., and Zhang, L.: Impact of mineral dust on nitrate, sulfate, and ozone in transpacific Asian pollution plumes, Atmospheric Chemistry and Physics, 10, 3999-4012, 2010.

Fairlie, T. D., Jacob, D. J., and Park, R. J.: The impact of transpacific transport of mineral dust in the United States, Atmospheric Environment, 41, 1251-1266, 2007.

Farias, T. L., Köylü, Ü. Ö., and Carvalho, M. d. G.: Range of validity of the Rayleigh–Debye–Gans theory for optics of fractal aggregates, Applied Optics, 35, 6560-6567, 1996.

Farina, S. C., Adams, P. J., and Pandis, S. N.: Modeling global secondary organic aerosol formation and processing with the volatility basis set: Implications for anthropogenic secondary organic aerosol, Journal of Geophysical Research, 115, D09202, 2010.

Favez, O., Alfaro, S. C., Sciare, J., Cachier, H., and Abdelwahab, M. M.: Ambient measurements of light-absorption by agricultural waste burning organic aerosols, Journal of Aerosol Science, 40, 613-620, 2009.

Feng, J., Hu, M., Chan, C. K., Lau, P., Fang, M., He, L., and Tang, X.: A comparative study of the organic matter in PM< sub> 2.5</sub> from three Chinese megacities in three different climatic zones, Atmospheric Environment, 40, 3983-3994, 2006.

Feng, Y., Ramanathan, V., and Kotamarthi, V.: Brown carbon: a significant atmospheric absorber of solar radiation?, Atmospheric Chemistry and Physics, 13, 8607-8621, 2013.

Fernandes, S. D., Trautmann, N. M., Streets, D. G., Roden, C. A., and Bond, T. C.: Global biofuel use, 1850–2000, Global Biogeochemical Cycles, 21, GB2019, 2007.

Flores, J. M., Washenfelder, R., Adler, G., Lee, H., Segev, L., Laskin, J., Laskin, A., Nizkorodov, S., Brown, S., and Rudich, Y.: Complex refractive indices in the near-ultraviolet spectral region of biogenic secondary organic aerosol aged with ammonia, Physical Chemistry Chemical Physics, 16, 10629-10642, 2014.

Folinsbee, L. J.: Human health effects of air pollution, Environmental health perspectives, 100, 45, 1993.

Forster, P., V. , Ramaswamy, P., Artaxo, T., Berntsen, R., Betts, D. W., Fahey, J., Haywood, J., Lean, D. C., Lowe, G., Myhre, J., Nganga, R., Prinn, G., Raga, M. S., and Dorland, R. V.: Changes in Atmospheric Constituents and in Radiative Forcing., Cambridge University Press, United Kingdom and New York, NY, USA., 2007.

Fountoukis, C. and Nenes, A.: ISORROPIA II: a computationally efficient thermodynamic equilibrium model for K+-Ca2+-Mg2+-NH4+-Na+-SO42--NO3--Cl--H2O aerosols, Atmospheric Chemistry and Physics Discussions, 7, 1893-1939, 2007.

Fu, T. M., Jacob, D. J., Wittrock, F., Burrows, J. P., Vrekoussis, M., and Henze, D. K.: Global budgets of atmospheric glyoxal and methylglyoxal, and implications for formation of secondary organic aerosols, Journal of Geophysical Research, 113, 2008.

Giglio, L., Randerson, J. T., and Werf, G. R.: Analysis of daily, monthly, and annual burned area using the fourth□generation global fire emissions database (GFED4), Journal of Geophysical Research: Biogeosciences, 118, 317-328, 2013.

Ginoux, P., Chin, M., Tegen, I., Prospero, J. M., Holben, B., Dubovik, O., and Lin, S. J.: Sources and distributions of dust aerosols simulated with the GOCART model, Journal of Geophysical Research: Atmospheres (1984–2012), 106, 20255-20273, 2001.

Goldstein, A. H. and Galbally, I. E.: Known and unexplored organic constituents in the earth's atmosphere, Environmental Science & Technology, 41, 1514-1521, 2007.

Graber, E. and Rudich, Y.: Atmospheric HULIS: How humic-like are they? A comprehensive and critical review, Atmospheric Chemistry and Physics, 6, 729-753, 2006.

Granier, C., Bessagnet, B., Bond, T., D'Angiola, A., Denier van der Gon, H., Frost, G. J., Heil, A., Kaiser, J. W., Kinne, S., and Klimont, Z.: Evolution of anthropogenic and biomass burning emissions of air pollutants at global and regional scales during the 1980–2010 period, Climatic Change, 109, 163-190, 2011.

Grieshop, A., Logue, J., Donahue, N., and Robinson, A.: Laboratory investigation of photochemical oxidation of organic aerosol from wood fires 1: measurement and simulation of organic aerosol evolution, Atmospheric Chemistry and Physics, 9, 2009.

Griffin, R., Flagan, R., and Seinfeld, J.: Organic aerosol formation from the oxidation of biogenic hydrocarbons, Journal of Geophysical Research, 104, 3555-3567, 1999.

Gu, Y. and Liao, H.: Summertime nitrate aerosol in the upper troposphere

and lower stratosphere over the Tibetan Plateau and the South Asian summer monsoon region, Atmospheric Chemistry and Physics Discussions, 15, 32049-32099, 2015.

Guenther, A., Jiang, X., Heald, C., Sakulyanontvittaya, T., Duhl, T., Emmons, L., and Wang, X.: The Model of Emissions of Gases and Aerosols from Nature version 2.1 (MEGAN2. 1): an extended and updated framework for modeling biogenic emissions, Geoscientific Model Development, 5, 1471-1492, 2012.

Hallquist, M., Wenger, J., Baltensperger, U., Rudich, Y., Simpson, D., Claeys, M., Dommen, J., Donahue, N., George, C., and Goldstein, A.: The formation, properties and impact of secondary organic aerosol: current and emerging issues, Atmospheric Chemistry and Physics, 9, 5155, 2009.

Hawkins, L. N., Baril, M. J., Sedehi, N., Galloway, M. M., De Haan, D. O., Schill, G. P., and Tolbert, M. A.: Formation of Semisolid, Oligomerized Aqueous SOA: Lab Simulations of Cloud Processing, Environmental science & technology, 48, 2273-2280, 2014.

Heald, C., Collett Jr, J., Lee, T., Benedict, K., Schwandner, F., Li, Y., Clarisse, L., Hurtmans, D., Van Damme, M., and Clerbaux, C.: Atmospheric ammonia and particulate inorganic nitrogen over the United States, Atmospheric Chemistry and Physics Discussions, 12, 19455-19498, 2012.

Heald, C., Jacob, D., Park, R., Russell, L., Huebert, B., Seinfeld, J., Liao, H., and Weber, R.: A large organic aerosol source in the free troposphere missing from current models, Geophysical Research Letters, 32, L18809, 2005.

Heald, C., Kroll, J., Jimenez, J., Docherty, K., DeCarlo, P., Aiken, A., Chen, Q., Martin, S., Farmer, D., and Artaxo, P.: A simplified description of the evolution of organic aerosol composition in the atmosphere, Geophysical Research Letters, 37, 2010a.

Heald, C., Ridley, D., Kroll, J., Barrett, S., Cady-Pereira, K., Alvarado, M., and Holmes, C.: Contrasting the direct radiative effect and direct radiative forcing of aerosols, Atmospheric Chemistry and Physics, 14, 5513-5527, 2014.

Heald, C. L., Coe, H., Jimenez, J. L., Weber, R. J., Bahreini, R., Middlebrook, A. M., Russell, L. M., Jolleys, M., Fu, T. M., Allan, J. D., Bower, K. N., Capes, G., Crosier, J., Morgan, W. T., Robinson, N. H., Williams, P. I., Cubison, M. J., DeCarlo, P. F., and Dunlea, E. J.: Exploring the vertical profile of atmospheric organic aerosol: comparing 17 aircraft field campaigns with a global model, Atmospheric Chemistry and Physics., 11, 12673-12696, 2011.

Heald, C. L., Ridley, D. A., Kreidenweis, S. M., and Drury, E. E.: Satellite observations cap the atmospheric organic aerosol budget, Geophysical Research Letters, 37, 2010b.

Hecobian, A., Zhang, X., Zheng, M., Frank, N., Edgerton, E., and Weber, R.: Water-Soluble Organic Aerosol material and the light-absorption characteristics of aqueous extracts measured over the Southeastern United States, Atmospheric Chemistry and Physics, 10, 5965-5977, 2010.

Henze, D. K. and Seinfeld, J. H.: Global secondary organic aerosol from isoprene oxidation, Geophysical Research Letters, 33, 09812, 2006.

Henze, D. K., Seinfeld, J. H., Ng, N. L., Kroll, J. H., Jacob, D. J., and Heald, C. L.: Global modeling of secondary organic aerosol formation from aromatic hydrocarbons: high-vs. low-yield pathways, Atmospheric Chemistry and Physics, 8, 2405-2420, 2008.

Hess, M., Koepke, P., and Schult, I.: Optical properties of aerosols and clouds: The software package OPAC, Bulletin of the American meteorological society, 79, 831-844, 1998.

Hirsch, R. and Gilroy, E.: Methods of Fitting a Straight Line to Data: Examples in Water Resources, Water Resources Bulletin, 20, 1984.

Hodzic, A., Kasibhatla, P. S., Jo, D. S., Cappa, C. D., Jimenez, J. L., Madronich, S., and Park, R. J.: Rethinking the global secondary organic aerosol (SOA) budget: stronger production, faster removal, shorter lifetime, Atmospheric Chemistry and Physics, 16, 7917-7941, 2016.

Hodzic, A., Madronich, S., Kasibhatla, P., Tyndall, G., Aumont, B., Jimenez, J., Lee-Taylor, J., and Orlando, J.: Organic photolysis reactions in tropospheric aerosols: effect on secondary organic aerosol formation and lifetime, Atmospheric Chemistry and Physics, 15, 9253-9269, 2015.

Hoffer, A., Gelencsér, A., Guyon, P., Kiss, G., Schmid, O., Frank, G., Artaxo, P., and Andreae, M.: Optical properties of humic-like substances (HULIS) in biomass-burning aerosols, Atmospheric Chemistry and Physics, 6, 3563-3570, 2006.

Huang, Y., Wu, S., Dubey, M., and French, N.: Impact of aging mechanism on model simulated carbonaceous aerosols, Atmospheric Chemistry and Physics, 13, 6329-6343, 2013.

Hudman, R. C., Jacob, D. J., Turquety, S., Leibensperger, E. M., Murray, L. T., Wu, S., Gilliland, A., Avery, M., Bertram, T. H., and Brune, W.: Surface and lightning sources of nitrogen oxides over the United States: Magnitudes, chemical evolution, and outflow, Journal of Geophysical Research, 112, D12S05, 2007.

Iacono, M. J., Delamere, J. S., Mlawer, E. J., Shephard, M. W., Clough, S. A., and Collins, W. D.: Radiative forcing by long□lived greenhouse gases: Calculations with the AER radiative transfer models, Journal of Geophysical Research: Atmospheres (1984–2012), 113, 2008.

Jacobson, M. Z.: Global direct radiative forcing due to multicomponent anthropogenic and natural aerosols, Journal of Geophysical Research, 106, 1551-1568, 2001.

Jacobson, M. Z.: Isolating nitrated and aromatic aerosols and nitrated aromatic gases as sources of ultraviolet light absorption, Journal of Geophysical Research, 104, 3527-3542, 1999.

Jaeglé, L., Quinn, P., Bates, T., Alexander, B., and Lin, J.-T.: Global distribution of sea salt aerosols: new constraints from in situ and remote sensing observations, Atmospheric Chemistry and Physics, 11, 3137-3157, 2011.

Janssens-Maenhout, G., Crippa, M., Guizzardi, D., Dentener, F., Muntean, M., Pouliot, G., Keating, T., Zhang, Q., Kurokawa, J., and Wankmüller, R.: HTAP_v2. 2: a mosaic of regional and global emission grid maps for 2008 and 2010 to study hemispheric transport of air pollution, Atmospheric Chemistry and Physics, 15, 11411-11432, 2015.

Jaoui, M., Edney, E. O., Kleindienst, T. E., Lewandowski, M., Offenberg, J. H., Surratt, J. D., and Seinfeld, J. H.: Formation of secondary organic aerosol from irradiated ¥á-pinene/toluene/NOx mixtures and the effect of isoprene and sulfur dioxide, Journal of Geophysical Research, 113, D09303, 2008.

Jathar, S., Farina, S., Robinson, A., and Adams, P.: The influence of semi-volatile and reactive primary emissions on the abundance and properties of global organic aerosol, Atmospheric Chemistry and Physics Discussions, 11, 5493-5540, 2011.

Jathar, S. H., Gordon, T. D., Hennigan, C. J., Pye, H. O., Pouliot, G., Adams, P. J., Donahue, N. M., and Robinson, A. L.: Unspeciated organic emissions from combustion sources and their influence on the secondary organic aerosol budget in the United States, Proceedings of the National Academy of Sciences, 111, 10473-10478, 2014.

Jeong, J., Park, R., Woo, J., Han, Y., and Yi, S.: Source contributions to carbonaceous aerosol concentrations in Korea, Atmospheric Environment, 2010. 2010.

Jethva, H., Torres, O., and Ahn, C.: Global assessment of OMI aerosol single□scattering albedo using ground□based AERONET inversion, Journal of Geophysical Research: Atmospheres, 119, 9020-9040, 2014.

Jimenez, J., Canagaratna, M., Donahue, N., Prevot, A., Zhang, Q., Kroll, J.,

DeCarlo, P., Allan, J., Coe, H., and Ng, N.: Evolution of organic aerosols in the atmosphere, Science, 326, 1525, 2009.

Jo, D., Park, R., Kim, M., and Spracklen, D.: Effects of chemical aging on global secondary organic aerosol using the volatility basis set approach, Atmospheric Environment, 81, 230-244, 2013.

Jo, D. S., Park, R. J., Lee, S., Kim, S. W., and Zhang, X.: A global simulation of brown carbon: implications for photochemistry and direct radiative effect, Atmospheric Chemistry and Physics, 16, 3413-3432, 2016.

Jordan, C., Dibb, J., Anderson, B., and Fuelberg, H.: Uptake of nitrate and sulfate on dust aerosols during TRACE-P, Journal of Geophysical Research, 108, 8817, 2003.

Kanakidou, M., Seinfeld, J., Pandis, S., Barnes, I., Dentener, F., Facchini, M., Van Dingenen, R., Ervens, B., Nenes, A., and Nielsen, C.: Organic aerosol and global climate modelling: a review, Atmospheric Chemistry and Physics, 5, 1053-1123, 2005.

Kaufman, Y. J., Justice, C. O., Flynn, L. P., Kendall, J. D., Prins, E. M., Giglio, L., Ward, D. E., Menzel, W. P., and Setzer, A. W.: Potential global fire monitoring from EOS-MODIS, Journal of Geophysical Research, 103, 32215-32238, 1998.

Khatri, P., Takamura, T., Shimizu, A., and Sugimoto, N.: Observation of low single scattering albedo of aerosols in the downwind of the East Asian desert and urban areas during the inflow of dust aerosols, Journal of Geophysical Research: Atmospheres, 119, 787-802, 2014.

Kim, H. and Paulson, S.: Real refractive indices and volatility of secondary organic aerosol generated from photooxidation and ozonolysis of limonene, α-pinene and toluene, Atmospheric Chemistry and Physics Discussions, 13, 2013.

Kirchstetter, T. and Thatcher, T.: Contribution of organic carbon to wood smoke particulate matter absorption of solar radiation, Atmospheric Chemistry and Physics, 12, 6067-6072, 2012.

Kirchstetter, T. W., Novakov, T., and Hobbs, P. V.: Evidence that the spectral dependence of light absorption by aerosols is affected by organic carbon, Journal of Geophysical Research, 109, D21208, 2004.

Kleindienst, T. E., Lewandowski, M., Offenberg, J. H., Jaoui, M., and Edney, E. O.: Ozone□isoprene reaction: Re□examination of the formation of secondary organic aerosol, Geophysical research letters, 34, 2007.

Koch, D., Schulz, M., Kinne, S., McNaughton, C., Spackman, J., Balkanski, Y., Bauer, S., Berntsen, T., Bond, T. C., and Boucher, O.: Evaluation of black carbon estimations in global aerosol models, Atmospheric

Chemistry and Physics, 9, 9001-9026, 2009.

Kok, J. F.: A scaling theory for the size distribution of emitted dust aerosols suggests climate models underestimate the size of the global dust cycle, Proceedings of the National Academy of Sciences, 108, 1016-1021, 2011.

Kok, J. F., Ridley, D. A., Zhou, Q., Miller, R. L., Zhao, C., Heald, C. L., Ward, D. S., Albani, S., and Haustein, K.: Smaller desert dust cooling effect estimated from analysis of dust size and abundance, Nature Geoscience, 2017. 2017.

Koo, B., Knipping, E., and Yarwood, G.: 1.5-Dimensional volatility basis set approach for modeling organic aerosol in CAMx and CMAQ, Atmospheric Environment, 95, 158-164, 2014.

Kroll, J. and Seinfeld, J.: Chemistry of secondary organic aerosol: Formation and evolution of low-volatility organics in the atmosphere, Atmospheric Environment, 42, 3593-3624, 2008.

Kroll, J. H., Ng, N. L., Murphy, S. M., Flagan, R. C., and Seinfeld, J. H.: Secondary organic aerosol formation from isoprene photooxidation, Environmental science & technology, 40, 1869-1877, 2006.

Kroll, J. H., Ng, N. L., Murphy, S. M., Flagan, R. C., and Seinfeld, J. H.: Secondary organic aerosol formation from isoprene photooxidation under high-NOx conditions, Geophysical Research Letters, 32, L18808, 2005.

Lacagnina, C., Hasekamp, O. P., Bian, H., Curci, G., Myhre, G., Noije, T., Schulz, M., Skeie, R. B., Takemura, T., and Zhang, K.: Aerosol single□ scattering albedo over the global oceans: Comparing PARASOL retrievals with AERONET, OMI, and AeroCom models estimates, Journal of Geophysical Research: Atmospheres, 120, 9814-9836, 2015.

Lamarque, J., Bond, T., Eyring, V., Granier, C., Heil, A., Klimont, Z., Lee, D., Mieville, A., and Owen, B.: Historical(1850-2000) gridded anthropogenic and biomass burning emissions of reactive gases and aerosols: methodology and application, Atmospheric Chemistry and Physics, 10, 7017-7039, 2010.

Lambe, A. T., Cappa, C. D., Massoli, P., Onasch, T., Forestieri, S. D., Martin, A. T., Cummings, M. J., Croasdale, D. R., Brune, B., and Worsnop, D. R.: Relationship between oxidation level and optical properties of secondary organic aerosol, Environmental science & technology, 47, 6349-6357, 2013.

Lane, T., Donahue, N., and Pandis, S.: Simulating secondary organic aerosol formation using the volatility basis-set approach in a chemical transport model, Atmospheric Environment, 42, 7439-7451, 2008.

Lanz, V., Alfarra, M., Baltensperger, U., Buchmann, B., Hueglin, C., and Prévôt, A.: Source apportionment of submicron organic aerosols at an urban site by factor analytical modelling of aerosol mass spectra, Atmospheric Chemistry and Physics, 7, 1503-1522, 2007.

Laskin, A., Laskin, J., and Nizkorodov, S. A.: Chemistry of Atmospheric Brown Carbon, Chemical reviews, 115, 4335-4382, 2015.

Laskin, J., Laskin, A., Nizkorodov, S. A., Roach, P., Eckert, P., Gilles, M. K., Wang, B., Lee, H. J., and Hu, Q.: Molecular Selectivity of Brown Carbon Chromophores, Environmental science & technology, 48, 12047-12055, 2014.

Laskin, J., Laskin, A., Roach, P. J., Slysz, G. W., Anderson, G. A., Nizkorodov, S. A., Bones, D. L., and Nguyen, L. Q.: High-resolution desorption electrospray ionization mass spectrometry for chemical characterization of organic aerosols, Analytical chemistry, 82, 2048-2058, 2010.

Li, L., Wang, W., Feng, J., Zhang, D., Li, H., Gu, Z., Wang, B., Sheng, G., and Fu, J.: Composition, source, mass closure of PM< sub> 2.5</sub> aerosols for four forests in eastern China, Journal of Environmental Sciences, 22, 405-412, 2010.

Liao, H., Henze, D., Seinfeld, J., Wu, S., and Mickley, L.: Biogenic secondary organic aerosol over the United States: Comparison of climatological simulations with observations, Journal of Geophysical Research, 112, D06201, 2007.

Liggio, J., Li, S. M., and McLaren, R.: Reactive uptake of glyoxal by particulate matter, Journal of Geophysical Research, 110, 2005.

Lin, G., Penner, J. E., Flanner, M. G., Sillman, S., Xu, L., and Zhou, C.: Radiative forcing of organic aerosol in the atmosphere and on snow: Effects of SOA and brown carbon, Journal of Geophysical Research: Atmospheres, 119, 7453-7476, 2014.

Lin, J.-T. and McElroy, M. B.: Impacts of boundary layer mixing on pollutant vertical profiles in the lower troposphere: Implications to satellite remote sensing, Atmospheric Environment, 44, 1726-1739, 2010.

Lin, P., Liu, J., Shilling, J. E., Kathmann, S. M., Laskin, J., and Laskin, A.: Molecular characterization of brown carbon (BrC) chromophores in secondary organic aerosol generated from photo-oxidation of toluene, Physical Chemistry Chemical Physics, 2015. 2015.

Liu, H., Jacob, D. J., Bey, I., and Yantosca, R. M.: Constraints from 210Pb and 7Be on wet deposition and transport in a global three-dimensional chemical tracer model driven by assimilated meteorological fields,

Journal of Geophysical Research, 106, 12109-12128, 2001.

Liu, J., Scheuer, E., Dibb, J., Ziemba, L. D., Thornhill, K., Anderson, B. E., Wisthaler, A., Mikoviny, T., Devi, J. J., and Bergin, M.: Brown carbon in the continental troposphere, Geophysical Research Letters, 41, 2191-2195, 2014.

Liu, S., Shilling, J. E., Song, C., Hiranuma, N., Zaveri, R. A., and Russell, L. M.: Hydrolysis of organonitrate functional groups in aerosol particles, Aerosol Science and Technology, 46, 1359-1369, 2012a.

Liu, Z., Wang, Y., Vrekoussis, M., Richter, A., Wittrock, F., Burrows, J. P., Shao, M., Chang, C. C., Liu, S. C., and Wang, H.: Exploring the missing source of glyoxal (CHOCHO) over China, Geophysical Research Letters, 39, 2012b.

Loeb, N. G. and Su, W.: Direct aerosol radiative forcing uncertainty based on a radiative perturbation analysis, Journal of Climate, 23, 5288-5293, 2010.

Lukács, H., Gelencsér, A., Hammer, S., Puxbaum, H., Pio, C., Legrand, M., Kasper-Giebl, A., Handler, M., Limbeck, A., and Simpson, D.: Seasonal trends and possible sources of brown carbon based on 2-year aerosol measurements at six sites in Europe, Journal of Geophysical Research, 112, 2007.

Mahowald, N., Albani, S., Kok, J. F., Engelstaeder, S., Scanza, R., Ward, D. S., and Flanner, M. G.: The size distribution of desert dust aerosols and its impact on the Earth system, Aeolian Research, 15, 53-71, 2014.

Malm, W. C., Sisler, J. F., Huffman, D., Eldred, R. A., and Cahill, T. A.: Spatial and seasonal trends in particle concentration and optical extinction in the United States, Journal of Geophysical Research, 99, 1347-1370, 1994.

Mari, C., Jacob, D. J., and Bechtold, P.: Transport and scavenging of soluble gases in a deep convective cloud, Journal of Geophysical Research, 105, 22255-22222,22267, 2000.

Martin, R. V., Jacob, D. J., Yantosca, R. M., Chin, M., and Ginoux, P.: Global and regional decreases in tropospheric oxidants from photochemical effects of aerosols, Journal of Geophysical Research, 108, 4097, 2003.

McComiskey, A., Schwartz, S. E., Schmid, B., Guan, H., Lewis, E. R., Ricchiazzi, P., and Ogren, J. A.: Direct aerosol forcing: Calculation from observables and sensitivities to inputs, Journal of Geophysical Research: Atmospheres, 113, 2008.

McMeeking, G. R.: The optical, chemical, and physical properties of aerosols and gases emitted by the laboratory combustion of wildland

fuels, Dissertation, 2008. 2008.

Ming, Y., Ramaswamy, V., Ginoux, P. A., and Horowitz, L. H.: Direct radiative forcing of anthropogenic organic aerosol, Journal of Geophysical Research, 110, 2005.

Mishchenko, M. I.: Electromagnetic scattering by nonspherical particles: A tutorial review, Journal of Quantitative Spectroscopy and Radiative Transfer, 110, 808-832, 2009.

Mishchenko, M. I., Travis, L. D., and Lacis, A. A.: Scattering, absorption, and emission of light by small particles, Cambridge university press, 2002.

Miyazaki, Y., Kondo, Y., Han, S., Koike, M., Kodama, D., Komazaki, Y., Tanimoto, H., and Matsueda, H.: Chemical characteristics of water□ soluble organic carbon in the Asian outflow, Journal of Geophysical Research, 112, 2007.

Moffet, R. C. and Prather, K. A.: In-situ measurements of the mixing state and optical properties of soot with implications for radiative forcing estimates, Proceedings of the National Academy of Sciences, 106, 11872-11877, 2009.

Moise, T., Flores, J. M., and Rudich, Y.: Optical Properties of Secondary Organic Aerosols and Their Changes by Chemical Processes, Chemical reviews, 115, 4400-4439, 2015.

Mu, M., Randerson, J., van der Werf, G., Giglio, L., Kasibhatla, P., Morton, D., Collatz, G., DeFries, R., Hyer, E., and Prins, E.: Daily and 3-hourly variability in global fire emissions and consequences for atmospheric model predictions of carbon monoxide, Journal of Geophysical Research, 116, 24303, 2011.

Murphy, B., Donahue, N., Fountoukis, C., Dall'Osto, M., O'Dowd, C., Kiendler-Scharr, A., and Pandis, S.: Functionalization and fragmentation during ambient organic aerosol aging: application of the 2-D volatility basis set to field studies, Atmospheric Chemistry and Physics, 12, 10797-10816, 2012.

Murphy, B., Donahue, N., Fountoukis, C., and Pandis, S.: Simulating the oxygen content of ambient organic aerosol with the 2D volatility basis set, Atmospheric Chemistry and Physics, 11, 7859-7873, 2011.

Murphy, B. N. and Pandis, S. N.: Exploring summertime organic aerosol formation in the eastern United States using a regional□scale budget approach and ambient measurements, Journal of Geophysical Research, 115, 2010.

Murphy, B. N. and Pandis, S. N.: Simulating the formation of semivolatile primary and secondary organic aerosol in a regional chemical transport

model, Environmental Science & Technology, 43, 4722-4728, 2009.

Myhre, G., Berglen, T., Johnsrud, M., Hoyle, C., Berntsen, T., Christopher, S., Fahey, D., Isaksen, I., Jones, T., and Kahn, R.: Modelled radiative forcing of the direct aerosol effect with multi-observation evaluation, Atmospheric Chemistry and Physics, 9, 1365-1392, 2009.

Myhre, G., D. Shindell, F.-M. Bréon, W. Collins, J. Fuglestvedt, J. Huang, D. Koch, J.-F. Lamarque, D. Lee, B. Mendoza, T. Nakajima, A. Robock, G. Stephens, Takemura, T., and Zhang, H.: Anthropogenic and Natural Radiative Forcing. In: Climate Change 2013: The Physical Science Basis. Contribution of Working Group I to the Fifth Assessment Report of the Intergovernmental Panel on Climate Change, Climate change, 2013a. 659-740, 2013a.

Myhre, G., Samset, B., Schulz, M., Balkanski, Y., Bauer, S., Berntsen, T., Bian, H., Bellouin, N., Chin, M., and Diehl, T.: Radiative forcing of the direct aerosol effect from AeroCom Phase II simulations, Atmospheric Chemistry and Physics, 13, 1853-1877, 2013b.

Nakayama, T., Matsumi, Y., Sato, K., Imamura, T., Yamazaki, A., and Uchiyama, A.: Laboratory studies on optical properties of secondary organic aerosols generated during the photooxidation of toluene and the ozonolysis of α-pinene, Journal of Geophysical Research, 115, D24204, 2010.

Nakayama, T., Sato, K., Matsumi, Y., Imamura, T., Yamazaki, A., and Uchiyama, A.: Wavelength and NO x dependent complex refractive index of SOAs generated from the photooxidation of toluene, Atmospheric Chemistry and Physics, 13, 531-545, 2013.

Napier, W., Ensberg, J., and Seinfeld, J.: Insight into the numerical challenges of implementing 2-dimensional SOA models in atmospheric chemical transport models, Atmospheric Environment, 96, 331-344, 2014.

Ng, N. L., Kroll, J. H., Keywood, M. D., Bahreini, R., Varutbangkul, V., Flagan, R. C., Seinfeld, J. H., Lee, A., and Goldstein, A. H.: Contribution of first-versus second-generation products to secondary organic aerosols formed in the oxidation of biogenic hydrocarbons, Environmental Science & Technology, 40, 2283-2297, 2006.

Nguyen, T. B., Lee, P. B., Updyke, K. M., Bones, D. L., Laskin, J., Laskin, A., and Nizkorodov, S. A.: Formation of nitrogen-and sulfur-containing light-absorbing compounds accelerated by evaporation of water from secondary organic aerosols, Journal of Geophysical Research, 117, 01207, 2012.

Odum, J., Hoffmann, T., Bowman, F., Collins, D., Flagan, R., and Seinfeld, J.: Gas/particle partitioning and secondary organic aerosol yields,

Environmental Science & Technology, 30, 2580-2585, 1996.

Oshima, N., Koike, M., Zhang, Y., Kondo, Y., Moteki, N., Takegawa, N., and Miyazaki, Y.: Aging of black carbon in outflow from anthropogenic sources using a mixing state resolved model: Model development and evaluation, Journal of Geophysical Research: Atmospheres, 114, 2009.

Pankow, J.: An absorption model of gas/particle partitioning of organic compounds in the atmosphere, Atmospheric Environment, 28, 185-188, 1994a.

Pankow, J. F.: An absorption model of the gas/aerosol partitioning involved in the formation of secondary organic aerosol, Atmospheric Environment, 28, 189-193, 1994b.

Park, R. J., Jacob, D. J., Chin, M., and Martin, R. V.: Sources of carbonaceous aerosols over the United States and implications for natural visibility, Journal of Geophysical Research, 108, 4355, 2003.

Park, R. J., Jacob, D. J., Field, B. D., Yantosca, R. M., and Chin, M.: Natural and transboundary pollution influences on sulfate-nitrate-ammonium aerosols in the United States: Implications for policy, Journal of Geophysical Research, 109, D15204, 2004.

Park, R. J., Jacob, D. J., Kumar, N., and Yantosca, R. M.: Regional visibility statistics in the United States: Natural and transboundary pollution influences, and implications for the Regional Haze Rule, Atmospheric Environment, 40, 5405-5423, 2006.

Park, R. J., Kim, M. J., Jeong, J. I., Youn, D., and Kim, S.: A contribution of brown carbon aerosol to the aerosol light absorption and its radiative forcing in East Asia, Atmospheric Environment, 44, 1414-1421, 2010.

Pathak, R. K., Wang, T., Ho, K., and Lee, S.: Characteristics of summertime PM< sub> 2.5</sub> organic and elemental carbon in four major Chinese cities: Implications of high acidity for water-soluble organic carbon (WSOC), Atmospheric Environment, 45, 318-325, 2011.

Pavia, D., Thomson, M. L., Clarke, S. W., and Shannon, H. S.: Effect of lung function and mode of inhalation on penetration of aerosol into the human lung, Thorax, 32, 194, 1977.

Pavuluri, C. M., Kawamura, K., Uchida, M., Kondo, M., and Fu, P.: Enhanced modern carbon and biogenic organic tracers in Northeast Asian aerosols during spring/summer, Journal of Geophysical Research: Atmospheres, 2013. 2013.

Pye, H., Chan, A., Barkley, M., and Seinfeld, J.: Global modeling of organic aerosol: the importance of reactive nitrogen (NO_x and NO_3), Atmospheric Chemistry and Physics, 10, 11261-11276, 2010.

Pye, H. and Seinfeld, J.: A global perspective on aerosol from low-volatility organic compounds, Atmospheric Chemistry and Physics, 10, 4377-4401, 2010.

Pye, H. O. T., Liao, H., Wu, S., Mickley, L. J., Jacob, D. J., Henze, D. J., and Seinfeld, J. H.: Effect of changes in climate and emissions on future sulfate-nitrate-ammonium aerosol levels in the United States, Journal of Geophysical Research, 114, 2009.

Reid, J., Koppmann, R., Eck, T., and Eleuterio, D.: A review of biomass burning emissions part II: intensive physical properties of biomass burning particles, Atmospheric Chemistry and Physics, 5, 799-825, 2005.

Rienecker, M. M., Suarez, M. J., Gelaro, R., Todling, R., Bacmeister, J., Liu, E., Bosilovich, M. G., Schubert, S. D., Takacs, L., and Kim, G.-K.: MERRA: NASA's modern-era retrospective analysis for research and applications, Journal of Climate, 24, 3624-3648, 2011.

Robinson, A., Donahue, N., Shrivastava, M., Weitkamp, E., Sage, A., Grieshop, A., Lane, T., Pierce, J., and Pandis, S.: Rethinking organic aerosols: Semivolatile emissions and photochemical aging, Science, 315, 1259, 2007.

Saleh, R., Robinson, E. S., Tkacik, D. S., Ahern, A. T., Liu, S., Aiken, A. C., Sullivan, R. C., Presto, A. A., Dubey, M. K., and Yokelson, R. J.: Brownness of organics in aerosols from biomass burning linked to their black carbon content, Nature Geoscience, 7, 647-650, 2014.

Schiferl, L. D., Heald, C. L., Nowak, J. B., Holloway, J. S., Neuman, J. A., Bahreini, R., Pollack, I. B., Ryerson, T. B., Wiedinmyer, C., and Murphy, J. G.: An investigation of ammonia and inorganic particulate matter in California during the CalNex campaign, Journal of Geophysical Research: Atmospheres, 119, 1883-1902, 2014.

Schnaiter, M., Gimmler, M., Llamas, I., Linke, C., Jäger, C., and Mutschke, H.: Strong spectral dependence of light absorption by organic carbon particles formed by propane combustion, Atmospheric Chemistry and Physics, 6, 2981-2990, 2006.

Schultz, M., Backman, L., Balkanski, Y., Bjoerndalsaeter, S., Brand, R., Burrows, J., Dalsoeren, S., De Vasconcelos, M., Grodtmann, B., and Hauglustaine, D.: REanalysis of the TROpospheric chemical composition over the past 40 years (RETRO)–A long-term global modeling study of tropospheric chemistry, Final Report, Jülich/Hamburg, Germany, 2007. 2007.

Schulz, M., Textor, C., Kinne, S., Balkanski, Y., Bauer, S., Berntsen, T., Berglen, T., Boucher, O., Dentener, F., and Guibert, S.: Radiative forcing by aerosols as derived from the AeroCom present-day and pre-

industrial simulations, Atmospheric Chemistry and Physics, 6, 5246, 2006.

Seidel, D. J., Ao, C. O., and Li, K.: Estimating climatological planetary boundary layer heights from radiosonde observations: Comparison of methods and uncertainty analysis, Journal of Geophysical Research, 115, 2010.

Shiraiwa, M., Kondo, Y., Moteki, N., Takegawa, N., Sahu, L., Takami, A., Hatakeyama, S., Yonemura, S., and Blake, D.: Radiative impact of mixing state of black carbon aerosol in Asian outflow, Journal of Geophysical Research: Atmospheres (1984–2012), 113, 2008.

Shrivastava, M. K., Lane, T. E., Donahue, N. M., Pandis, S. N., and Robinson, A. L.: Effects of gas particle partitioning and aging of primary emissions on urban and regional organic aerosol concentrations, Journal of Geophysical Research, 113, D18301, 2008.

Simon, H., Reff, A., Wells, B., Xing, J., and Frank, N.: Ozone trends across the United States over a period of decreasing NOx and VOC emissions, Environmental science & technology, 49, 186-195, 2014.

Sinyuk, A., Torres, O., and Dubovik, O.: Combined use of satellite and surface observations to infer the imaginary part of refractive index of Saharan dust, Geophysical Research Letters, 30, 2003.

Snider, G., Weagle, C., Martin, R., Van Donkelaar, A., Conrad, K., Cunningham, D., Gordon, C., Zwicker, M., Akoshile, C., and Artaxo, P.: SPARTAN: a global network to evaluate and enhance satellite-based estimates of ground-level particulate matter for global health applications, Atmospheric Measurement Techniques, 8, 505-521, 2015.

Snider, G., Weagle, C. L., Murdymootoo, K. K., Ring, A., Ritchie, Y., Stone, E., Walsh, A., Akoshile, C., Anh, N. X., and Balasubramanian, R.: Variation in global chemical composition of PM 2.5: emerging results from SPARTAN, Atmospheric Chemistry and Physics, 16, 9629-9653, 2016a.

Snider, G., Weagle, C. L., Murdymootoo, K. K., Ring, A., Ritchie, Y., Walsh, A., Akoshile, C., Anh, N. X., Brook, J., Qonitan, F. D., Dong, J., Griffith, D., He, K., Holben, B. N., Kahn, R., Lagrosas, N., Lestari, P., Ma, Z., Misra, A., Quel, E. J., Salam, A., Schichtel, B., Segev, L., Tripathi, S. N., Wang, C., Yu, C., Zhang, Q., Zhang, Y., Brauer, M., Cohen, A., Gibson, M. D., Liu, Y., Martins, J. V., Rudich, Y., and Martin, R. V.: Variation in Global Chemical Composition of PM2.5: Emerging Results from SPARTAN, Atmos. Chem. Phys. Discuss., 2016, 1-35, 2016b.

Spracklen, D. V., Jimenez, J. L., Carslaw, K. S., Worsnop, D. R., Evans, M. J., Mann, G. W., Zhang, Q., Canagaratna, M. R., Allan, J., Coe, H.,

McFiggans, G., Rap, A., and Forster, P.: Aerosol mass spectrometer constraint on the global secondary organic aerosol budget, Atmospheric Chemistry and Physics., 11, 12109-12136, 2011.

Srinivas, B. and Sarin, M.: Brown carbon in atmospheric outflow from the Indo-Gangetic Plain: Mass absorption efficiency and temporal variability, Atmospheric Environment, 89, 835-843, 2014.

Srivastava, R., Ramachandran, S., Rajesh, T., and Kedia, S.: Aerosol radiative forcing deduced from observations and models over an urban location and sensitivity to single scattering albedo, Atmospheric environment, 45, 6163-6171, 2011.

Stettler, M., Eastham, S., and Barrett, S.: Air quality and public health impacts of UK airports. Part I: Emissions, Atmospheric environment, 45, 5415-5424, 2011.

Stier, P., Seinfeld, J. H., Kinne, S., and Boucher, O.: Aerosol absorption and radiative forcing, Atmospheric Chemistry and Physics, 7, 5237-5261, 2007.

Sullivan, A., Peltier, R., Brock, C., De Gouw, J., Holloway, J., Warneke, C., Wollny, A., and Weber, R.: Airborne measurements of carbonaceous aerosol soluble in water over northeastern United States: Method development and an investigation into water- soluble organic carbon sources, Journal of Geophysical Research, 111, 2006.

Sullivan, A., Weber, R., Clements, A., Turner, J., Bae, M., and Schauer, J.: A method for on-line measurement of water-soluble organic carbon in ambient aerosol particles: Results from an urban site, Geophysical Research Letters, 31, L13105, 2004.

Textor, C., Schulz, M., Guibert, S., Kinne, S., Balkanski, Y., Bauer, S., Berntsen, T., Berglen, T., Boucher, O., and Chin16, M.: Analysis and quantification of the diversities of aerosol life cycles within AeroCom, Atmospheric Chemistry and Physics, 6, 1777-1813, 2006.

Tsigaridis, K., Daskalakis, N., Kanakidou, M., Adams, P., Artaxo, P., Bahadur, R., Balkanski, Y., Bauer, S., Bellouin, N., and Benedetti, A.: The AeroCom evaluation and intercomparison of organic aerosol in global models, Atmospheric Chemistry and Physics, 14, 10845-10895, 2014.

Tsimpidi, A., Karydis, V., Zavala, M., Lei, W., Molina, L., Ulbrich, I., Jimenez, J., and Pandis, S.: Evaluation of the volatility basis-set approach for the simulation of organic aerosol formation in the Mexico City metropolitan area, Atmospheric Chemistry and Physics, 10, 525-546, 2010.

Turpin, B. J. and Lim, H. J.: Species contributions to PM2. 5 mass

concentrations: Revisiting common assumptions for estimating organic mass, Aerosol Science & Technology, 35, 602-610, 2001.

Updyke, K. M., Nguyen, T. B., and Nizkorodov, S. A.: Formation of Brown Carbon via Reactions of Ammonia with Secondary Organic Aerosols from Biogenic and Anthropogenic Precursors, Atmospheric Environment, 63, 22-31, 2012.

van der Werf, G., Randerson, J., Giglio, L., Collatz, G., Mu, M., Kasibhatla, P., Morton, D., DeFries, R., Jin, Y., and van Leeuwen, T.: Global fire emissions and the contribution of deforestation, savanna, forest, agricultural, and peat fires (1997-2009), Atmospheric Chemistry and Physics, 10, 11707-11735, 2010.

van Donkelaar, A., Martin, R. V., Brauer, M., and Boys, B. L.: Use of satellite observations for long-term exposure assessment of global concentrations of fine particulate matter, Environmental health perspectives, 123, 135, 2015.

Volkamer, R., Jimenez, J. L., San Martini, F., Dzepina, K., Zhang, Q., Salcedo, D., Molina, L. T., Worsnop, D. R., and Molina, M. J.: Secondary organic aerosol formation from anthropogenic air pollution: Rapid and higher than expected, Geophysical Research Letters, 33, 17, 2006.

Volkamer, R., San Martini, F., Molina, L. T., Salcedo, D., Jimenez, J. L., and Molina, M. J.: A missing sink for gas□phase glyoxal in Mexico City: Formation of secondary organic aerosol, Geophysical Research Letters, 34, 2007.

Wang, J. X.: Mapping the Global Dust Storm Records: Review of Dust Data Sources in Supporting Modeling/Climate Study, Current Pollution Reports, 1, 82-94, 2015.

Wang, X., Heald, C., Ridley, D., Schwarz, J., Spackman, J., Perring, A., Coe, H., Liu, D., and Clarke, A.: Exploiting simultaneous observational constraints on mass and absorption to estimate the global direct radiative forcing of black carbon and brown carbon, Atmospheric Chemistry and Physics, 14, 10989-11010, 2014.

Wang, Y., Jacob, D. J., and Logan, J. A.: Global simulation of tropospheric O3-NO x-hydrocarbon chemistry 1. Model formulation, Journal of Geophysical Research, 103, 10713-10710,10725, 1998.

Wang, Y., Zhang, Q., He, K., Zhang, Q., and Chai, L.: Sulfate-nitrate-ammonium aerosols over China: response to 2000–2015 emission changes of sulfur dioxide, nitrogen oxides, and ammonia, Atmospheric Chemistry and Physics, 13, 2635-2652, 2013.

Ward, D., Susott, R., Kauffman, J., Babbitt, R., Cummings, D., Dias, B.,

Holben, B., Kaufman, Y., Rasmussen, R., and Setzer, A.: Smoke and Fire Characteristics for Cerrado and Deforestation Burns in Brazil: BASE-B Experiment, Journal of Geophysical Research, 97, 14601-14619, 1992.

Ward, D. E. and Hao, W.: Projections of emissions from burning of biomass foruse in studies of global climate and atmospheric chemistry, Air and Waste Management Association, 1991. 1991.

Washenfelder, R., Young, C., Brown, S., Angevine, W., Atlas, E., Blake, D., Bon, D., Cubison, M., De Gouw, J., and Dusanter, S.: The glyoxal budget and its contribution to organic aerosol for Los Angeles, California, during CalNex 2010, Journal of Geophysical Research, 116, 2011.

Weber, R. J., Sullivan, A. P., Peltier, R. E., Russell, A., Yan, B., Zheng, M., de Gouw, J., Warneke, C., Brock, C., and Holloway, J. S.: A study of secondary organic aerosol formation in the anthropogenic-influenced southeastern United States, Journal of Geophysical Research, 112, D13302, 2007.

Wells, K. C., Witek, M., Flatau, P., Kreidenweis, S. M., and Westphal, D. L.: An analysis of seasonal surface dust aerosol concentrations in the western US (2001–2004): Observations and model predictions, Atmospheric Environment, 41, 6585-6597, 2007.

Wiedinmyer, C., Akagi, S., Yokelson, R., Emmons, L., Al-Saadi, J., Orlando, J., and Soja, A.: The Fire INventory from NCAR (FINN): a high resolution global model to estimate the emissions from open burning, Geoscientific Model Development, 4, 625-641, 2011.

Wiscombe, W. J.: Improved Mie scattering algorithms, Applied optics, 19, 1505-1509, 1980.

Yang, M., Howell, S., Zhuang, J., and Huebert, B.: Attribution of aerosol light absorption to black carbon, brown carbon, and dust in China–interpretations of atmospheric measurements during EAST-AIRE, Atmospheric Chemistry and Physics, 9, 2035-2050, 2009.

Yttri, K., Aas, W., Bjerke, A., Ceburnis, D., Dye, C., Emblico, L., Facchini, M., Forster, C., Hanssen, J., and Hansson, H.: Elemental and organic carbon in PM10: a one year measurement campaign within the European Monitoring and Evaluation Programme EMEP, Atmospheric Chemistry and Physics Discussions, 7, 3859-3899, 2007.

Yu, F.: A secondary organic aerosol formation model considering successive oxidation aging and kinetic condensation of organic compounds: global scale implications, Atmospheric Chemistry and Physics, 11, 1083-1099, 2011.

Yu, L., Smith, J., Laskin, A., Anastasio, C., Laskin, J., and Zhang, Q.: Chemical characterization of SOA formed from aqueous-phase reactions of phenols with the triplet excited state of carbonyl and hydroxyl radical, Atmospheric Chemistry and Physics, 14, 13801-13816, 2014.

Zender, C. S., Bian, H., and Newman, D.: Mineral Dust Entrainment and Deposition (DEAD) model: Description and 1990s dust climatology, Journal of Geophysical Research: Atmospheres (1984–2012), 108, 2003.

Zhang, F., Xu, L., Chen, J., Yu, Y., Niu, Z., and Yin, L.: Chemical compositions and extinction coefficients of PM< sub> 2.5</sub> in peri-urban of Xiamen, China, during June 2009–May 2010, Atmospheric Research, 106, 150-158, 2012a.

Zhang, H., Worton, D. R., Lewandowski, M., Ortega, J., Rubitschun, C. L., Park, J.-H., Kristensen, K., Campuzano-Jost, P., Day, D. A., and Jimenez, J. L.: Organosulfates as tracers for secondary organic aerosol (SOA) formation from 2-methyl-3-buten-2-ol (MBO) in the atmosphere, Environmental science & technology, 46, 9437-9446, 2012b.

Zhang, L., Jacob, D., Knipping, E., Kumar, N., Munger, J., Carouge, C., Donkelaar, A. v., Wang, Y., and Chen, D.: Nitrogen deposition to the United States: distribution, sources, and processes, Atmospheric Chemistry and Physics, 12, 4539-4554, 2012c.

Zhang, L., Kok, J. F., Henze, D. K., Li, Q., and Zhao, C.: Improving simulations of fine dust surface concentrations over the western United States by optimizing the particle size distribution, Geophysical Research Letters, 40, 3270-3275, 2013a.

Zhang, Q., Jimenez, J., Canagaratna, M., Allan, J., Coe, H., Ulbrich, I., Alfarra, M., Takami, A., Middlebrook, A., and Sun, Y.: Ubiquity and dominance of oxygenated species in organic aerosols in anthropogenically-influenced Northern Hemisphere midlatitudes, Geophysical Research Letters, 34, L13801, 2007.

Zhang, Q., Worsnop, D., Canagaratna, M., and Jimenez, J. L.: Hydrocarbon-like and oxygenated organic aerosols in Pittsburgh: insights into sources and processes of organic aerosols, Atmospheric Chemistry and Physics Discussions, 5, 8421-8471, 2005.

Zhang, X., Lin, Y.-H., Surratt, J. D., and Weber, R. J.: Sources, Composition and Absorption Ångström Exponent of Light-absorbing Organic Components in Aerosol Extracts from the Los Angeles Basin, Environmental Science & Technology, doi: 10.1021/es305047b, 2013b. 2013b.

Zhang, X., Lin, Y. H., Surratt, J. D., Zotter, P., Prévôt, A. S. H., and Weber, R. J.: Light-absorbing soluble organic aerosol in Los Angeles and Atlanta: A contrast in secondary organic aerosol, Geophysical Research Letters, 38, 21810, 2011.

Zhao, P., Dong, F., He, D., Zhao, X., Zhang, X., Zhang, W., Yao, Q., and Liu, H.: Characteristics of concentrations and chemical compositions for PM 2.5 in the region of Beijing, Tianjin, and Hebei, China, Atmospheric Chemistry and Physics, 13, 4631-4644, 2013.

Zhong, M. and Jang, M.: Light absorption coefficient measurement of SOA using a UV-Visible spectrometer connected with an integrating sphere, Atmospheric Environment, 45, 4263-4271, 2011.

Zhong, M., Jang, M., Oliferenko, A., Pillai, G. G., and Katritzky, A. R.: The SOA Formation Model Combined with Semiempirical Quantum Chemistry to Predict UV-Vis Absorption of Secondary Organic Aerosols, Physial Chemistry Chemical Physics, 14, 9058-9066, 2012.

Zhu, L., Henze, D., Bash, J., Jeong, G.-R., Cady-Pereira, K., Shephard, M., Luo, M., Paulot, F., and Capps, S.: Global evaluation of ammonia bidirectional exchange and livestock diurnal variation schemes, Atmospheric Chemistry and Physics, 15, 12823-12843, 2015.

Zhu, L., Henze, D., Cady□Pereira, K., Shephard, M., Luo, M., Pinder, R., Bash, J., and Jeong, G. R.: Constraining US ammonia emissions using TES remote sensing observations and the GEOS□Chem adjoint model, Journal of Geophysical Research: Atmospheres, 118, 3355-3368, 2013.

# 국문 초록

에어로졸은 온실 기체에 의한 양의 복사 효과를 상쇄할 수 있으나, 에어로졸에 의한 복사 효과 산정에는 큰 불확실성이 존재한다. 이러한 큰 불확실성은 현재 대기 중 에어로졸을 모의하는 모델의 한계에서 기인한다. 본 학위 논문은 모델의 에어로졸 모의 성능 향상을 위하여 크게 세 가지의 현안 (1. 에어로졸의 질량 농도 모의, 2. 모델 내 에어로졸 종 분류, 3. 에어로졸의 물리적/광학적 특성) 에 대하여 연구를 수행하였다. 연구에 사용한 모델은 전 지구 화학 수송 모형인 GEOS-Chem 모델이며, 최신의 연구 결과들을 모델에 적용 시켜 모의 성능을

향상시키고자 하였다. 또한 개선된 모델을 한반도에서 수행된 KORUS-AQ 캠페인에 적용하여 오염이 심한 지역에서의 모델의 모의 성능을 검증하였다. 첫번째 현안으로, 유기 에어로졸이 전체 미세 에어로졸 중 매우 큰 비중을 차지하나 (20-90%) 현재 대부분의 모델들이 이러한 유기 에어로졸을 크게 과소 모의 하고 있다. 본 연구에서는 GEOS-Chem 모델에 volatility basis set (VBS) 방법을 적용하여 유기 에어로졸 모의 성능을 개선하였다. VBS 방법을 통해 이차 유기 에어로졸의 대기 중 화학적 노화 과정을 모의할 수 있었으며, 이를 통해 이차 유기 에어로졸의 휘발성 감소와 이에 의한 질량 농도 증가를 모의하였다. 이러한 화학적 노화 과정을 고려 후, 특히 시골 지역에서 모델의 모의 성능 향상을 발견할 수 있었다. 두번째 현안으로, 현재의 모델들은 유기 에어로졸 전체를 빛을 산란하는 에어로졸로 다루고 있으나, 최근의 관측 결과들에서 일부 유기 에어로졸은 빛을 흡수할 수 있다는 사실이 발견되었다. 이러한 유기 에어로졸은 브라운 카본이라고 불리며, 브라운 카본은 대부분의 모델에서 고려하지 않고 있다. 브라운 카본을 모델에서 모의 하기 위해 새로운 방법을 개발하여 산불이나 가정의 나무 연료에서 발생하는 브라운 카본의 배출량을 추정하였다. 브라운 카본의 대기 중 양을 계산하였을 때 전체 유기 에어로졸의 대기 중 양의 21% 정도를 차지하였다. 브라운 카본을 고려하였을 때, 유기 에어로졸에 의한 복사 냉각 효과를 16% 상쇄하였으며, 이는 또한 이산화질소의 광분해 비율을 감소시켜 오존 농도의 감소 (봄철 아시아에서 최대 -13%) 를 야기하는 결과를 얻었다. 세번째 현안으로, 상당수의 전 지구 모델들이 에어로졸에

의한 단산란알베도를 과대 모의하고 있었으며, 이는 에어로졸에 의한 복사 강제력 산정에 있어 큰 오차를 야기할 수 있다. 그러나 에어로졸의 다양한 물리적/광학적 특성을 모델에서 모두 고려하기는 어려우며, 따라서 본 연구에서는 모델 민감도 분석을 통해 단산란알베도에 영향을 미치는 요소들을 분류하고, 그 효과를 알아보았다. 블랙 카본의 질량 농도가 같더라도 입자 크기 분포나 굴절률, 밀도 등이 큰 영향을 미치는 것을 확인하였다. 또한 브라운 카본의 추가 고려, 관측에 기반한 황사 에어로졸의 크기 분포 적용을 하였을 때도 단산란알베도 값에 큰 영향을 미쳐 결과적으로 모델의 값이 AERONET에 의하여 관측된 값과 비슷해지는 결과를 얻을 수 있었다. 마지막으로, 위에서 개발된 모델을 한반도에서 수행된 KORUS-AQ 캠페인에 적용하여 모의 능력을 검증하였다. 모델은 관측된 유기 에어로졸의 평균 농도를 5%의 편차로 비교적 잘 모의하였고, 고도별 평균 분포 비교에서도 관측과 비슷한 농도를 보였다. 그러나, 개개의 관측 평균값과의 비교에서는 모델이 관측을 2배 이상 과대 모의 또는 과소 모의를 하는 것을 발견할 수 있었다. 모델이 과소 모의를 할 때에는 주로 관측된 유기 에어로졸이 산불의 영향 하에 놓여있을 때였으며, 이는 주로 모델의 산불 배출량 자료의 과소모의에서 기인한 것으로 분석되었다. 모델이 과대 모의를 하는 이유는 주로 모델에서 광화학 반응에 의한 유기 에어로졸 농도 감소를 고려하지 않는 것에서 찾을 수 있었으며, 앞으로의 모델에서는 이러한 광화학 반응이 고려되어야 한다는 점을 보였다.

주요어 : 유기 에어로졸, 화학적 노화, 브라운 카본, 에어로졸 복사 효과, 단산란알베도

학번 : 2010-20353